LIGHT SCATTERING STUDIES OF IRREGULARLY SHAPED PARTICLES

by

YULI WANG HEINSON

B.S., Harbin Normal University, 2010
M.S., Creighton University, 2012

A DISSERTATION

submitted in partial fulfillment of the requirements for the degree

DOCTOR OF PHILOSOPHY

Department of Physics
College of Arts and Sciences

KANSAS STATE UNIVERSITY
Manhattan, Kansas

2016

Abstract

We present light scattering studies of irregularly shaped particles which significantly affect the climate. We built and calibrated our apparatus which was able to measure all six independent scattering matrix elements. Our apparatus detects light from 0.32° to 157° simultaneously. We studied all six scattering matrix elements of irregularly shaped Arizona Road Dust which behave differently than those of spheres. We strongly focused on the most important scattering matrix element – the phase function, scattered intensity vs. the scattering angle, which we applied Q-space analysis to. Q-space analysis involves plotting the scattering intensity vs. the magnitude of the scattering wave vector q or qR with R the radius of a particle, on a double logarithmic scale. We measured and studied the phase functions of Al_2O_3 abrasives; compared the scattering from the abrasives with the scattering of spheres.

To generalize the study, we collected a large amount of experimental and theoretical data from our group and others and applied Q-space analysis. They all displayed a common scattering pattern. The power law exponents showed a quasi-universal functionality with the internal coupling parameter ρ'. *In situ* studies of the soot fractal aggregates produced from a burner were also conducted. A power law exponent -1.85 is seen to imply the aggregates have fractal dimension of $D_f = 1.85$.

The overall work presented shows Q-space analysis uncovers patterns common to *all* particles: a q-independent forward scattering regime is followed by a Guinier regime, a power law regime, and sometimes an enhanced back scattering regime. The description of the patterns applies to spheres as well, except the power law regime has more than a single power law. These simple patterns give a unified description for all particle shapes. Moreover, the power law exponents have a quasi-universal functionality with ρ' for non-fractal aggregates. The absolute

value of the exponents start from 4 when ρ' is small. As ρ' increases, the exponents decrease until the trend levels off at $\rho' \gtrsim 10$ where the exponents reach a constant 1.75 ± 0.25. All the non-fractal particles fall on the same trend regardless of the detail of their structure.

LIGHT SCATTERING STUDIES OF IRREGULARLY SHAPED PARTICLES

by

YULI WANG HEINSON

B.S., Harbin Normal University, 2010
M.S., Creighton University, 2012

A DISSERTATION

submitted in partial fulfillment of the requirements for the degree

DOCTOR OF PHILOSOPHY

Department of Physics
College of Arts and Sciences

KANSAS STATE UNIVERSITY
Manhattan, Kansas

2016

Approved by:

Major Professor
Christopher M. Sorensen

Copyright

Abstract

We present light scattering studies of irregularly shaped particles which significantly affect the climate. We built and calibrated our apparatus which was able to measure all six independent scattering matrix elements. Our apparatus detects light from 0.32° to 157° simultaneously. We studied all six scattering matrix elements of irregularly shaped Arizona Road Dust which behave differently than those of spheres. We strongly focused on the most important scattering matrix element – the phase function, scattered intensity vs. the scattering angle, which we applied Q-space analysis to. Q-space analysis involves plotting the scattering intensity vs. the magnitude of the scattering wave vector q or qR with R the radius of a particle, on a double logarithmic scale. We measured and studied the phase functions of Al_2O_3 abrasives; compared the scattering from the abrasives with the scattering of spheres.

To generalize the study, we collected a large amount of experimental and theoretical data from our group and others and applied Q-space analysis. They all displayed a common scattering pattern. The power law exponents showed a quasi-universal functionality with the internal coupling parameter ρ'. *In situ* studies of the soot fractal aggregates produced from a burner were also conducted. A power law exponent -1.85 is seen to imply the aggregates have fractal dimension of $D_f = 1.85$.

The overall work presented shows Q-space analysis uncovers patterns common to *all* particles: a q-independent forward scattering regime is followed by a Guinier regime, a power law regime, and sometimes an enhanced back scattering regime. The description of the patterns applies to spheres as well, except the power law regime has more than a single power law. These simple patterns give a unified description for all particle shapes. Moreover, the power law exponents have a quasi-universal functionality with ρ' for non-fractal aggregates. The absolute

value of the exponents start from 4 when ρ' is small. As ρ' increases, the exponents decrease until the trend levels off at $\rho' \gtrsim 10$ where the exponents reach a constant 1.75 ± 0.25. All the non-fractal particles fall on the same trend regardless of the detail of their structure.

Table of Contents

List of Figures x
List of Tables xv
Acknowledgements xvi
Chapter 1 - Introduction 1
1.1 Q-Space Analysis 2
1.2 The Scattering Matrix 4
1.3 The internal coupling parameter ρ' 6
Chapter 2 - Experiment 9
2.1. Experimental Apparatus 9
2.2. Calibrations 16
2.2.1 Forward scattering 16
2.2.2 Side scattering 18
2.2.3 Connecting forward and side scattering 30
2.2.4 Water droplets 31
2.3 Dust Aerosol Generation 38
Chapter 3 - Arizona Road Dust 40
3.1 Results 41
3.2 Discussion 42
3.3 Summary 46
Chapter 4 - Al_2O_3 Abrasives 48
4.1 Results 48
4.2 Discussion 53
4.2.1 Sizes 53
4.2.2 Comparison between spheres and Al_2O_3 abrasives 55
4.3 Summary 58
Chapter 5 - The Exponent of Q-Space Analysis as a Function of ρ' 59
5.1 Q-Space analysis of a collection of irregularly shaped particles 59
5.1.1 Analysis of prior published data sets 59

5.1.2 Arizona Road Dust (AZRD) 63
5.1.3 Al_2O_3 Abrasives 64
5.1.4 Gaussian Random Spheres (GRSs) 65
5.1.5 Thickened Percolation Clusters 67
5.1.6 Irregular spheres 69
5.2 The exponent of Q-space analysis as a function of ρ' 69
5.3 Summary 72
Chapter 6 - Soot Fractal Aggregates 75
6.1 Premixed Burner 78
6.2 Results 80
6.3 Discussion 82
6.4 Summary 84
Chapter 7 - Conclusion and Future Work 86
References 89
Appendix A - Internal coupling parameter and corresponding Q-space exponent 98

List of Figures

Figure 1.1 Comparison between (a) conventional analysis and (b) Q-Space analysis of a sphere with refractive index m=1.5 and various size parameters kR [*Sorensen and Fischbach*, 2000]. Unlike the conventional analysis yields no definable pattern, Q-space analysis shows forward scattering regime followed by a Guinier regime and a power law regime with quantifiable exponents. 3

Figure 2.1 Picture of our experimental apparatus with major optical elements labeled. 11

Figure 2.2 A schematic diagram of the experimental apparatus. The angle at the center of each channel on the detectors was labeled. 11

Figure 2.3 Single slit diffraction experimental and theoretical patterns for the forward direction. Intensity (arbitrary units) was plotted vs. q (cm^{-1}). The -2 slope line indicated the power law envelope of the theoretical curve. 18

Figure 2.4 (a) Geometry of the ellipse that the elliptical mirror was part of it; (b) the mechanical drawing of the elliptical mirror. 19

Figure 2.5 (a) A top view of the calibration method where the grass dropper was filled with glowing agent; (b) angle independent intensities of the glass dropper. 21

Figure 2.6 (a) A top view of our real scattering situation. Using capillary filled with glowing agent to simulate our actual scattering shape, we combined (b) and (c) to get the calibration done. 22

Figure 2.7 Uniform intensities along the angles for the capillary calibration method. 22

Figure 2.8 The 1mm iris determined the subtended amount of the scattering volume by connecting the edges of the iris to a picked up point of the mirror and their reflected rays. 23

Figure 2.9 Glowing glass dropper placed vertically. The subtended areas in red (a) and blue (b), formed by the reflected rays and glass dropper, correspond to different scattering angles. The black bars in (a) and (b) are crossing the center of the glass dropper overlapped the near focal point of the mirror. Each black bar was perpendicular to the line that connected the focal point and ray-tracing back point on the mirror. 24

Figure 2.10 Glowing capillary placed horizontally. The subtended areas in red (a) and blue (b), formed by the reflected rays and the capillary, correspond to different scattering angles. The

black bars in (a) and (b) were crossing the near focal point perpendicular to the axis of the revolution of the mirror. 27
Figure 2.11 Lambert's Cosine Law for glowing capillary placed horizontally. A was a normal observer; B was off-normal observer, which is our case. At an arbitrary angle, I, α_0, α, and d_0 were constants; thus the observed intensity I_0 only depended upon $d\cos(90-\theta)$..... 28
Figure 2.12 A calibration of the whole system by measuring S_{11} of water droplets using setup shown in Fig. 2.2 and Fig. 2.13. The S_{11} (arbitrary units) was plotted vs. the scattering angle. (a) Scattering data from the two setup. (b) Side scattering was calibrated be comparing the data from the two setups. (c) Forward and side scattering were connected.. 31
Figure 2.13 A schematic of the calibration to connect forward scattering and side scattering. ... 31
Figure 2.14 Experimental water droplet S_{11} data compared to Mie theory for perfect, polydisperse spheres with weighted mean radius of 1.1μm and a geometric width of 1.5 for a log-normal distribution. S_{11} was normalized at the smallest q. 33
Figure 2.15 The scattering matrix elements vs. the scattering angle θ for water droplets produced from an atomizer compared to Mie theory. S_{11} is normalized at the smallest angle. 34
Figure 2.16 The scattering matrix elements vs. the scattering angle θ for water droplets from our group at $\lambda = 532nm$ and the Amsterdam-Granada group at $\lambda = 441.6nm$ and $632.8nm$. S_{11} is normalized at 30° 35
Figure 2.17 Guinier analysis of water droplet. 37
Figure 2.18 Monodisperse water droplet $R_{g,G}/R_g vs.\, \rho$ [*Sorensen and Shi*, 2000]..... 37
Figure 2.19 Dust aerosol generator (a) picture and (b) schematic drawing with major parts labeled. 39
Figure 3.1 The Q-space analysis on the Ultrafine, Fine and Medium AZRD samples. S_{11} of three ARZD samples are normalized to 1 at the smallest q. 41
Figure 3.2 The scattering matrix elements vs. θ for three sizes of AZRD. S_{11} of three ARZD samples are normalized at the smallest angle. 42
Figure 3.3 The summary of the work done by the Amsterdam group on many different types of irregular shaped particles [*Volten et al.*, 2001]. Our AZRD data would fall right on top of this figure. 43
Figure 3.4 Guinier analysis of AZRD, Ultrafine, Fine and Medium. 44

Figure 3.5 The images for three AZRD samples under an optical compound microscope. Each figure has a 10 micron scale bar in the lower left and a scale bar equal to the light scattering determined $2R_g$ in the upper right for comparison to the images. Note that light scattering is strongly affected by the largest particles in an ensemble..... 45
Figure 3.6 The comparison of the Q-space analysis between (a) water droplets and (b) AZRD. Unlike scattering from our "quasi-spherical" water droplets shows the power law regime with exponents of -2 and -4. Scattering from three AZRD samples all show single power laws with exponents other than -4. 46
Figure 4.1 Q-space analysis of scattering by 1200 grit Al_2O_3 abrasives and the corresponding image under an optical compound microscope..... 50
Figure 4.2 Q-space analysis of scattering by 1000 grit Al_2O_3 abrasives and the corresponding image under an optical compound microscope..... 50
Figure 4.3 Q-space analysis of scattering by 800 grit Al_2O_3 abrasives and the corresponding image under an optical compound microscope..... 51
Figure 4.4 Q-space analysis of scattering by 600 grit Al_2O_3 abrasives and the corresponding image under an optical compound microscope..... 51
Figure 4.5 Q-space analysis of scattering by 400 grit Al_2O_3 abrasives and the corresponding image under an optical compound microscope..... 52
Figure 4.6 Q-space analysis of scattering by 320 grit Al_2O_3 abrasives and the corresponding image under an optical compound microscope..... 52
Figure 4.7 Guinier analysis on Al_2O_3 abrasives of 1200, 1000, and 800 grit. The slopes indicated the measured radii of gyration of 2.4μm, 3.7μm, and 6.4μm, respectively..... 54
Figure 4.8 Comparisons between scattering by spheres and the 1200, 1000, and 800 grit abrasives. The scattered intensity (normalized at $qR \ll 1$) is plotted vs. qR for each grit. Spheres and abrasives were forced to fit in the Guinier, $qR \ll 1$, range. Also indicated are the $qR \simeq \rho'$ crossover points for the sphere scattering..... 56
Figure 5.1 Scattered intensities (a.u.) (intensities have been scaled for clarity) expressed as functions of the parameter q (cm^{-1}), for studies of the indicated particle types, as reported by the Amsterdam-Granada group (Munoz et al. 2000; Munoz et al. 2001; Munoz et al. 2002; Munoz et al. 2004; Munoz et al. 2006; Munoz et al. 2007; Munoz et al. 2012; Volten et al. 2001; Volten et al. 2006; Laan et al. 2009). Lines are the power law fits proposed in this

work, and the numbers to the right of the plots are the exponents of the power law. (a) Volcanic ash (Pinatubo, Lokon) measured at $\lambda = 441.6nm$. (b) Volcanic ash (Pinatubo, Lokon, El Chichol, Mnt St. Helens) measured at $\lambda = 632.8nm$. (c) Olivine S, Olivine M, Olivine L, Olivine XL measured at $\lambda = 441.6nm$. (d) Olivine S, Olivine M, Olivine L, Olivine XL measured at $\lambda = 632.8nm$. (e) Feldspar, Red clay, Quartz, Loess, Sahara, Allende, Green clay, Fly ash measured at $\lambda = 441.6nm$. (f) Feldspar, Redy clay, Quartz, Loess, Sahara, Allende, Green clay, Fly ash measure at $\lambda = 632.8nm$. (g) Volcanic ash (Redoubt A, Redoubt B, Spurr Ashton, Spurr Anchorage, Spurr Gunsight, Spurr Stop 33) measured at $\lambda = 632.8nm$. (h) Hematite, Rutile, Martian analog (palagonite), Sahara sand (Libya) measured at $\lambda = 632.8nm$. (i) Forsterie initial, Forsterie small, Forsterie washed measured at $\lambda = 632.8nm$..... 61

Figure 5.2 Comparison between conventional analysis and Q-space analysis on desert dust [*Sorensen*, 2013a]. The same data are plotted on each side of the figure. Plotting the data vs. linear θ (left) yields a non-descript curve; plotting vs. logarithmic q (right) yields an obvious straight line regime indicating a power law. 62

Figure 5.3 Q-space analysis on extrapolated AZRD data from Curtis et al. [*Curtis et al.*, 2008].64

Figure 5.4 GRS model compared to Saharan dust particles from [*Munoz et al.*, 2007]. 65

Figure 5.5 GRS described by three parameters [*Maughan et al.*, 2016]. The parameter a is the mean radius. The parameter σ is the relative standard deviation in the radial direction. The parameter ν is the power law exponent controlling the angular range of fluctuations in a tangential direction..... 66

Figure 5.6 Q-space analysis on GRSs with ka=30, $\sigma = 0.2$, and $\nu = 0.3$. Lines are the power law fits and the numbers to the right of the plots are the exponents of the power law. A different multiplication factor is applied to the intensity for each plot to separate one from another. 67

Figure 5.7 Thickened percolation cluster (a) side view, (b) three quarters view, and (c) top view. 68

Figure 5.8 Q-space analysis on thickened percolation clusters. Lines are the power law fits and the numbers to the right of the plots are the exponents of the power law. A different multiplication factor is applied to the intensity for each plot for clarity..... 68

Figure 5.9 Strongly damaged spheres from [*Zubko et al.*, 2006]. 69

Figure 5.10 The exponents of the power laws vs. the internal coupling parameter ρ'. 70

Figure 5.11 A generalized schematic of Q-space analysis for non-spherical particles. Scattered intensity *I* (a.u.) is plotted vs. *q* (cm^{-1}) on a log-log scale. 73
Figure 6.1 Simulated soot aggregate [*Heinson*, 2015] made using DLCA algorithm [*Sorensen*, 2001]. 76
Figure 6.2 (a) A picture of the premixed burner we designed and built with a suction nozzle connected to a vacuum cleaner; (b) schematic drawing of the burner main body and (c) two disassembled burner parts with major elements labeled. 79
Figure 6.3 Preliminary data of soot produced from our premixed burner. 81
Figure 6.4 TEM image of the soot freshly produced from the premixed burner. A scale bar of $0.699\mu m$ across one soot fractal aggregate indicated its approximate visible optical size. . 82
Figure 6.5 Examples of anti-correlation; (a) shows strong decreasing trend as q got smaller for small q regime; when we decreased the C_2H_4 to C_3H_8 ratio, as shown in (b), the anti-correlation was smaller. 83

List of Tables

Table 2.1 Center angles and their angle spreads for the 16 channel forward scattering detector. 17

Table 2.2 The angles at the centers of the 15 channels and the corresponding angle spreads. 20

Table 2.3 Scattering angles θ and their corresponding subtended d for the case where a glowing glass dropper was placed vertically. We also included $\Delta\theta$ from Table 2.2 and calculated $d \times \Delta\theta$ which was nearly constant. 26

Table 2.4 Scattering angles θ and their corresponding subtended d and $d\cos(90 - \theta)$ and for the case where a glowing capillary placed vertically..... 29

Acknowledgements

First, I would like to express my sincere gratitude to my advisor, Dr. Chris Sorensen, who has been constantly and patiently encouraging and guiding me since I came to K-State. Without him I could not accomplish my goals.

I also would like to thank Dr. Amit Chakrabarti for all his help and suggestions. With his theoretical insights we could better understand our work.

I would like to thank Dr. Kristan Corwin, Dr. Charles Rice, for being my committee members, and Dr. William Kuhn for being the chairperson of my examination committee.

I would like to thank Tim Sobering, Russell Taylor, and David Huddleston for the detectors electronic design. I am grateful to Russ Reynolds for his help on building and modifying our research instrumentation.

We are grateful that the Amsterdam-Granada group provided various kinds of aerosol particle data on their website and allowed us to use them, and the Iowa group [*Curtis et al.*, 2008] allowed us to extrapolate their data on Arizona Road Dust.

Special thanks are given to Justin Maughan and William Heinson for their theoretical support on this work.

Last but not least, I will like to thank my friends and family, especially my husband, for their support.

This work was supported by National Science Foundation under grant no. AGM 1261651 and Army Research Laboratory under grant no. W911NF-14-1-0352.

Chapter 1 - Introduction

Light scattering by particles has been a subject of enduring scientific interest [*Mishchenko*, n.d.; *Kerker*, 1969; *Hulst*, 1981; *Bohren and Huffman*, 1998; *Mishchenko et al.*, 1999]. Not only does scattering from irregularly shaped particles hold inherent intellectual interest, but such scattering plays a significant role in affecting the global radiation budget. Scattered light from spherical particles has been studied for more than 100 years and is well understood [*Mie*, 1908; *Hulst*, 1981; *Bohren and Huffman*, 1998]. Much work, both experiment and theory, is still being conducted to study irregularly shaped particles [*Muinonen*, 1998; *Muinonen and Lagerros*, 1998; *Munoz et al.*, 2000, 2001, 2002, 2004, 2006, 2007, 2012; *Volten et al.*, 2001, 2006; *Kalashnikova and Sokolik*, 2004; *Dubovik et al.*, 2006; *Muñoz et al.*, 2010; *Nousiainen et al.*, 2011a, 2011b]. However, a coherent description and understanding of light scattering by irregularly shaped particles has not been achieved. This dissertation is directed at that challenge.

Most aerosol mass in the atmosphere, including that of entrained mineral dust, volcanic ash, and soot produced from combustion systems and forest fire, consists of particles with irregular shapes. The manner in which the irregularly shaped particles scatter and absorb light has implications for the radiative forcing component of climate models [*Ghan and Schwartz*, 2007] and for aerosol optical remote sensing, especially satellite remote sensing [*Hoff and Christopher*, 2009]. For example, satellite aerosol observations use a specific angular geometry between incident solar radiation and sensor field of view, therefore the aerosol phase function, scattered intensity as a function of scattering angle, is needed to determine scattering into other directions. Similarly, calculations of aerosol radiative forcing rely upon the phase function to represent the energy that is scattered toward and away from the earth's surface. Current

assumptions for aerosol phase function range from the single-parameter Henyey-Greenstein equation [*Henyey and Greenstein,* 1941] and calculations for spherical [*Mie*, 1908] or spheroidal [*Dubovik et al.,* 2006] particles to approximations for irregularly shaped particles using composition-size-shape distributions [*Kalashnikova and Sokolik*, 2004]. Multiangle Imaging Spectroradiometer (MISR) which provides independent constraints on aerosol properties has been used to study aerosols [*Kalashnikova et al.*, 2004; *Kahn and Gaitley*, 2015].

Due to its significant impacts, the phase function is the major element we will focus on in this dissertation. Unlike others studying the phase function by graphing the scattered intensity as a function of the scattering angle, we apply the unique Q-space analysis to phase function, and thereby uncover common patterns common to *all* shapes.

1.1 Q-Space Analysis

Q-space analysis was originally used in X-ray scattering and neutron scattering [*Guinier et al.*, 1955; *Glatter and Kratky*, 1982; *Lovesey*, 1986]; however it was Sorensen and co-workers who first applied it to light scattering [*Sorensen and Fischbach*, 2000; *Berg et al.*, 2005; *Sorensen*, 2013b]. Q-space analysis refers to the use of q, representing the magnitude of the scattering wave vector:

$$q = 2k\sin(\theta/2) \tag{1.1}$$

where $k = 2\pi/\lambda$ with λ the wavelength, and θ is the scattering angle. Instead of plotting the scattered intensity vs. the scattering angle θ on a log-linear scale, Q-space analysis graphs scattered intensity vs. the magnitude of the scattering wave vector q (unit of inverse length) or the dimensionless qR (R is the effective radius, e.g. volume equivalent radius of the particle) on

a log-log scale (equivalent results, however the latter variable eliminates the particle size dependence).

Unlike the conventional analysis plotting vs. linear θ which yields no definable pattern, Q-space analysis reveals a series of regimes as a function of q common to *all* particle shapes. In particular, power law functionalities of the scattered intensity versus q with quantifiable exponents are uncovered. Figure 1.1 shows an example from previous work [*Sorensen and Fischbach*, 2000] of Mie scattering (scattering from spherical particles) for a sphere with refractive index m=1.5 and various size parameters kR, where the intensity is normalized to 1 at 0°, comparing (a) conventional analysis and (b) Q-space analysis. In Fig. 1.1a, series incoherent curves are seen without descriptive patterns. In contrast, in Fig. 1.1b, the same data is presented under Q-space analysis; clearly, a common forward scattering lobe is followed by a Guinier regime at $qR \approx 1$, an envelope with slope of -2 crossing over to an envelope with slope of -4.

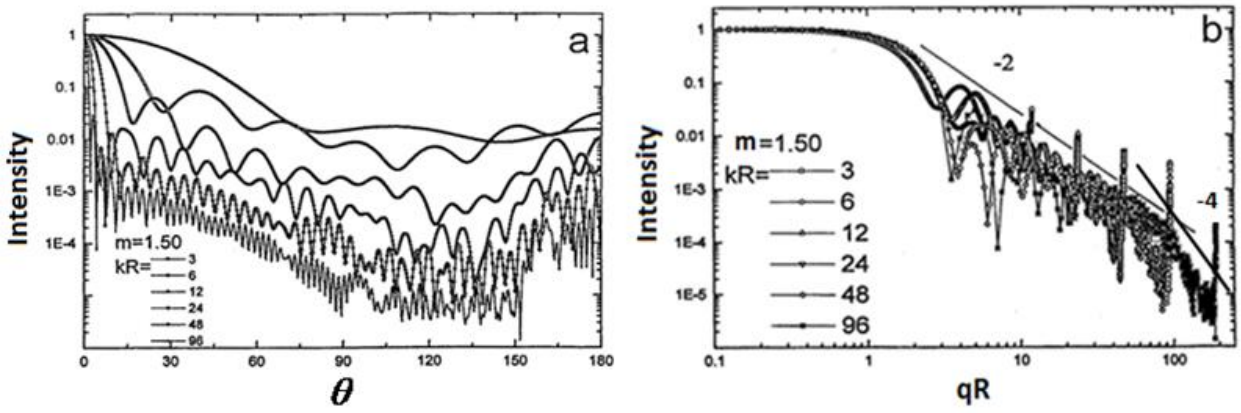

Figure 1.1 Comparison between (a) conventional analysis and (b) Q-Space analysis of a sphere with refractive index m=1.5 and various size parameters kR [*Sorensen and Fischbach*, 2000]. Unlike the conventional analysis yields no definable pattern, Q-space analysis shows forward scattering regime followed by a Guinier regime and a power law regime with quantifiable exponents.

1.2 The Scattering Matrix

Although the phase function is the most important scattering matrix element, our experimental apparatus was built to be capable of studying the whole scattering matrix (six independent scattering matrix elements – S_{11}, S_{12}, S_{22}, S_{33}, S_{34}, S_{44}). S_{12}, S_{22}, S_{33}, S_{34}, and S_{44} normalized by S_{11} are related to different degree of polarization. We will graph S_{12}, S_{22}, S_{33}, S_{34}, and S_{44} normalized by S_{11}. In this dissertation, we will present the measurements of all six scattering matrix elements for completeness for water droplets and Arizona Road Dust, in Chapter 2 and 3 respectively.

The intensity and polarization of a beam of light can be specified by a Stokes vector [*Hunt and Huffman*, 1973; *Kuik et al.*, 1991]

$$\begin{pmatrix} I \\ Q \\ U \\ V \end{pmatrix},$$

where I represents the total intensity, Q represents the difference between the horizontally and vertically polarized intensities, U represents the difference between the $+45^\circ$ and -45° polarized intensities, and V represents the difference between the right-handed and left-handed polarized intensities. I is always 1 because it is the total intensity. Each of the other three is between -1 and 1. For example, the Stokes vectors of an unpolarized light, a vertically polarized light, and a circularly polarized light are $\begin{pmatrix} 1 & 0 & 0 & 0 \end{pmatrix}^T$, $\begin{pmatrix} 1 & -1 & 0 & 0 \end{pmatrix}^T$, and $\begin{pmatrix} 1 & 0 & 0 & \pm 1 \end{pmatrix}^T$ respectively, where T is the transpose operator. In $\begin{pmatrix} 1 & 0 & 0 & \pm 1 \end{pmatrix}^T$, "+" represents right-handed and "–" represents left-handed.

The optical scattering information about a given particle is completely described by the 4 by 4 scattering matrix[*Hunt and Huffman*, 1973; *Kuik et al.*, 1991] The scattering process is a transformation of the incident Stokes vector to the scattering Stokes vector. The Stokes vector of the scattered light is obtained by multiplying the incident light Stokes vector by the 4 by 4 scattering matrix, expressed as

$$\begin{pmatrix} S_{11} & S_{12} & S_{13} & S_{14} \\ S_{12} & S_{22} & S_{23} & S_{24} \\ S_{31} & S_{32} & S_{33} & S_{34} \\ S_{41} & S_{42} & -S_{34} & S_{44} \end{pmatrix} \cdot \begin{pmatrix} I_{inc} \\ Q_{inc} \\ U_{inc} \\ V_{inc} \end{pmatrix} = \begin{pmatrix} I_{sca} \\ Q_{sca} \\ U_{sca} \\ V_{sca} \end{pmatrix}. \tag{1.2}$$

When the particles are randomly oriented they have a plane of symmetry, thus the scattering matrix has eight zero elements and eight nonzero elements

$$\begin{pmatrix} S_{11} & S_{12} & 0 & 0 \\ S_{21} & S_{22} & 0 & 0 \\ 0 & 0 & S_{33} & S_{34} \\ 0 & 0 & S_{43} & S_{44} \end{pmatrix},$$

where $S_{21} = S_{12}$and $S_{43} = -S_{34}$. Thus, six of the matrix elements are independent. This matrix applies to an ensemble of randomly oriented particles [*Mishchenko*, 2014].

By sending certain polarized light incident upon the particulate system and then detecting the difference between certain polarized scattered intensities, one can measure all six matrix elements [*Hunt and Huffman*, 1973; *Kuik et al.*, 1991]. We will graph S_{11} vs. q, $-S_{12}/S_{11}$ vs. θ, S_{22}/S_{11} vs. θ, S_{33}/S_{11} vs. θ, S_{34}/S_{11} vs. θ, and S_{44}/S_{11} vs. θ. S_{11} represents the total scattered intensity when the incident light is unpolarized or circularly polarized. The other five represent different degrees of polarization with corresponding polarized incident light. In later chapters, we will show that plotting S_{11} vs. q reveals power laws with quantifiable exponents for *all* particles;

thus achieving a universal description. In Chapter 5, we will show that the exponents of the power laws display a functionality with respect to the internal coupling parameter ρ' [*Heinson et al.*, 2015].

1.3 The internal coupling parameter ρ'

The internal coupling parameter incorporates the information on particle size and refractive index:

$$\rho' = 2kR\left|\frac{m^2-1}{m^2+2}\right|, \tag{1.3}$$

where R is the effective radius, e.g. volume equivalent radius of the particle, and $m = n + i\kappa$ is the particle's refractive index. We will show an undeniable trend in the absolute value of the power law exponents, under Q-space analysis, with respect to ρ' in Chapter 5. In recent work [*Heinson et al.*, 2016] it has been shown that patterns revealed by Q-space analysis are better parameterized by the internal coupling parameter ρ' than by the more widely known phase shift parameter

$$\rho = 2kR|m-1|, \tag{1.4}$$

which was used in previous work [*Sorensen and Fischbach*, 2000; *Berg et al.*, 2005; *Sorensen*, 2013b]. The phase shift parameter ρ describes the phase difference between a beam of light traveling through the diameter of the sphere and another that travels the same distance outside the sphere. In contrast ρ' is related to the Lorentz-Lorenz factor $\left|\frac{m^2-1}{m^2+2}\right|$ which is directly involved in the radiative coupling between the subvolumes that comprise the particle. When the coupling is strong, the field within the particle is no longer equal to the incident field hence the scattering

is no longer in the purely diffraction regime commonly called the Rayleigh Debye Gans (RDG) limit which occurs at small ρ' (and ρ). When in the RDG limit, the scattering is simple diffraction from the volume of the particle, and as such, the scattered intensity is the Fourier transform of the shape of the particle, squared. This new parameter ρ' was first realized by the need for spherical particle scattering to cross over from the small particle RDG limit to large particle Fraunhofer diffraction which is described by a two-dimensional circular obstacle. Note that both ρ' and ρ assume a homogeneous particle with regard to the refractive index m, although we expect that, if inhomogeneous, a Maxwell-Garnett average m [*Levy and Stroud*, 1997] would make a good approximation. All the non-fractal particles studied in this dissertation are homogeneous or to a very good approximation.

In this dissertation, we will, in Chapter 2, introduce the experimental apparatus we built which could measure all six matrix elements, although we put most of our effort on S_{11}. We will discuss the procedures to measure each element, explain in detail how the apparatus was calibrated, present the Guinier analysis which we used to determine particles sizes, and introduce the dust aerosol generation system which we used to blow Arizona Road Dust and Al_2O_3 abrasives powder. In Chapter 3, we will present the measurements of three different sizes of Arizona Road Dust (Ultrafine, Fine, and Medium) which is a canonical example of irregularly shaped particles similar to many other dusts that can be found in the atmosphere. We measured all six matrix elements, applied Guinier analysis to determine particle sizes, and examined the dust particles under an optical compound microscope. In Chapter 4, we will present the phase function measurements of six different grits of Al_2O_3 abrasive powders and the images under an optical compound microscope. We chose to study abrasive particles because they have irregular shapes, are readily available and can be obtained in a range of sizes as specified by the

manufacturer. The abrasives have a roughly spherical overall shape because of the way they are produced. We anticipate that scattering by abrasive particles might have some characteristics in common with scattering by spheres. Thus, after we determine particles sizes using Guinier analysis, we directly compared the scattering by the abrasives with scattering by spheres under the eye of Q-space analysis. In Chapter 5, we collected a large amount of experimental and theoretical phase function data from our group and others and applied Q-space analysis. Q-space analysis displayed a common scattering pattern which includes a q-independent forward scattering regime; a crossover, Guinier regime where $q \approx R^{-1}$; a power law regime with quantifiable expoenents; and sometimes an enhanced backscattering regime. Power law exponents show a quasi-universal functionality with respect to the internal coupling parameter ρ'. The absolute value of the exponents start from 4 when $\rho' < 1$, the diffraction limit, and decrease as ρ' increases until a constant 1.75 ± 0.25 when $\rho' \gtrsim 10$. In Chapter 6, we present the *in situ* measurements of soot fractal aggregates produced from a premixed burner. Soot fractal aggregates have completely different morphologies than other particles presented in this dissertation. With the help of our custom designed premixed burner combined with a suction nozzle, we were able to produce soot from a flame stable enough to measure the phase function. We also collected soot samples on a TEM grid and ran TEM imaging. In Chapter 7, we conclude this dissertation and briefly discuss possible future work.

Chapter 2 - Experiment

With the support of National science Foundation and US Army Research Laboratory we were able to initiate this project. The content of this chapter is based on [*Wang et al.*, 2015].

2.1. Experimental Apparatus

The experimental setup with major optical elements labeled is picture in Fig. 2.1. For a better view, Figure 2.2 displays a schematic diagram of the experimental apparatus. The laser (Coherent 532nm CW DPSS Sapphire) beam with $\lambda = 532$ nm passed through a linear polarizer (Thorlabs LPVISB100-MP) or a wave plate (Thorlabs $\lambda/2$ or $\lambda/4$ @ 532nm zero-order) on its way toward the aerosol from which it scattered. A linear polarizer or a wave plate was placed between the aerosol particles and the detector for both forward and side scattering. A linear polarizer passes light of a specific polarization and blocks other polarizations. A wave plate is also called a retarder which has a fast axis and a slow axis; light polarized along the fast axis encounters a smaller refractive index and travels faster through the wave plate than light polarized along the slow axis. This information is useful when we need to send different polarized incident light to obtain the six matrix elements. The forward scattering detection followed a design by Ferri [*Ferri*, 1997] with a beam stop placed at the focal point of a Fourier lens (Thorlabs AC508-100-A) to block the light directly from the laser. The beam stop was a 1.5 mm diameter drill bit with a 45° cut such that when the laser beam hit the 45° cut surface the surface worked as a mirror to reflect the laser beam upwards. Therefore the laser beam was stopped towards its way to the detector. The scattered light was collected by a lens (Thorlabs AC254-035-A) that imaged the Fourier plane onto the detector.

For the side scattering, a custom elliptical mirror (Optiforms 2753-0100-1300-0-00 ELLIPSE, AQ COATED) collected a wide range of angles. The intersection of the incident light and the aerosol was at one focal point of the elliptical mirror. An iris (Thorlabs SM1D12C) with 1mm opening was placed at the other focal point. This scattered light was then collimated by a lens (Thorlabs AC127-030-A). One 16 channel photodiode array (Hamamatsu S8558) for the forward direction and one 16 channel MPPC array (Hamamatsu C12677-03) for the side direction were used as detectors for a total of 31 angles. The forward scattering was bright enough to be detected with a low cost photodiode array but side scattering intensity droped fast with increasing scattering angles thus a more sensitive MPPC array was used for the side direction. One channel of the side detector was sacrificed as a monitor. The two detectors were connected to a data acquisition box connected to a computer. The 16 channel photodiode array and the 16 channel MPPC array had the exact same dimensions. The arrays detected light at many angles simultaneously which allowed for quick and efficient procurement of data, eliminated problems regarding aerosol stability, and made easier detection at small angles. The angles of the 16 channels in the forward direction and 15 channels at the side direction were determined from geometrical calculation. We also calibrated these angles, which is presented in section 2.2.

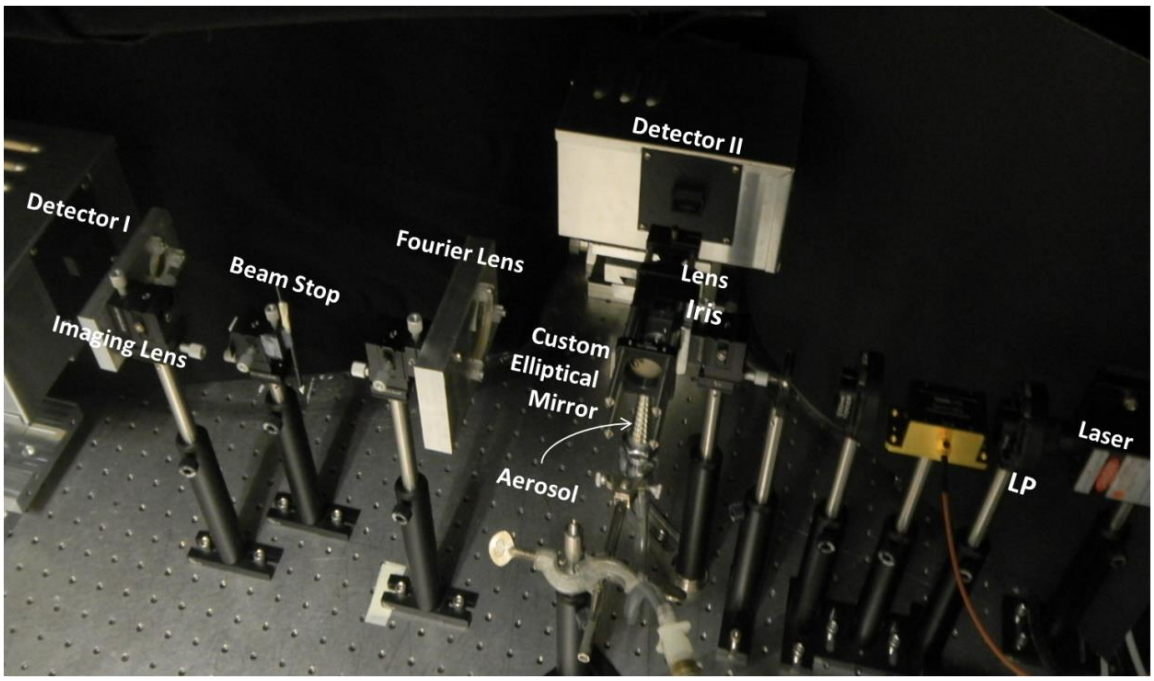

Figure 2.1 Picture of our experimental apparatus with major optical elements labeled.

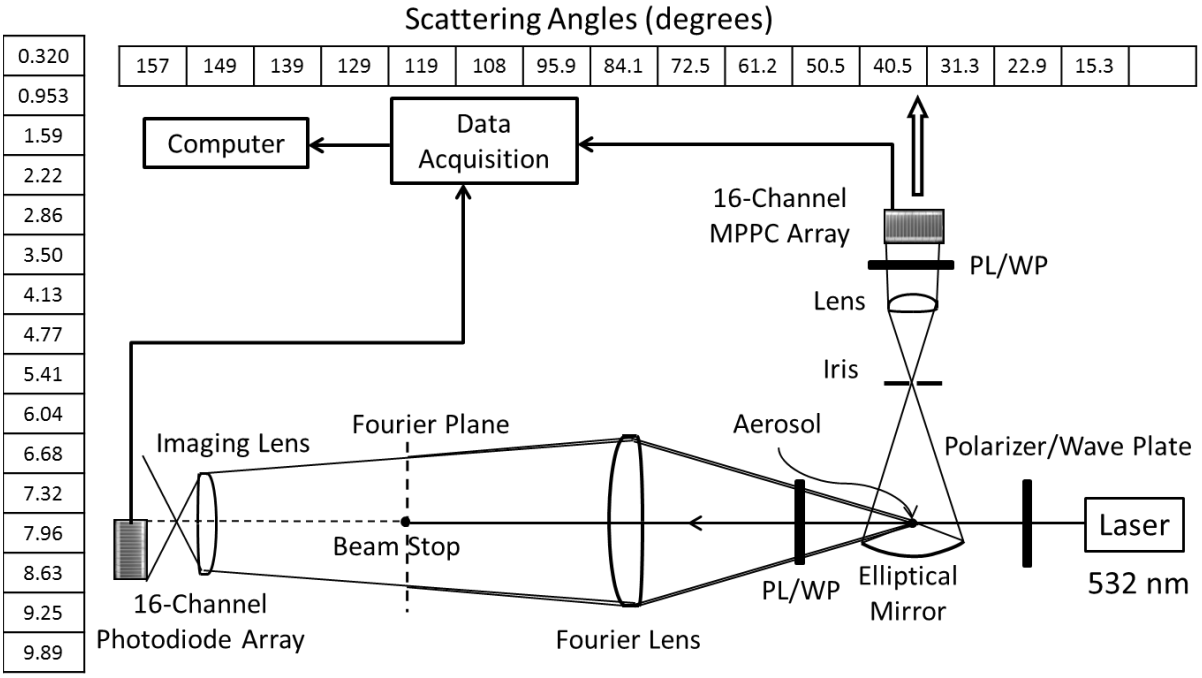

Figure 2.2 A schematic diagram of the experimental apparatus. The angle at the center of each channel on the detectors was labeled.

The Amsterdam-Granada group has studied a number of aerosol particles with an apparatus that allowed for measurements from 3° to 177° [*Munoz et al.*, 2000, 2001, 2002, 2004, 2006, 2007, 2012; *Volten et al.*, 2001, 2006; *Laan et al.*, 2009]. They had to move their detector along a ring surrounding the scattering sample from one scattering angle to the next. Our apparatus has advantage over other similar instruments such that it detected light at many angles simultaneously and was built to detect from a small angle of 0.32^{o} to 157^{o}, a factor of 10 decrease in the smallest forward angle. Detection at small angles was very important for measuring the light scattering properties of larger particles. We explain the reason in section 2.2.4 where we introduce Guinier analysis.

Our original plan was to use a polarizer and an electro-optic modulator (Thorlabs EO-AM-NR-C4) to send sinusoidally modulated polarized incident light into the scattering system but this setup proved unreliable. However, based on the information of the Stokes vector and the scattering matrix described in Chapter 1, section 1.2, we found that it was straightforward to send different polarized incident light by manipulating the polarizer and/or wave plates shown in Fig. 2.2; then we could obtain all the six matrix elements.

Consider the propagation of the laser beam along the z-axis, vertical from the optics table was the y-axis, and the x-axis was perpendicular to z-axis and parallel to the optics table. x-y-z obeys right-hand rule. To measure S_{11}, we sent right-handed circularly polarized light (produced by a $\lambda/4$ wave plate after the vertically polarized laser with fast axis $+45^{\circ}$ from vertical) and obtained the scattering Stokes vector from the scattering system. The procedure is expressed by Eq. (2.1):

$$\begin{pmatrix} S_{11} & S_{12} & 0 & 0 \\ S_{12} & S_{22} & 0 & 0 \\ 0 & 0 & S_{33} & S_{34} \\ 0 & 0 & -S_{34} & S_{44} \end{pmatrix} \cdot \begin{pmatrix} 1 \\ 0 \\ 0 \\ 1 \end{pmatrix} = \begin{pmatrix} S_{11} \\ S_{12} \\ S_{34} \\ S_{44} \end{pmatrix}, \tag{2.1}$$

where $(1 \quad 0 \quad 0 \quad 1)^T$ was the Stokes vector of the right-handed circularly polarized incident light. *T* was the transpose operator, same as mentioned in section 1.2. Recall that, for a Stokes vector, the four elements from top to bottom represent the total scattered intensity, the difference between the horizontally and vertically polarized intensities, the difference between the $+45^\circ$ and -45° polarized intensities, and the difference between the right-handed and left-handed polarized intensities, respectively. The detector, without a polarizer or a wave plate in front, detected the top element of a Stokes vector, the total scattered intensity, S_{11}. To measure S_{12}, we sent circularly polarized light and obtained the same Stokes vector, the same expression as Eq. (2.1). To determine the second element from the top, S_{12}, the difference between the vertically and horizontally polarized scattered intensities, we placed a linear polarizer with transmission axis vertically and then horizontally, in front of the detector. To measure S_{22}, we followed two procedures: first sent horizontally polarized light (λ/2 wave plate after the vertically polarized laser with fast axis 45° from vertical)

$$\begin{pmatrix} S_{11} & S_{12} & 0 & 0 \\ S_{12} & S_{22} & 0 & 0 \\ 0 & 0 & S_{33} & S_{34} \\ 0 & 0 & -S_{34} & S_{44} \end{pmatrix} \cdot \begin{pmatrix} 1 \\ 1 \\ 0 \\ 0 \end{pmatrix} = \begin{pmatrix} S_{11} + S_{12} \\ S_{12} + S_{22} \\ 0 \\ 0 \end{pmatrix}, \tag{2.2}$$

where $(1 \quad 1 \quad 0 \quad 0)^T$ was the Stokes vector of the horizontally polarized incident light, and measured the difference between horizontally and vertically polarized intensities $S_{12} + S_{22}$; second sent vertically polarized light (λ/2 wave plate with fast axis vertical)

$$\begin{pmatrix} S_{11} & S_{12} & 0 & 0 \\ S_{12} & S_{22} & 0 & 0 \\ 0 & 0 & S_{33} & S_{34} \\ 0 & 0 & -S_{34} & S_{44} \end{pmatrix} \cdot \begin{pmatrix} 1 \\ -1 \\ 0 \\ 0 \end{pmatrix} = \begin{pmatrix} S_{11} - S_{12} \\ S_{12} - S_{22} \\ 0 \\ 0 \end{pmatrix}, \tag{2.3}$$

where $\begin{pmatrix} 1 & -1 & 0 & 0 \end{pmatrix}^T$ ws the Stokes vector of the vertically polarized incident light, and measured the difference between horizontally and vertically polarized intensities $S_{12} - S_{22}$. With the values of $S_{12} + S_{22}$ and $S_{12} - S_{22}$, one can solve for S_{22}. One might ask why we placed the λ/2 wave plate with fast axis vertical to produce vertically polarized light, instead of simply removing the λ/2 wave plate to use the vertically polarized light directly from the laser. That is because using a λ/2 wave plate was the easiest way for us to obtain horizontally polarized incident light, which, however, attenuates the laser intensity; we wanted the incident intensities for both procedures in Eqs. (2.2) and (2.3) to be the same. To measure S_{33}, we sent $+45^\circ$ polarized light by placing a linear polarizer with transmission axis $+45^\circ$ from vertical

$$\begin{pmatrix} S_{11} & S_{12} & 0 & 0 \\ S_{12} & S_{22} & 0 & 0 \\ 0 & 0 & S_{33} & S_{34} \\ 0 & 0 & -S_{34} & S_{44} \end{pmatrix} \cdot \begin{pmatrix} 1 \\ 0 \\ 1 \\ 0 \end{pmatrix} = \begin{pmatrix} S_{11} \\ S_{12} \\ S_{33} \\ -S_{34} \end{pmatrix}, \tag{2.4}$$

where $\begin{pmatrix} 1 & 0 & 1 & 0 \end{pmatrix}^T$ was the Stokes vector of the $+45^\circ$ polarized incident light, and placed a linear polarizer with transmission axis $+45^\circ$ and -45° alternately to measure the difference between the $+45^\circ$ and -45° polarized intensities. To measure S_{34}, we sent right-handed circularly polarized light, the same expression as Eq. (2.1) and measured the difference between the $+45^\circ$ and -45° polarized intensities. To measure S_{44}, we again sent circularly polarized light, the same expression as Eq. (2.1); then we determined the bottom element, S_{44}, the difference between the right-handed and left-handed polarized intensities. It was straight forward

to understand that we used a linear polarizer placed at different angles relative to vertical to determine the horizontally, vertically, $+45^{\circ}$, and -45° polarized intensities. As for the procedure to determine S_{44}, the difference between the right-handed and left-handed polarized intensities, we addressed that each optical element had its own 4 by 4 Mueller matrix. The Mueller matrix of a linear polarizer is given as

$$M_P = \frac{1}{2}\begin{pmatrix} 1 & \cos 2\alpha & \sin 2\alpha & 0 \\ \cos 2\alpha & \cos^2 2\alpha & \sin 2\alpha \cos 2\alpha & 0 \\ \sin 2\alpha & \sin 2\alpha \cos 2\alpha & \sin^2 2\alpha & 0 \\ 0 & 0 & 0 & 0 \end{pmatrix}, \tag{2.5}$$

where α is the angel between transmission axis and x-axis; the Mueller matrix of a linear retarder, e.g. λ/4 and λ/2 wave plates, is given as

$$M_r = \begin{pmatrix} 1 & 0 & 0 & 0 \\ 0 & \cos^2 2\beta + \sin^2 2\beta \cos\delta & \sin 2\beta \cos 2\beta(1-\cos\delta) & -\sin 2\beta \sin\delta \\ 0 & \sin 2\beta \cos 2\beta(1-\cos\delta) & \sin^2 2\beta + \cos^2 2\beta \cos\delta & \cos 2\beta \sin\delta \\ 0 & \sin 2\beta \sin\delta & -\cos 2\beta \sin\delta & \cos\delta \end{pmatrix}, \tag{2.6}$$

where β is the angle between the fast axis and x-axis, and δ is the retarder phase, e.g. $\delta = \pi/2$ for λ/4 wave plate and $\delta = \pi$ for λ/2 wave plate. After the procedure expressed in Eq. (2.1), to determine S_{44}, we placed a λ/4 wave plate with fast axis $+45^{\circ}$ and -45° from vertical alternately right after the scattering volume; additionally we placed a linear polarizer with transmission axis vertically in front of the detector. Therefore the whole procedure is expressed as

$$\frac{1}{2}\begin{pmatrix} 1 & -1 & 0 & 0 \\ -1 & 1 & 0 & 0 \\ 0 & 0 & 0 & 0 \\ 0 & 0 & 0 & 0 \end{pmatrix}\begin{pmatrix} 1 & 0 & 0 & 0 \\ 0 & 0 & 0 & \mp 1 \\ 0 & 0 & 1 & 0 \\ 0 & 1 & 0 & 0 \end{pmatrix}\begin{pmatrix} S_{11} \\ S_{12} \\ S_{34} \\ S_{44} \end{pmatrix} = \frac{1}{2}\begin{pmatrix} S_{11} \pm S_{44} \\ -(S_{11} \pm S_{44}) \\ 0 \\ 0 \end{pmatrix}. \tag{2.7}$$

With the values of $S_{11} + S_{44}$ and $S_{11} - S_{44}$ one can solve for S_{44}. Therefore, we were able obtain all six independent scattering matrix elements, S_{11}, S_{12}, S_{22}, S_{33}, S_{34}, S_{44}. We graphed S_{12}, S_{22}, S_{33}, S_{34}, and S_{44} by S_{11}; this normalization S_{11} was obtained from each of the other five matrix elements measurement procedures. For example, when we measured S_{12}, we followed the procedure in Eq. (2.1) and then we placed a linear polarizer with transmission axis vertically and then horizontally in front of the detector to determine the difference between the vertically and horizontally polarized scattered intensities. In Eq. (2.1), S_{11} was still the top element of the Stokes vector , which represents the total scattered intensity; therefore we added up the vertically and horizontally polarized scattered intensities to obtain S_{11}.

Note that we used an elliptical mirror for the side scattering which meant we needed to consider the mirror effect – left becomes right and vice versa. If we placed a linear polarizer with transmission axis $+45^{\circ}$ and -45° from vertical (after the scattering system) for the forward scattering, we switched the two angles for the side scattering, i.e. -45° and $+45^{\circ}$; same for the λ/4 wave plate.

2.2. Calibrations

2.2.1 Forward scattering

Each angle labeled in Fig. 2.2, calculated according to the geometry and the arrangement of the apparatus, corresponded to the center of each channel. Since each channel has its width, each angle should have its angle spread. Table 2.1 shows the center angles and their spreads for the 16 channels and the corresponding q's and Δq's for the forward direction. The angle spreads are close to each other. A 10μm single slit was used to calibrate the forward scattering. Figure

2.3 shows that the experimental and theoretical patterns of single slit diffraction match well under Q-space analysis except for the theoretical minima because the photodiodes have finite angular width and are not sensitive enough to detect very low intensity. Figure 2.3 has q spreads calculated from the corresponding angle spreads $\Delta\theta$. Q-space analysis revealed a power law envelope with an exponent of -2 which was the expected value of $-(2D_m - D_s)$ [*Oh and Sorensen*, 1999] where D_m is the mass dimension and D_s is the surface dimension of the single slit (1 and 0, respectively). Thus, the forward scattering was calibrated.

Table 2.1 Center angles and their angle spreads for the 16 channel forward scattering detector.

θ (deg)	$\Delta\theta$ (deg)	q (cm^{-1})	Δq (cm^{-1})
0.320	0.556	6.55×10^2	1.15×10^3
0.953	0.556	1.96×10^3	1.15×10^3
1.59	0.556	3.27×10^3	1.15×10^3
2.22	0.556	4.58×10^3	1.15×10^3
2.86	0.556	5.89×10^3	1.15×10^3
3.49	0.557	7.20×10^3	1.15×10^3
4.13	0.557	8.51×10^3	1.15×10^3
4.77	0.558	9.83×10^3	1.15×10^3
5.41	0.558	1.11×10^4	1.15×10^3
6.04	0.559	1.25×10^4	1.15×10^3
6.68	0.559	1.38×10^4	1.15×10^3

7.32	0.560	1.51×10^4	1.15×10^3
7.96	0.561	1.64×10^4	1.15×10^3
8.61	0.562	1.77×10^4	1.16×10^3
9.25	0.563	1.90×10^4	1.16×10^3
9.89	0.564	2.04×10^4	1.16×10^3

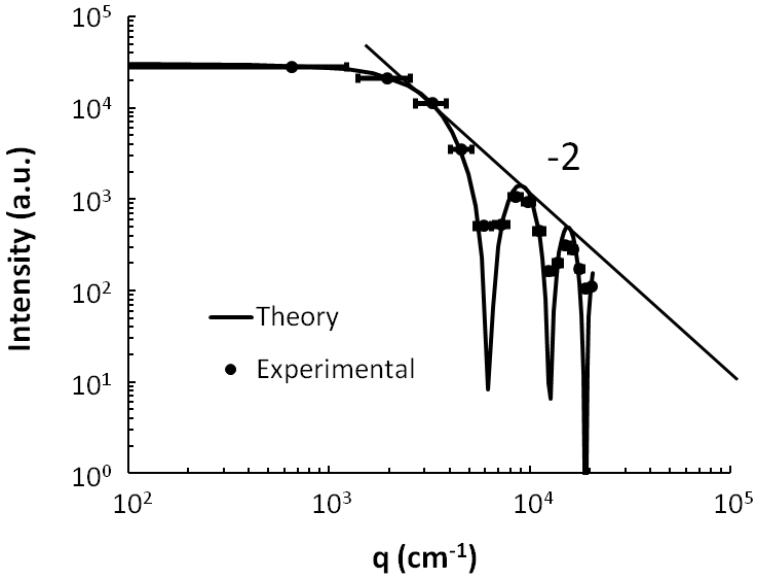

Figure 2.3 Single slit diffraction experimental and theoretical patterns for the forward direction. Intensity (arbitrary units) was plotted vs. q (cm^{-1}). The -2 slope line indicated the power law envelope of the theoretical curve.

2.2.2 Side scattering

The custom elliptical mirror maximized the angle detection range – 15.3° to 157°, and left space between the edge of the mirror and the scattering system which was at the focal point near to the elliptical mirror. Therefore, when we measured of soot particles freshly produced from a burner placed very close to the mirror, the mirror will not get extremely hot to cause

deformation of the mirror. We discuss soot particles in detail in Chapter 6. Figure 2.4(a) showed the geometry of the ellipse that our elliptical mirror was part of. Figure 2.4(b) shows the mechanical drawing of the elliptical mirror. Note that the elliptical mirror was a 3 dimensional object. The drawing of Fig. 2.4(b) was a cut along the axis of the revolution of the mirror. According to the custom geometry of the elliptical mirror, the geometry of the MPPC, and the arrangement of the whole side scattering setup, we calculated the angles at the centers of the 15 channels and the angle spreads and their corresponding q's and Δq's as shown in Table 2.2. Before we designed the custom elliptical mirror, we tested the method of elliptical mirror collecting wide scattering angle, with another elliptical mirror that Optiforms had in stock. The Optiforms mirror worked; therefore we were willing to spend for money to design our own mirror to maximize the scattering angle collection range.

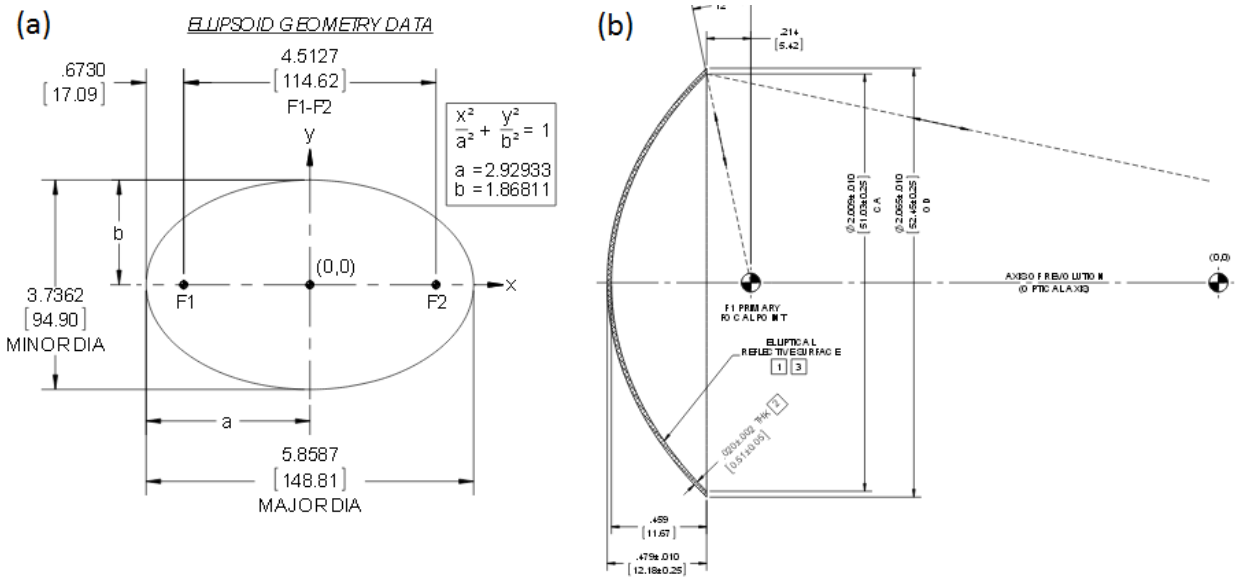

Figure 2.4 (a) Geometry of the ellipse that the elliptical mirror was part of it; (b) the mechanical drawing of the elliptical mirror.

Table 2.2 The angles at the centers of the 15 channels and the corresponding angle spreads.

θ (deg)	$\Delta\theta$ (deg)	q (cm^{-1})	Δq (cm^{-1})
15.3	6.32	3.15×10^4	1.29×10^4
22.9	7.00	4.69×10^4	1.41×10^4
31.3	7.70	6.38×10^4	1.53×10^4
40.5	8.41	8.18×10^4	1.62×10^4
50.5	9.06	1.01×10^5	1.69×10^4
61.2	9.63	1.20×10^5	1.71×10^4
72.5	10.0	1.40×10^5	1.67×10^4
84.1	10.3	1.58×10^5	1.57×10^4
95.9	10.3	1.75×10^5	1.42×10^4
108	10.0	1.91×10^5	1.22×10^4
119	9.63	2.03×10^5	1.01×10^4
129	9.06	2.14×10^5	7.98×10^3
139	8.41	2.22×10^5	6.01×10^3
148	7.70	2.27×10^5	4.30×10^3
157	7.00	2.31×10^5	2.88×10^3

To experimentally calibrate our side scattering setup, we placed a 5mm in diameter glass dropper vertically at the scattering volume position. The glass dropper was filled with glowing agent from a glow stick. Figure 2.5 (a) shows a top view of this calibration arrangement. The

glowing agent was bright enough to give a high signal/noise ratio. Theoretically, the glowing glass dropper should emit light uniformly along the angles, and indeed, the detector observed angle independent intensities as shown in Fig. 2.5 (b) except for the angles near 90°.

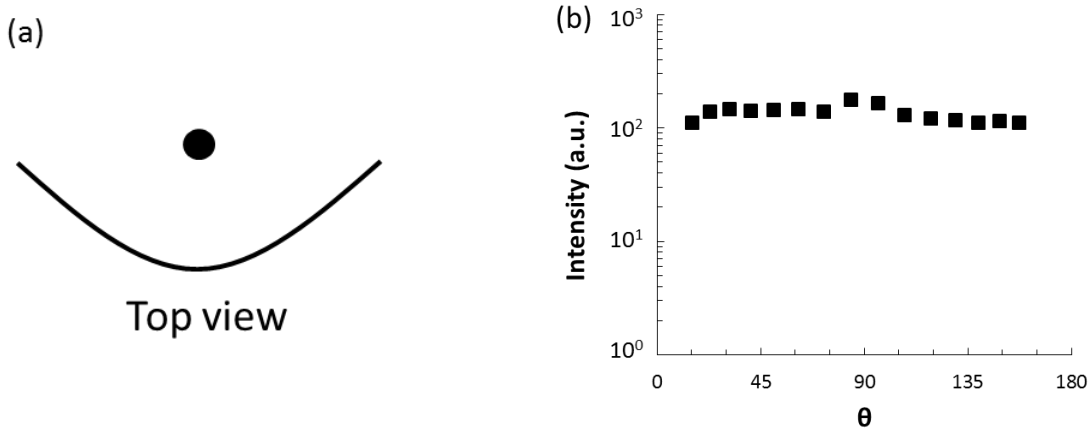

Figure 2.5 (a) A top view of the calibration method where the grass dropper was filled with glowing agent; (b) angle independent intensities of the glass dropper.

In our experiments, the aerosol particles come out of a copper tubing with 3mm inner diameter. The laser beam passed through the aerosol stream and illuminated the scattering system of a 1mm in diameter and 3mm long cylindrical bright bar, along the laser propagation direction, a top view as shown in Fig. 2.6(a). Our next step was to put a glowing shape which was close to our scattering volume shape at the focal point of the elliptical mirror. Therefore, we used a capillary to simulate the case. The capillary was a 7.5cm long tube with 1.5mm in diameter. We left one end (3mm) of the capillary clear and black taped the rest; filled the capillary with glowing agent and placed the capillary horizontally as shown in Fig. 2.6(b) and(c) alternately. Due to the black tape, for Fig. 2.6(b), we picked up the scattering data of angles less than 90°; for Fig. 2.6(c), we picked up the scattering data of angles greater than 90°. Combining the two sets of data, the detector showed uniform intensities along the angles as shown in Fig.

2.7, except for the angles near 90°. The angles near 90° in Figs. 2.5(b) and 2.7 were affected by the glass dropper and capillary respectively which block the reflected light from the mirror at 90°. They are not reflecting the real experimental situation where the scattering volume is made of aerosolized particles. Hence, based on the relative flat intensities in Fig. 2.5(b) and Fig. 2.7 neglecting the angles near 90°, we experimentally proved our side scattering setup did not need corrections.

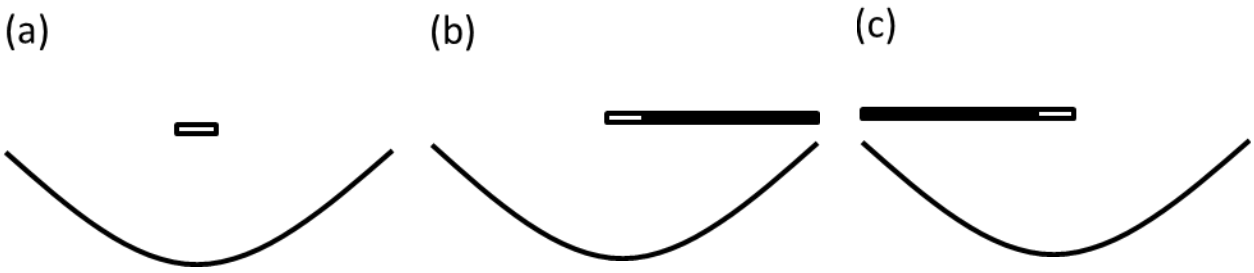

Figure 2.6 (a) A top view of our real scattering situation. Using capillary filled with glowing agent to simulate our actual scattering shape, we combined (b) and (c) to get the calibration done.

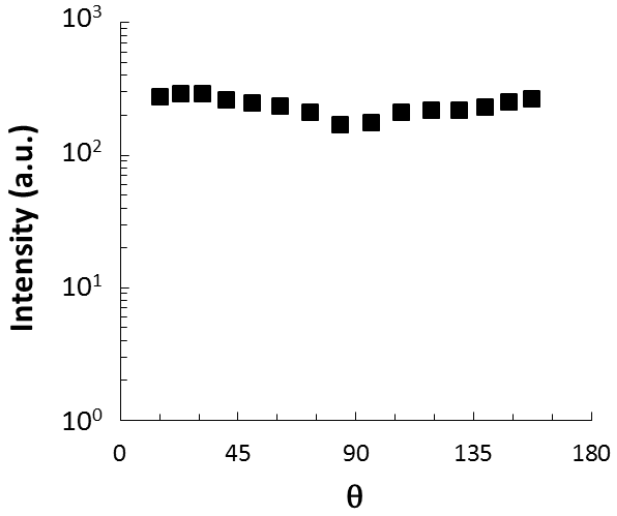

Figure 2.7 Uniform intensities along the angles for the capillary calibration method.

Based on the two experimental calibrations of our side scattering setup discussed above, additionally, for completeness, we also theoretically calculated if each channel at the detector collected the same amount of light. For our experiment, we placed an iris with 1mm opening at the farther focal point from the elliptical mirror. This 1mm opening determined the subtended angle to the near focal point, by connecting the edges of the 1mm to a picked point of the mirror and their reflected rays, for example, shown as the red and blue ray tracing lines in Fig. 2.8. Each picked point of the mirror corresponded to a specific scattering angle. Each pair of reflected rays (the pair in red or blue) and the shape of the scattering system located at the near focal point will determine the subtended area. The subtended area determined the amount of light seen at each scattering angle. Therefore, we needed to examine if the subtended area changes with angles. We enlarged the 1mm opening dramatically so one can see the ray tracing clearly. Since we applied two calibration methods for the side scattering, we discussed them separately.

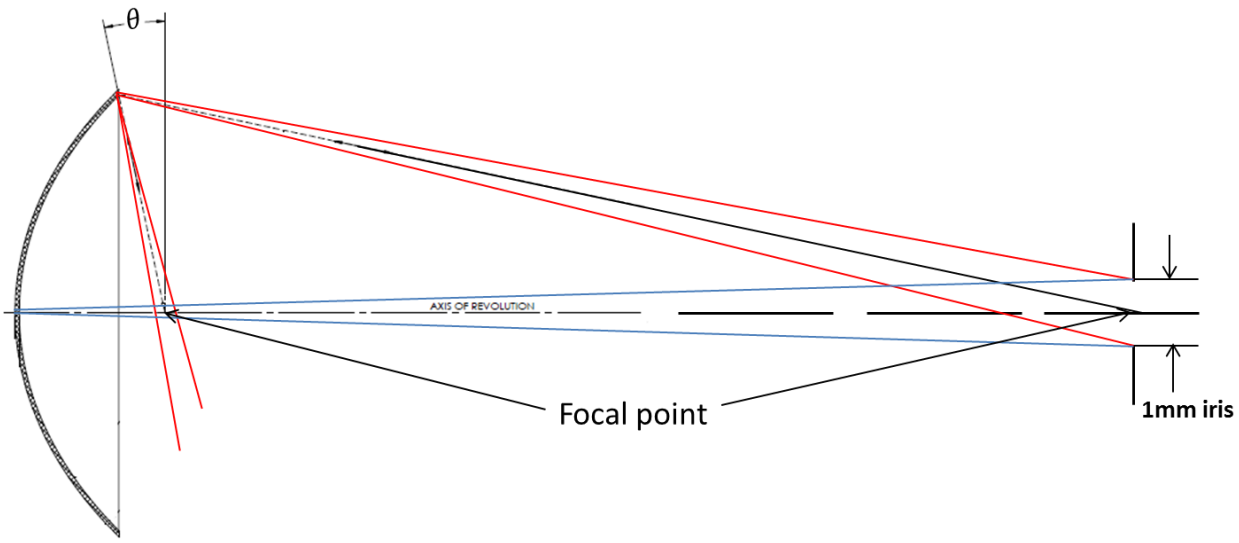

Figure 2.8 The 1mm iris determined the subtended amount of the scattering volume by connecting the edges of the iris to a picked up point of the mirror and their reflected rays.

First, for the case where the glowing glass dropper was placed vertically, the patches in red (a) and blue (b) formed by the reflected rays and glass dropper, corresponded to different scattering angles (Fig. 2.9). We only compared the lengths of the center black bars in Fig. 2.9(a) and (b), in order to compare the patches areas, because the shape of the patches was close to trapezoid and the two trapezoids have the same height – the diameter of the glass dropper. The black bar was crossing the center of the glass dropper overlapped the near focal point of the mirror and always perpendicular to the line that was connecting the corresponding point on the mirror and the near focal point. With the geometry of the ellipse shown in Fig. 2.9, we labeled some length scales and angles which will be used in Eq. (2.8) – (2.11).

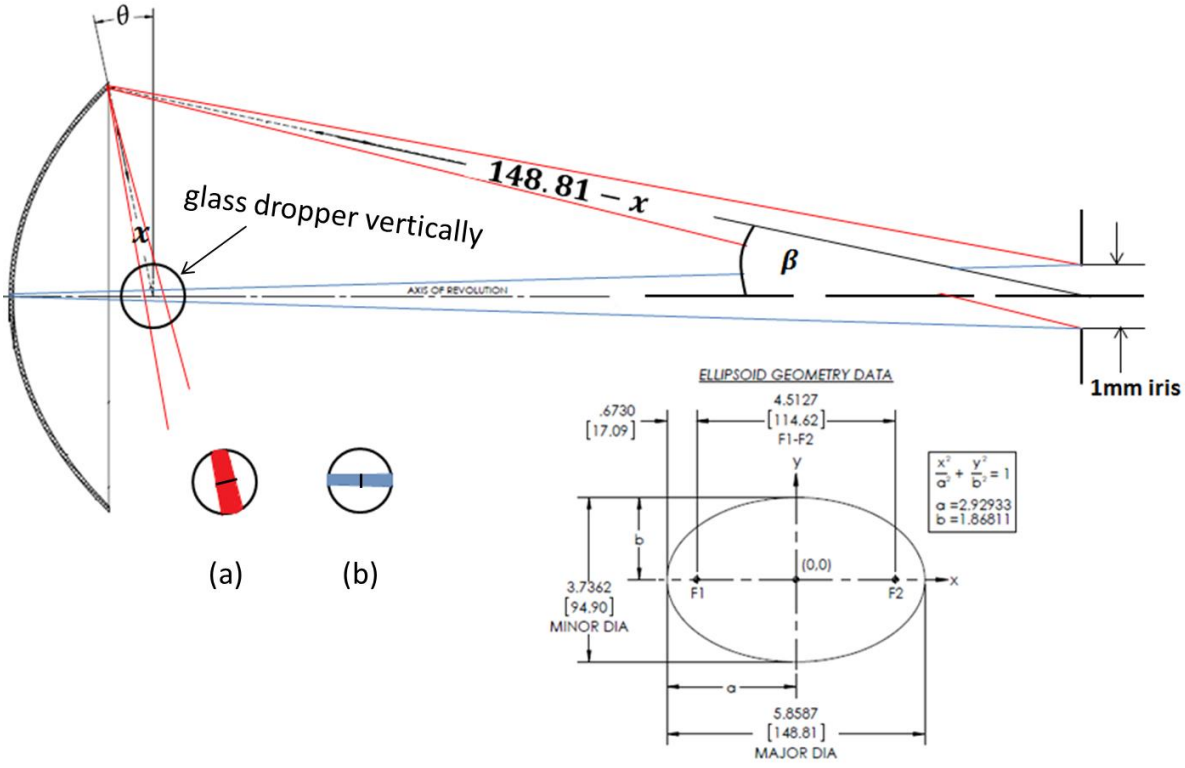

Figure 2.9 Glowing glass dropper placed vertically. The subtended areas in red (a) and blue (b), formed by the reflected rays and glass dropper, correspond to different scattering angles. The black bars in (a) and (b) are crossing the center of the glass dropper overlapped the near focal point of the mirror. Each black bar was perpendicular to the line that connected the focal point and ray-tracing back point on the mirror.

We determined how the length of the black bar changes with respect to the scattering angle. Assuming the distance between near focal point to a point on the mirror is x with scattering angle θ, the distance between the point on the mirror and the far focal point was $148.81 - x$ because $2a = 148.81$ (the long axis of the ellipse), according to the dimension of the mirror. The following calculations were also considered when we designed the mirror.

$$(x\,cos\,\theta)^2 + (x\,sin\,\theta + 114.62)^2 = (148.81 - x)^2 \tag{2.8}$$

x can be solved,

$$x = \frac{9006.67}{(229.24\sin\theta + 297.62)} \tag{2.9}$$

Now, we assumed the length of the black bar was d. Then,

$$\frac{x}{148.81 - x} = \frac{d}{1 \cdot \cos\beta}, \tag{2.10}$$

where

$$\cos\beta = \frac{(x\sin\theta + 114.62)}{(148.81 - x)} \tag{2.11}$$

The "1" in the denominator of Eq. (2.10) indicated the opening of the iris, 1mm. Therefore, d can be determined. We chose five different θ's and calculated their corresponding d's (Table 2.3). d was obviously changing with respect to θ. It appears that our setup would have an issue that an increasing or decreasing volume of the scattering system was seen. However, we have to consider each θ at the detector has its own angle spread $\Delta\theta$. Greater angle spread means collecting more light. Using the angle spread $\Delta\theta$ at each θ shown in Table 2.2, we found that the product $d \times \Delta\theta \approx 1.3$, the same for all θ, as shown in Table 2.3.

Table 2.3 Scattering angles θ and their corresponding subtended d for the case where a glowing glass dropper was placed vertically. We also included $\Delta\theta$ from Table 2.2 and calculated $d \times \Delta\theta$ which was nearly constant.

θ (deg)	d (mm)	$\Delta\theta$	$d \times \Delta\theta$
15	0.20	6.32	1.26
23	0.18	7.00	1.26
40	0.16	8.41	1.35
60	0.14	9.63	1.35
84	0.13	10.3	1.34

For the glowing glass dropper placed vertically, d was proportional to the subtended area. Thus we concluded that subtended area compensated the angle spread at the detector $\Delta\theta$ indicating each channel of the detector collected the same amount of light; therefore no correction was need. Hence, we have theoretically proved the vertical glass dropper calibration method.

Next, let us consider the case where the glowing capillary was placed horizontally. Similarly, the subtended areas, the patches in red and blue in Fig. 2.10(a) and (b), formed by the reflected rays and the capillary, corresponded to different scattering angles. The shape of the patches was trapezoidal with the same height – the diameter of the capillary. We only need to compare the lengths of the center black bars in Fig. 2.10(a) and (b) which were proportional to the areas of the patches. We need to address the fact that, different than the previous case, the black bar was always perpendicular to the axis of the revolution of the mirror. With the geometry

of the ellipse shown in Fig. 2.10, we labeled some length scales and angles which was used in Eq. (2.12) – (2.16).

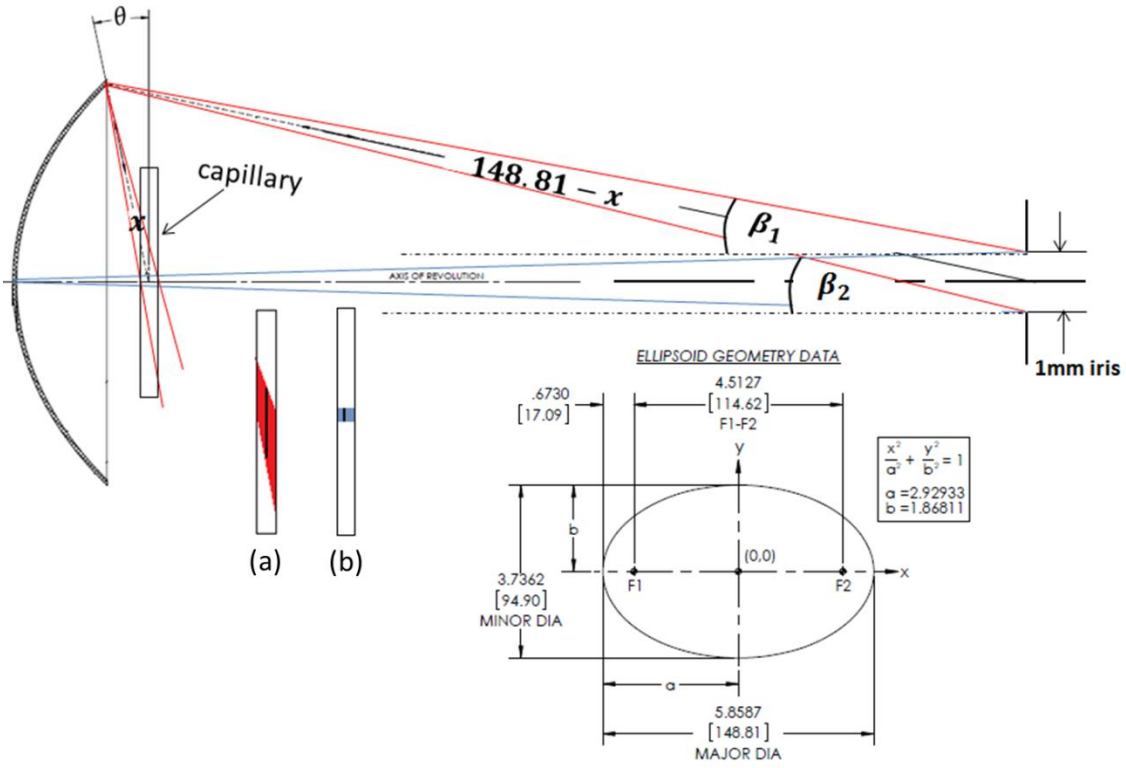

Figure 2.10 Glowing capillary placed horizontally. The subtended areas in red (a) and blue (b), formed by the reflected rays and the capillary, correspond to different scattering angles. The black bars in (a) and (b) were crossing the near focal point perpendicular to the axis of the revolution of the mirror.

Again, we need to determine how the length of the black bar changes with scattering angle and again we assumed the length of the black bar was d which can be calculated by the following equations:

$$\frac{x\cos\theta - 0.5}{x\sin\theta + 114.62} = \sin\beta_1 \tag{2.12}$$

$$\frac{x\cos\theta + 0.5}{x\sin\theta + 114.62} = \sin\beta_2 \tag{2.13}$$

$$\theta_1 = \theta - \left|\frac{\beta_1 - \beta_2}{2}\right| \tag{2.14}$$

$$\theta_2 = \theta + \left|\frac{\beta_1 - \beta_2}{2}\right| \tag{2.15}$$

$$d = \left|\frac{x \sin\theta}{\tan\theta_1} - \frac{x \sin\theta}{\tan\theta_2}\right| \tag{2.16}$$

Furthermore, in order to determine the observed intensity we considered Lambert's Cosine Law [*Lambert and Anding*, 1892] since in our case the observer (each scattering angle on the mirror) was off-normal relative to the scattering system. Figure 2.11 represents the adapted Lambert's Cosine Law for our case where the glowing capillary was placed horizontally.

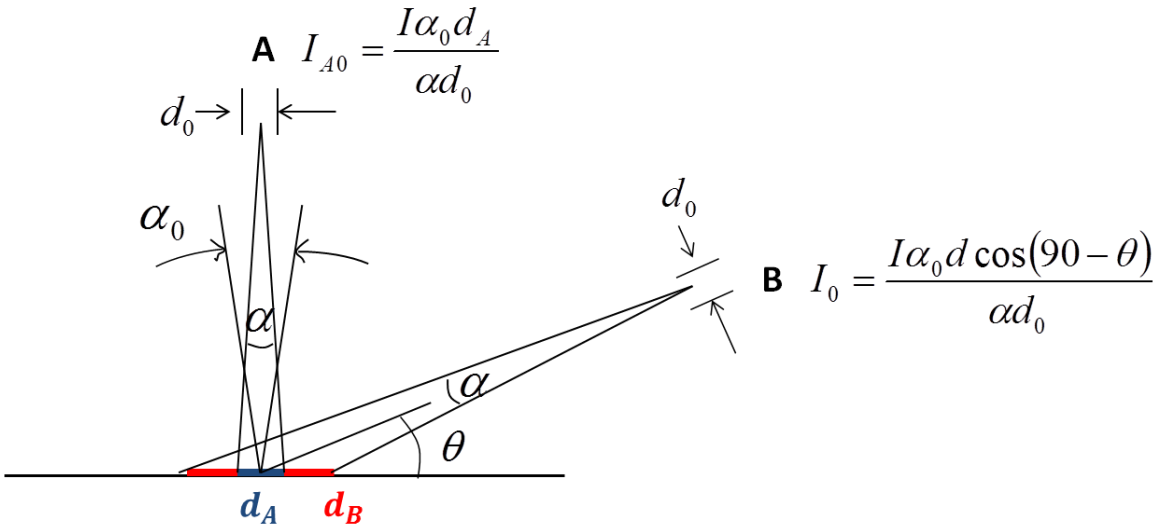

Figure 2.11 Lambert's Cosine Law for glowing capillary placed horizontally. A was a normal observer; B was off-normal observer, which is our case. At an arbitrary angle, I, α_0, α, and d_0 were constants; thus the observed intensity I_0 only depended upon $d\cos(90-\theta)$.

A was a normal observer; B was an off-normal observer, which was our case. We determined the subtended angles of observer A and observer B were the same, $\alpha_A = \alpha_B = \alpha$, after the calculations using Eqs. (2.12) – (2.16). Observer A sees d_A of the glowing capillary;

observer B sees d which we consider as a general case. Assume I (photons/(s·m·rad)) was the radiance of the glowing capillary along the normal and α_0 was the angle of the vertical wedge that the radiance propagates into. Therefore $I\alpha_0 d\cos(90-\theta)$ was the number of photons per second emitted from d into a wedge with the same angle α_0, at scattering angle θ. Assume d_0 was the window width that the observer is seeing through; d_0 was the same for all the scattering angles. With α the subtended angle, the observed intensity at B is expressed as

$$I_0 = \frac{I\alpha_0 d\cos(90-\theta)}{\alpha d_0} \tag{2.17}$$

For observer A, $\theta = 90^{\circ}$, then

$$I_{A0} = \frac{I\alpha_0 d_A}{\alpha d_0} \tag{2.18}$$

At an arbitrary angle, I, α_0, α, and d_0 are constants; thus the observed intensity I_0 only depends upon $d\cos(90-\theta)$.

Again, we chose five different θ's and calculated their corresponding d's using Eqs. (2.12) – (2.16) and $d\cos(90-\theta)$'s, see Table 2.4. Again, compared to the angle spread at each θ shown in Table 2.2, $d\cos(90-\theta)\times\Delta\theta \approx 1.34$ as shown in Table 2.4. Therefore, we theoretically proved the capillary calibration method as well.

Table 2.4 Scattering angles θ and their corresponding subtended d and $d\cos(90-\theta)$ and for the case where a glowing capillary placed vertically.

θ (deg)	d (mm)	$d\cos(90-\theta)$	$\Delta\theta$	$d\cos(90-\theta)\times\Delta\theta$
15	0.82	0.21	6.32	1.33
23	0.49	0.19	7.00	1.33
40	0.25	0.16	8.41	1.35

60	0.16	0.14	9.63	1.35
84	0.13	0.13	10.3	1.34

2.2.3 Connecting forward and side scattering

After the calibration of forward and side scattering separately, we need to connect the two. We measured S_{11} of water droplets produced from an atomizer. The diamonds shown in Fig. 2.12(a) were the original data from apparatus arrangement shown in Fig. 2.2. A multiplication factor was necessary to connect the forward and side scattering. Furthermore, the first channel on the side detector was found to give a low signal which means another multiplication factor was needed for that channel. Figure 2.13 shows the setup used to determine those two calibration factors. We placed two mirrors to direct the laser beam such that 0° scattering angle was offset by 6.48°. Thus, the side scattering detector included an angle, 8.82°, which was in the angle range of the front scattering detector.

The setup in Fig. 2.13 was used to measure S_{11} of water droplets (Fig. 2.12a). By comparing the side scattering of both setups (Fig. 2.2 and Fig. 2.13), the calibration factor was determined for the first channel on the side detector. The channels 10 and 11 (open circles) on the side detector had the same problem as the first channel. Thus the same correction method applied to channel 1 was applied to channel 10 and then channel 11. In Fig. 2.12(b), the side scattering was calibrated. Compare the forward scattering from setup in Fig. 2.2 and side scattering of setup in Fig. 2.13 which included an angle in the forward scattering range, the calibration factor to connect the side scattering to the front scattering was determined. Figure 2.12(c) shows the final graph after all the corrections.

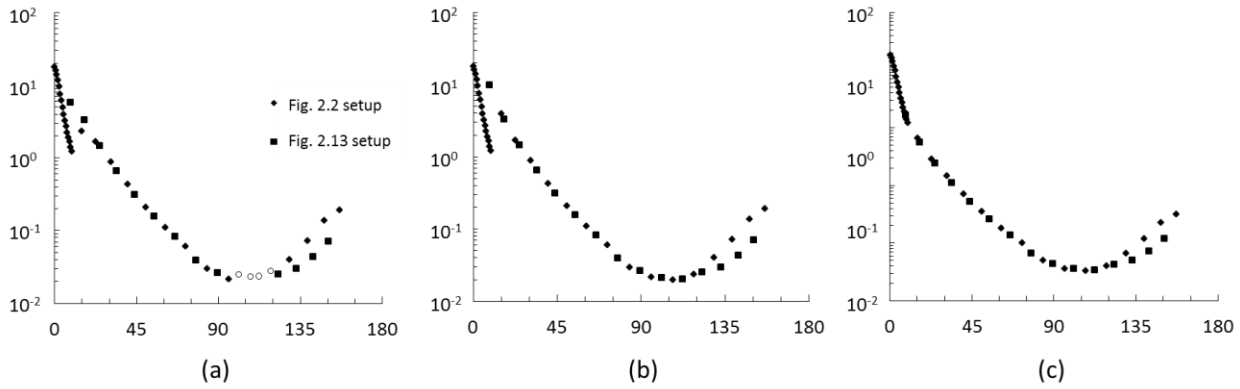

Figure 2.12 A calibration of the whole system by measuring S_{11} of water droplets using setup shown in Fig. 2.2 and Fig. 2.13. The S_{11} (arbitrary units) was plotted vs. the scattering angle. (a) Scattering data from the two setup. (b) Side scattering was calibrated be comparing the data from the two setups. (c) Forward and side scattering were connected.

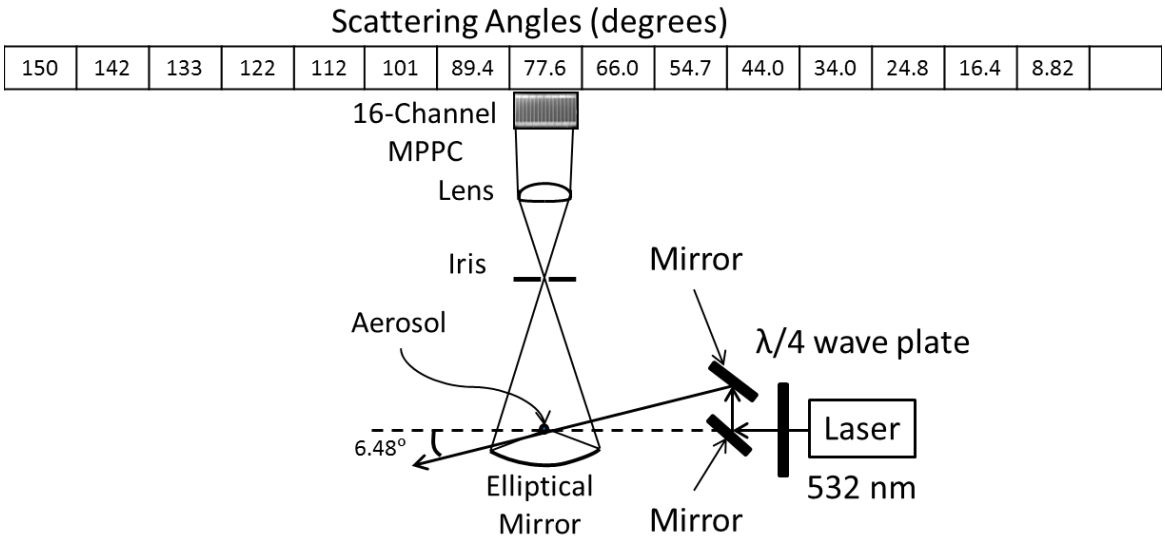

Figure 2.13 A schematic of the calibration to connect forward scattering and side scattering.

2.2.4 Water droplets

Figure 2.14 shows the experimental data of S_{11} (solid circles) for water droplets under the Q-space analysis. We normalized S_{11} to 1 at the smallest q or angle. S_{11} experimental data shows

two lines which have power laws of q^{-2} and q^{-4}**.** Here, we introduce $P(R)$ which is the unnormalized log-normal size distribution given by

$$P(R) = exp(-ln^2(R/R_0)/2ln^2\sigma), \tag{2.20}$$

where R_0 is the most probable radius and σ is the geometric width of the size distribution [*Sorensen*, 2001]. Fitting our experimental data for S_{11} with the theoretical Mie code [*Bohren and Huffman*, 1998] (solid line) averaged over the size distribution yielded a best fit weighted mean radius of our water droplets to be 1.1μm with a geometric width of 1.5 for a log-normal distribution. A multiplication factor applied to the original theory curve made the theoretical S_{11} normalized to 1 at the smallest q. The theory showed an obvious dip at $q \approx 30{,}000cm^{-1}$ but not observed with our experiment data. We speculated that the lack of the dip of our experiment is possibly due to the non-sphericity of our water droplets based on our recent incipient theoretical calculations for slightly aspherical drops that show lessened dips.

To verify that the experiment was carried out in the single scattering limit, a power meter was placed after the aerosol to detect the power before and after the aerosol was turned on.

$$I = I_0 e^{-<s>}, \tag{2.21}$$

where I is the power for the aerosol on, I_0 is the power for the aerosol off, and $< s >$ is the average number of scattering events [*Mokhtari et al.*, 2005]. In our case, the power for the aerosol on was 92.3% of the power for the aerosol off, thus the average number of scattering events $< s >$was 0.08. Since multiple scattering events were distributed by a Poisson distribution [*Mokhtari et al.*, 2005], this low value indicated the experiment was under the single scattering limit.

Our experimental apparatus can measure all six matrix elements. Figure 2.13 shows the six matrix elements vs. the scattering angle θ for the water droplets. The uncertainties of the matrix elements were within the size of the solid circles. The uncertainty of each angle was due to the width of each channel of the detectors. Compared to Q-space analysis, the scattered intensity S_{11} does not have any quantifiable exponent to describe the trend (Fig. 2.15a). The non-sphericity of our water droplets was supported by the decrease in S_{22}/S_{11} from unity as the scattering angle increased (Fig. 2.15c). For spheres, S_{22}/S_{11} is unity along the angles. Our recent incipient theoretical work has shown that even a few percent of deviation from spheres can cause a significant change in the matrix elements. A reason for the non-sphericity of our water droplets was that the water droplets coming out of the atomizer might oscillate with certain modes. Future work will investigate these possibilities.

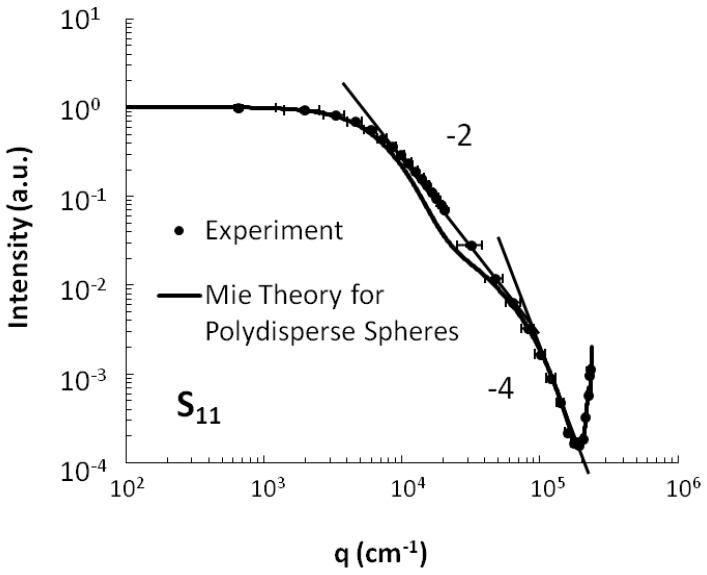

Figure 2.14 Experimental water droplet S_{11} data compared to Mie theory for perfect, polydisperse spheres with weighted mean radius of 1.1μm and a geometric width of 1.5 for a log-normal distribution. S_{11} was normalized at the smallest q.

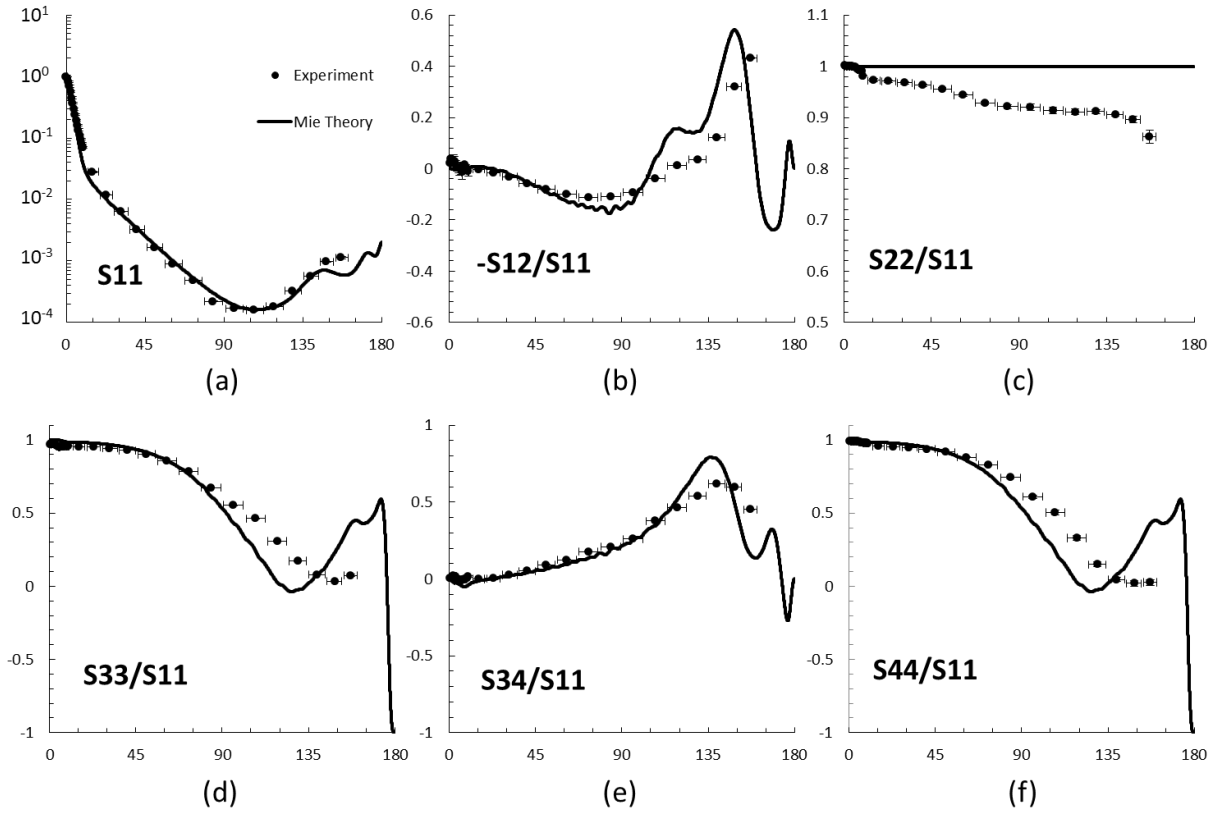

Figure 2.15 The scattering matrix elements vs. the scattering angle θ for water droplets produced from an atomizer compared to Mie theory. S_{11} is normalized at the smallest angle.

We compared our data with the Amsterdam-Granada group's water droplets experimental data at $\lambda = 441.6nm$ and $632.8nm$ [*Volten et al.*, 2001] (Fig. 2.16). The colors of the data are close to the wavelengths. S_{11} was normalized to 1 at 30° (the Amsterdam-Granada group always normalize S_{11} to 1 at 30°). Our water droplets experimental data agreed well with the Amsterdam group's water droplets data. Taking into consideration possible nonsphericity of our water droplets, we consider our apparatus to be well calibrated.

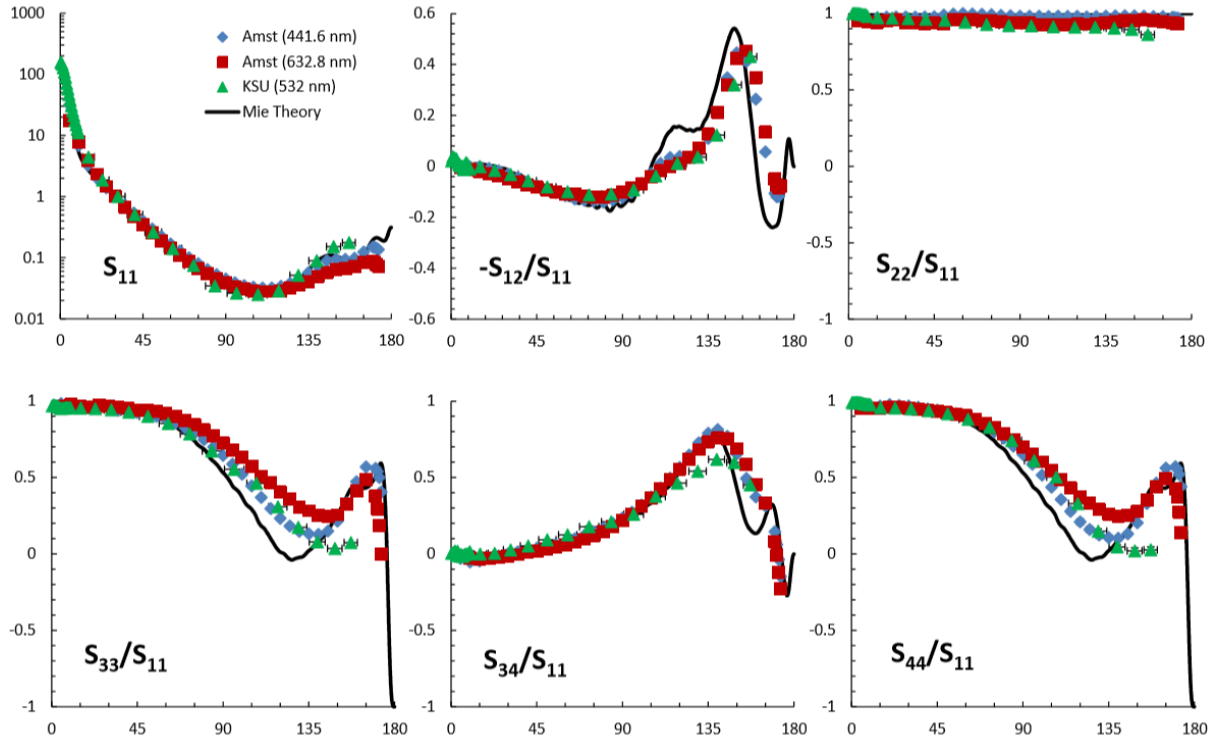

Figure 2.16 The scattering matrix elements vs. the scattering angle θ for water droplets from our group at $\lambda = 532nm$ and the Amsterdam-Granada group at $\lambda = 441.6nm$ and $632.8nm$. S_{11} is normalized at 30°.

In Figs. 2.14 – 2.16, the error bars along the horizontal axis was calculated according to the dimensions of detector channels; the error bars along the vertical axis are the standard deviations from three measurements. The vertical error bars were hidden behind some of the data points.

Returning to Fig. 2.14 we see that the Q-space analysis of the water droplet data for the scattered intensity, S_{11}, shows power laws with exponents of -2 and -4. These power laws lie in the region beyond the forward scattering lobe and the Guinier regime but before the backscattering regime where the scattering was enhanced. This confirms the same patterns seen

by Q-space analysis of spherical particle scattering obtained theoretically from the Mie code [*Sorensen and Fischbach*, 2000; *Berg et al.*, 2005].

Based on the Q-space analysis, regardless of the shape of the particle, one can determine the radius of gyration R_g of the particle by doing Guinier analysis, which is exactly definable for any shape as

$$R_g^2 = \int_0^R r^2 \rho(\vec{r}) d^3r / \int_0^R \rho(\vec{r}) d^3r, \tag{2.22}$$

where $\rho(\vec{r})$ is the mass density at position $\vec{r}$ of an object. For a sphere with radius of gyration R_g the Guinier equation is [*Guinier et al.*, 1955]

$$I(q) = I(0)\left(1 - q^2 R_g^2/3\right). \tag{2.23}$$

Guinier analysis was applicable when $qR_g < 1$, although one can often exceed this limit [*Guinier et al.*, 1955]. At the limit where $qR_g = 1$, $I(q)$ is 2/3 of $I(0)$. In Fig. 2.14, at 2/3 of the maximum intensity, the corresponding q indicates that $R_g = 2.4\mu m$. When qR_g is very small, Eq. (2.23) can be rewritten as

$$I(0)/I(q) = \left(1 + q^2 R_g^2/3\right). \tag{2.24}$$

Thus the slope of $I(0)/I(q)$ versus q^2 is $R_g^2/3$, and the data were plotted in this manner to find a measured radius of gyration of $R_g = 2.5\mu m$ (Fig. 2.17). On average, the measured radius of gyration is 2.45μm. By multiplying R_g by $\sqrt{5/3}$, the measured geometric radius is $R = 3.2\mu m$. The measured radius was a significant discrepancy from 1.1μm obtained from the Mie code discussed previously.

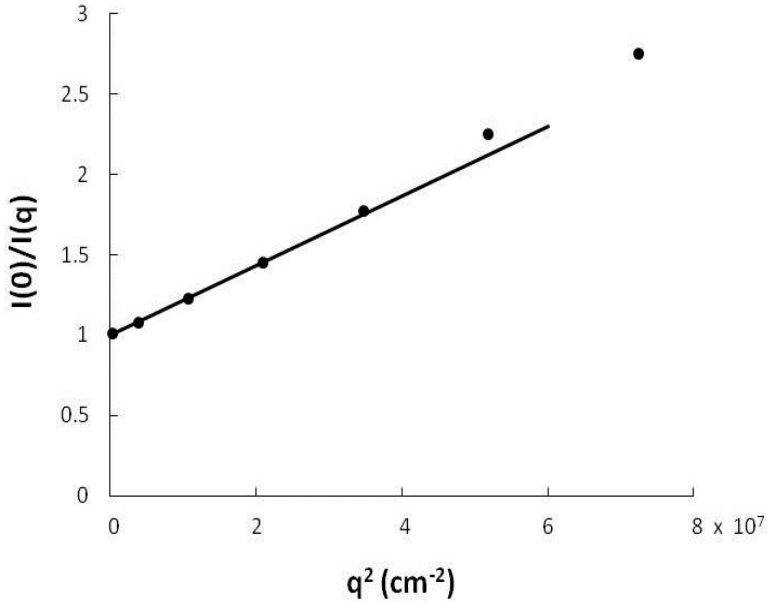

Figure 2.17 Guinier analysis of water droplet.

However, there were more subtle effects on the Guinier analysis for refractive particles which are identified as having a phase shift parameter as given in Eq. (1.4) where $m > 1$. These effects were first identified in [*Sorensen and Shi*, 2000]; we applied the effects for the first time in what we will call the Extended Guinier Analysis. The radius of gyration determined from the Guinier analysis, $R_{g,G}$, is not equal to the true radius of gyration, R_g, when $\rho > 1$. Figure 2.18 shows the ratio $R_{g,G}/R_g$ vs. ρ for monodisperse water droplets [*Sorensen and Shi*, 2000].

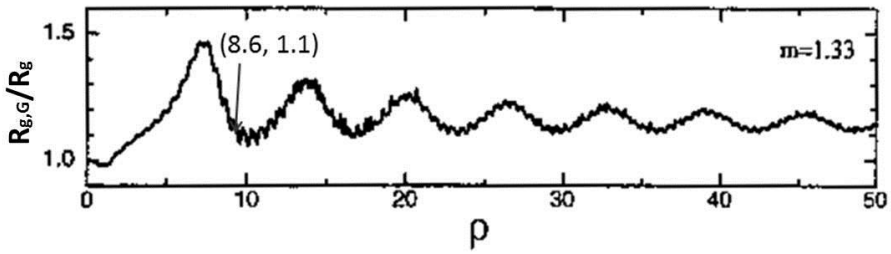

Figure 2.18 Monodisperse water droplet $R_{g,G}/R_g$ $vs.$ ρ [*Sorensen and Shi*, 2000].

When the true radius is $1.1\mu m$ ($R_g = 0.85$), $\rho = 8.6$. According to Fig. 2.18, $R_{g,G}/R_g = 1.1$, which means $R_{g,G} = 0.94\mu m$. To determine the measured radius of gyration $R_{g,meas}$, integrating the size distribution into Guinier analysis Eq. (2.24),

$$I(0)/I(q) = 1 + (q^2/3)\left(\int R_g^4 R_g^2 P(R) dR_g / \int R_g^4 P(R) dR_g\right) = 1 + (q^2/3)R_{g,meas}^2 , \quad (2.25)$$

where R_g is a variable and R_g^4 is light scattering weighting factor for forward scattering for large refractive particles [*Sorensen*, 2001]. Substitution of Eq. (2.20) with $R = R_g$, $R_0 = R_{g,G} = 0.94\mu m$, and $\sigma = 1.5$ into Eq. (2.25) and solving the integral for $R_{g,meas}^2$ yields the measured radius of gyration $R_{g,meas} = 2.5\mu m$. This is equivalent to the measured geometric radius of $R = 3.2\mu m$. Thus consistency between the Extended Guinier Analysis and the Mie fit is achieved. In summary, we started from the Mie theory which indicated the true radius is 1.1μm (radius of gyration 0.85 μm) with a geometric width 1.5. Then we apply the Extended Guinier Analysis found measured radius of gyration should be 2.5μm which agrees with the radius of gyration determined experimentally.

2.3 Dust Aerosol Generation

The goal of our research was to study irregularly shaped particles. We used a dust generator to aerosolize the irregularly shaped Arizona Road Dust and Al_2O_3 abrasive powders (Chapter 3 and 4 respectively). Figure 2.19(a) is a picture of the generator [*Hubbard*, 2006] with Fig. 2.19(b) displaying the schematic drawing. The dust generator had a 7.5cm in diameter and 7.5cm tall cylindrical chamber into which the dust was loaded. The bottom of the chamber had a stir bar connected to a motor (PITTMAN GM9413-2) connected to a DC generator to spin the stir bar at 200 revolutions per minute. Simultaneously, oxygen blew in from the bottom of the

chamber. The outgoing aerosolized dust particles were directed to the scattering volume by vinyl tubing. The dust aerosol was emitted vertically from a 3 mm inner diameter copper tube 10 mm below the scattering volume.

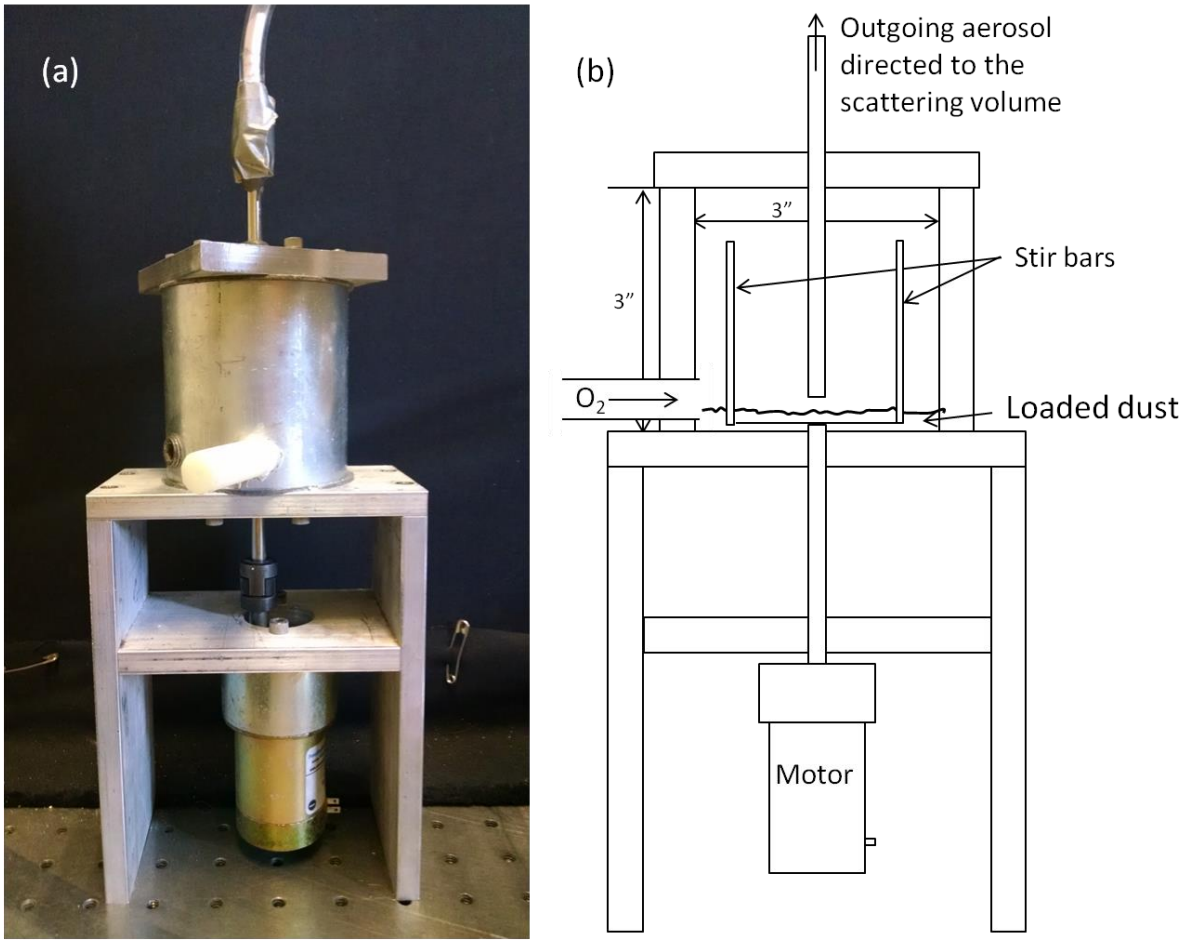

Figure 2.19 Dust aerosol generator (a) picture and (b) schematic drawing with major parts labeled.

Chapter 3 - Arizona Road Dust

Light scattering from spherical particles has been well studied and understood [*Mie*, 1908; *Hulst*, 1981; *Bohren and Huffman*, 1998]; however, Light scattering by irregularly shaped particles has not been complete understand. With the calibrated apparatus, we chose to study Arizona Road Dust (AZRD). AZRD is a standard dust used in filter testing and also a canonical example of irregularly shaped particles similar to many other dusts that can be found in the atmosphere. Curtis et al. has studied AZRD Ultrafine sample and their scattering angles were 17° to 172° [*Curtis et al.*, 2008]. They put the dust sample in HPLC grade water and aerosolized it with an atomizer. The resulting aerosol flow passed through a diffusion dryer which dries the aerosol and removes water vapor from the flow. After drying, particles were directed to the scattering volume for measurements. This process only picked up the small dust particles of the Ultrafine sized sample and left the large dust particles behind in the atomizer. We *purchased* three different sizes of AZRD (Ultrafine, Fine, and Medium) from Powder Technology Inc, Arden Hills, MN. For each measurement, a 10g sample of AZRD was loaded inside the dust generator chamber (described in Chapter 2). Our scattering angle range was 0.32° to 156°. The smallest angle of our forward scattering 0.32° was a factor of 10 smaller than the smallest angle of previous work on irregularly shaped particles [*Munoz et al.*, 2000, 2001, 2002, 2004, 2006, 2012; *Volten et al.*, 2001, 2006; *Muinonen et al.*, 2007; *Laan et al.*, 2009]. Thus we were able to detect both the Guinier regime and constant intensity forward scattering lobe which marks the end of the angular functionality in the small angle limit. This small angle detection helps determine large dust particle sizes using Guinier analysis.

3.1 Results

A constant forward scattering lobe at small q is seen followed by, at larger q, a Guinier regime, a power law regime, and an enhanced backscattering regime (Fig. 3.1). The power law regime yielded the exponents of -2.23, -2.17, and -2.12 for the Ultrafine, Fine and Medium dust samples, respectively; all with uncertainties of ± 0.05, hence nearly equivalent. This disclosure of power laws in the scattering by dusts confirms an observation made previously [*Sorensen*, 2013a].

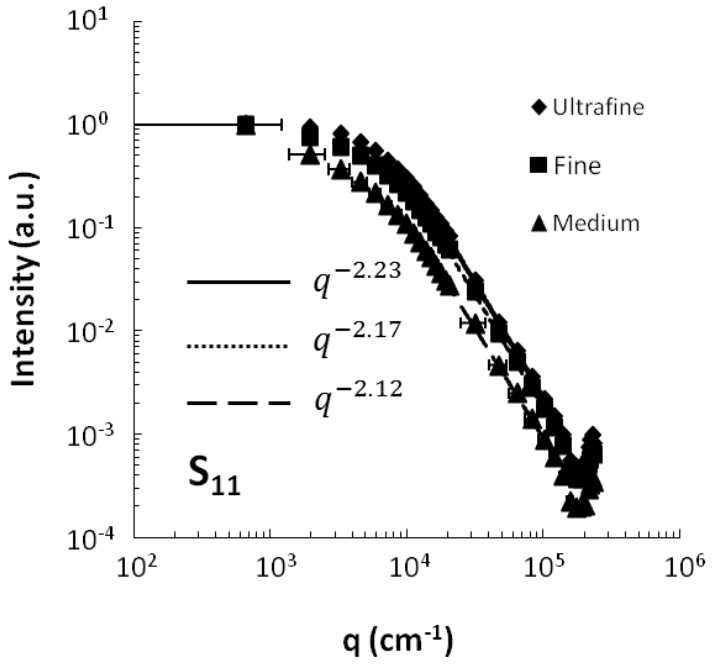

Figure 3.1 The Q-space analysis on the Ultrafine, Fine and Medium AZRD samples. S_{11} of three ARZD samples are normalized to 1 at the smallest q.

Figure 3.2 shows the six matrix elements vs. θ for the three sizes of AZRD. The forward scattering (0.32° to 9.89°) for all matrix elements except for S_{11} is enlarged in an inset in Figs. 3.2(b) to (f). In Figs. 3.2(b) and (e) for $-S_{12}/S_{11}$ and S_{34}/S_{11} respectively, the forward scattering fluctuated around 0 without any functionality with considerable variation. This variation was due

to the value of two nearly equal intensities subtracted from each other divided by the value of those two nearly equal intensities added up to each other. Ideally, the forward scattering of -S12/S11 and S34/S11 would align to 0, which is consistent with the data with consideration of errors.

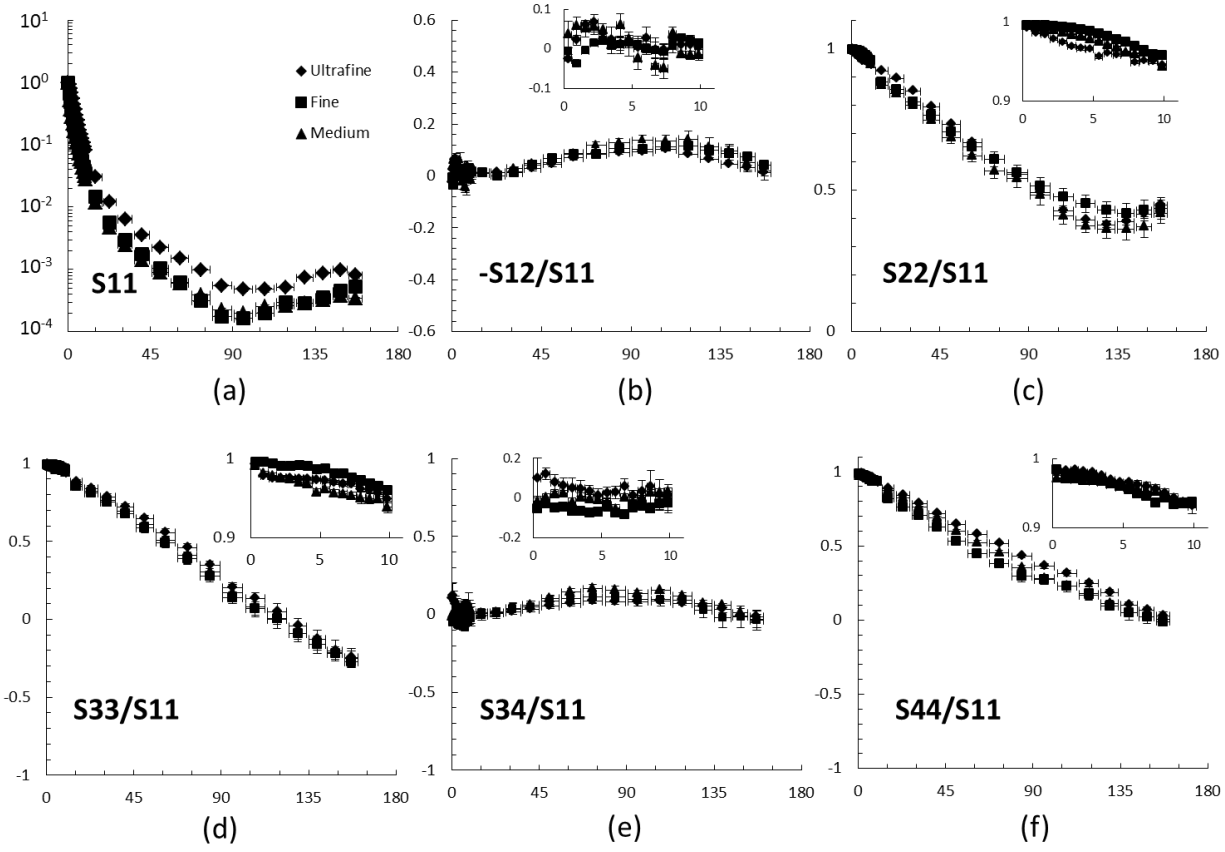

Figure 3.2 The scattering matrix elements vs. θ for three sizes of AZRD. S_{11} of three ARZD samples are normalized at the smallest angle.

3.2 Discussion

The scattering matrix elements of AZRD, which has irregular shapes, behaved differently from the scattering matrix elements of the water droplets – "quasi-spherical" particles (Fig. 2.15). For non-spherical particles, S_{22}/S_{11} was no longer unity for all scattering angles larger than

0°. The six matrix elements of AZRD agreed very well with the summary of the work done by the Granada-Amsterdam group (Fig. 3.3), on many different types of irregular shaped particles [*Volten et al.*, 2001], such as feldspar, red clay, quartz, Sahara dust, volcanic ash, etc.

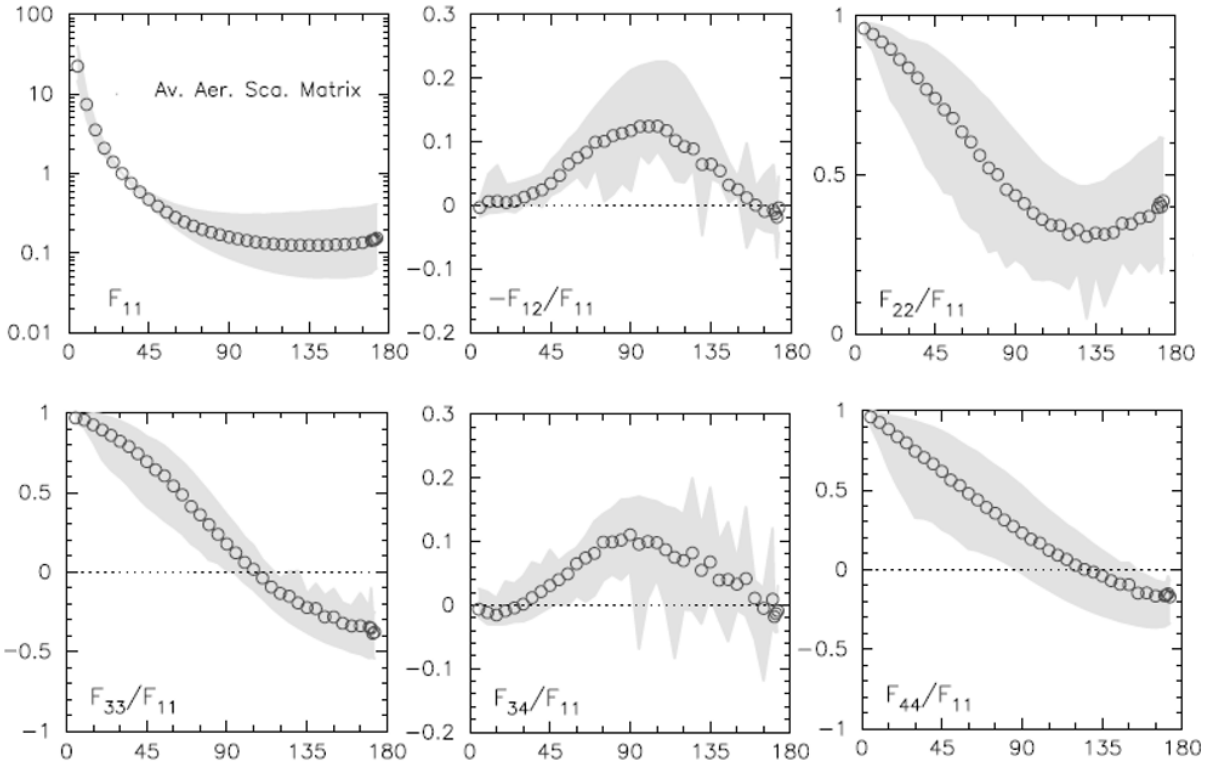

Figure 3.3 The summary of the work done by the Amsterdam group on many different types of irregular shaped particles [*Volten et al.*, 2001]. Our AZRD data would fall right on top of this figure.

The Guinier regimes of the S_{11} plots occur at smaller q for dusts with increasing sizes as indicated by the supplier (Fig. 3.2). This was as expected because $qR_g = 1$. Figure 3.4 shows Guinier analysis, I(0)/I(q) versus q^2, for the three sizes of AZRD.

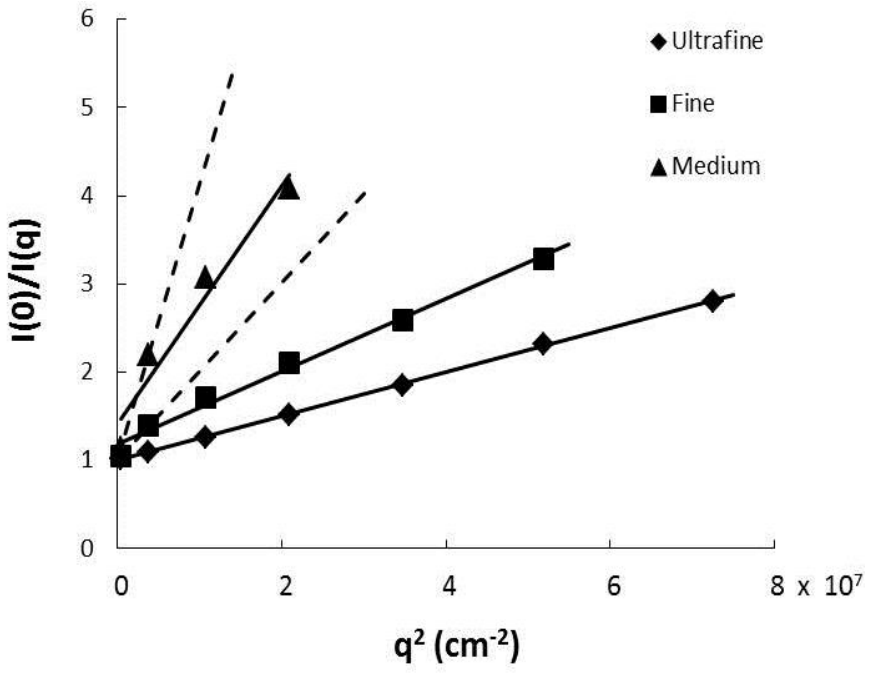

Figure 3.4 Guinier analysis of AZRD, Ultrafine, Fine and Medium.

The Ultrafine dust has several points of data for use in the Guinier analysis. From the slope the radius of gyration of Ultrafine dust was 2.7μm. For Fine dust and Medium dust, the data are more limited. We put two boundary slopes for each set of data. The fitted lines (solid lines) with the smaller slope were the fits for the all the points in a set and the fitted lines (dashed lines) with the greater slope only include data when $qR_g < 1$, where the Guinier analysis is, in principle, applicable. According to the fitted line slopes, the radius of gyration ranged between 3.5 and 5.5μm for Fine dust and between 6.4 and 9.7μm for Medium dust. Although the fits for Fine and Medium dust in the $qR_g < 1$ range only include two points, the estimated sizes were close to the sizes the manufacturer claimed. According to Powder Technology Inc., the median size of Ultrafine dust particles was 4.5μm diameter, the median size of Fine dust particles was 10μm diameter, and the median size of Medium dust particles was 15μm diameter, which means the sizes determined from Guinier analysis were in the reasonable range. Note that we did not

apply the Extended Guinier analysis because we could not determine a describable functionality of the size distribution for AZRD.

Figure 3.5 shows the images with 10μm scaling bars for three AZRD samples under a binocular compound optical microscope. The measured radii of gyration of Ultrafine, Fine, and Medium AZRD were 2.7μm, 5.5μm, and 9.7μm respectively, which agreed visually well with the images according to the scaling bars.

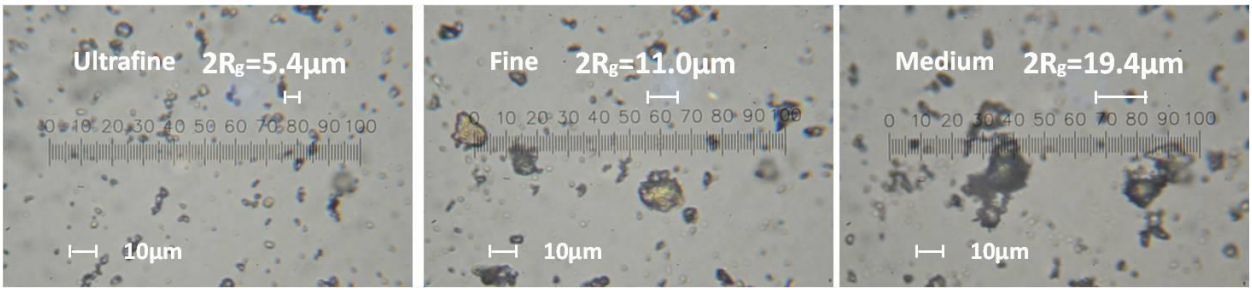

Figure 3.5 The images for three AZRD samples under an optical compound microscope. Each figure has a 10 micron scale bar in the lower left and a scale bar equal to the light scattering determined $2R_g$ in the upper right for comparison to the images. Note that light scattering is strongly affected by the largest particles in an ensemble.

The Q-space analysis unveiled a characteristic description of scattering common to spheres and dusts: a q-independent forward scattering lobe at smallest q, followed by a Guinier regime, a power law regime and an enhanced backscattering regime. For AZRD the exponents in the power law regime discriminated spheres from these particular dusts. Figure 3.6 shows the comparison of the Q-space analysis between (a) water droplets from Fig. 2.14 and (b) AZRD from Fig. 3.1. Unlike scattering from our "quasi-spherical" water droplets shows the power law regime with exponents of -2 and -4. Scattering from three AZRD samples all show single power laws with exponents other than -4.

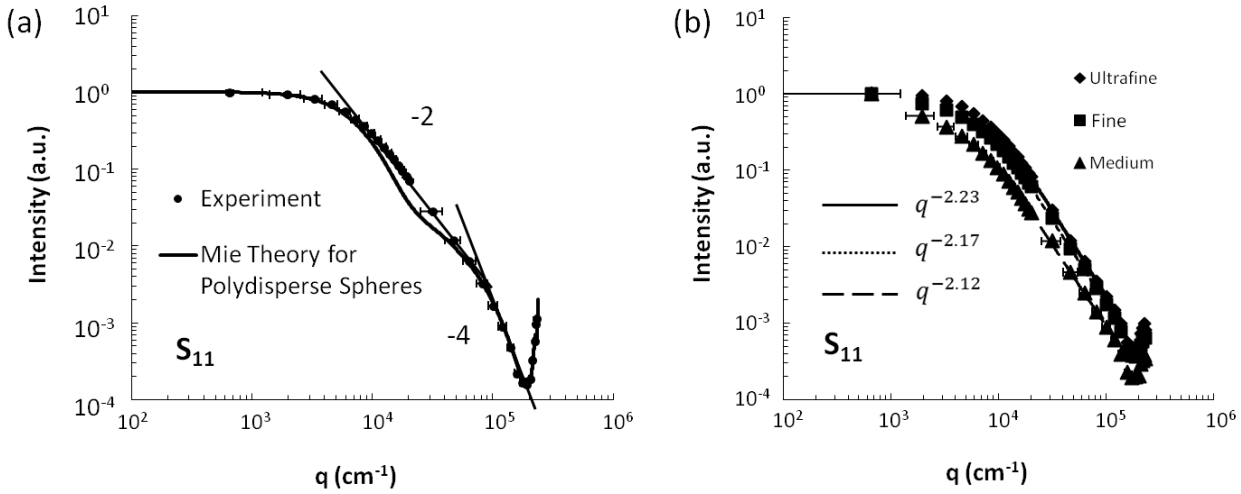

Figure 3.6 The comparison of the Q-space analysis between (a) water droplets and (b) AZRD. Unlike scattering from our "quasi-spherical" water droplets shows the power law regime with exponents of -2 and -4. Scattering from three AZRD samples all show single power laws with exponents other than -4.

3.3 Summary

The scattering matrix elements for irregularly shaped particles behaved differently from spherical particles. Regardless of particle shape, Guinier analysis indicated particles sizes. Q-space analysis unveiled a characteristic description of scattering common to spheres and dusts: a q-independent forward scattering lobe followed by a Guinier regime, a power law regime and an enhanced backscattering regime. Unlike Mie scattering from our "quasi-spherical" water droplets showed the power law regime with exponents of -2 and -4. The exponents of the power laws of the Q-space analysis on the Ultrafine, Fine and Medium AZRD samples were -2.23, -2.17, and -2.12, respectively, nearly equivalent within experimental errors. The measured radii of gyration of Ultrafine, Fine, and Medium AZRD were 2.7μm, 5.5μm, and 9.7μm respectively, which agreed visually well with the images according to the scaling bars. The absolute value of power law exponents decreased with increasing size (hence with increasing phase shift parameter ρ')

was repeatable from multiple measurements, although the power law exponents were nearly equivalent within experimental errors. Therefore, to measure particles that we could systematically change sizes.

Chapter 4 - Al_2O_3 Abrasives

The content of this chapter is based on a manuscript under review [*Heinson et al.*, n.d.]. Much work including both experiment and theory has been conducted to study irregularly shaped particles [*Muinonen*, 1998; *Muinonen and Lagerros*, 1998; *Munoz et al.*, 2000, 2001, 2002, 2004, 2006, 2007, 2012; *Volten et al.*, 2001, 2006; *Kalashnikova and Sokolik*, 2004; *Dubovik et al.*, 2006; *Laan et al.*, 2009; *Muñoz et al.*, 2010; *Nousiainen et al.*, 2011a, 2011b]. However, surprisingly few studies have changed relevant parameters in a systematic way which could lead to the uncovering of light scattering patterns. From Chapter 3, we noticed that the power law exponents decreased with increasing size for AZRD. We chose to study abrasive particles because they have irregular shapes, were readily available, and can be obtained in a range of sizes as specified by the manufacturer. For AZRD, there were only three different sizes we could use; for abrasives, we had more size options. Because the abrasive action requires rolling between the two surfaces that are grinding, they have a roughly spherical overall shape, as opposed to particles with large aspect ratios such as flakes or needles. Thus we anticipate that scattering by abrasive particles might have some characteristics in common with scattering by spheres. We directly compared the scattering by the abrasives and spheres by Q-space analysis. Moreover, the comparison described forward and backward scattering properties and the possible power law that might lie in between.

4.1 Results

We measured the phase function of six different grits of white Al_2O_3 abrasive powders from Panadyne Abrasives (Montgomeryville, PA). For each measurement, 10g of grit sample

were loaded inside the dust generator chamber. Al_2O_3 is birefringent but the two refractive indices (1.760 and 1.768) are very close to each other. Therefore we treated the refractive index as 1.76. The grit numbers and the average diameters sizes of the abrasives were 1200 grit (3μm), 1000 grit (4.5μm), 800 grit (6.5μm), 600 grit (9.3μm), 400 grit (17.3μm), and 320 grit (29.2μm) as given by the manufacturer. Note that the larger the grit number, the finer the powder.

We performed Q-space analysis on the angular scattering by the Al_2O_3 abrasives as shown in Figs. 4.1 to 4.6. The figures also contain corresponding optical microscope images. Each image has a 10 micron scale bar in the lower left and a scale bar in the upper right indicating the diameter given by the manufacturer for comparison to the image. The scattered intensity with arbitrary unit (a.u.) is plotted vs. $q\ (cm^{-1})$ on a double logarithmic plot. For the three smaller sizes, grits 1200, 1000, and 800, Q-space analysis revealed an indication of a constant forward scattering lobe at smallest q followed by, with increasing q, a Guinier regime, a power law regime, and an enhanced backscattering regime. The power law exponents are labeled in each graph. For the three larger sizes, grits 600, 400 and 320, the forward scattering and Guinier regimes could not be seen since the large size requires detection angles smaller than our minimum angle of 0.32°. Also, for the larger grits, a new feature appeared starting perhaps with 800 grit and then growing with increasing size: a kink near $q \simeq 2 \times 10^4 cm^{-1}$. This kink perturbs the power law functionality.

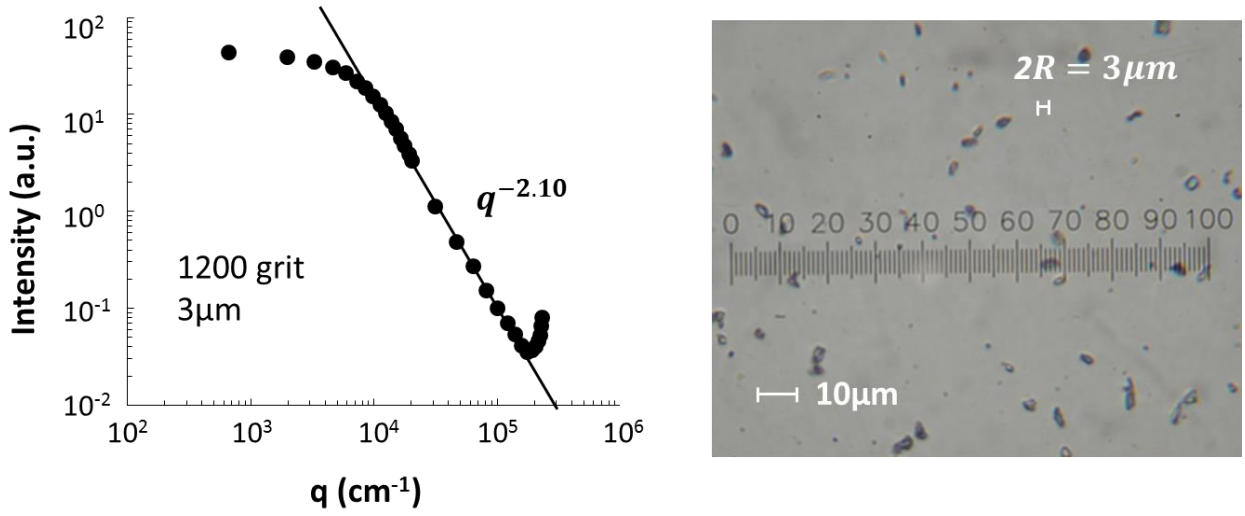

Figure 4.1 Q-space analysis of scattering by 1200 grit Al_2O_3 abrasives and the corresponding image under an optical compound microscope.

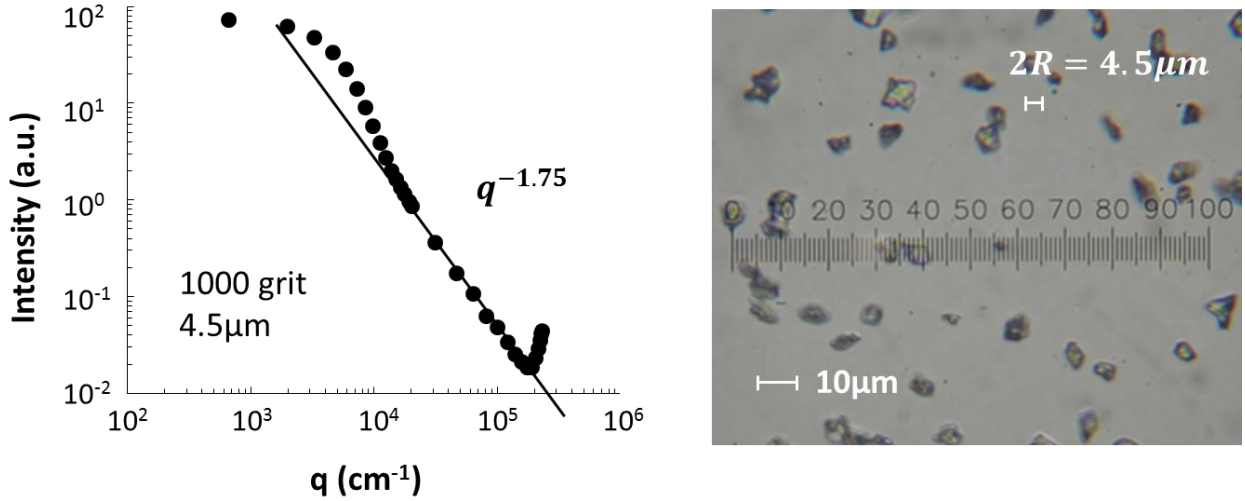

Figure 4.2 Q-space analysis of scattering by 1000 grit Al_2O_3 abrasives and the corresponding image under an optical compound microscope.

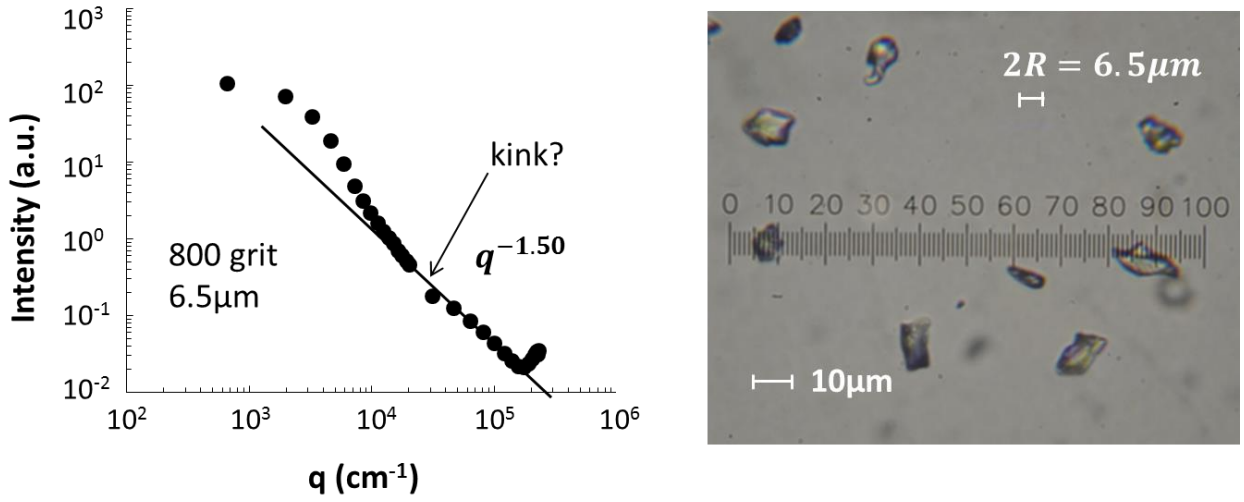

Figure 4.3 Q-space analysis of scattering by 800 grit Al_2O_3 abrasives and the corresponding image under an optical compound microscope.

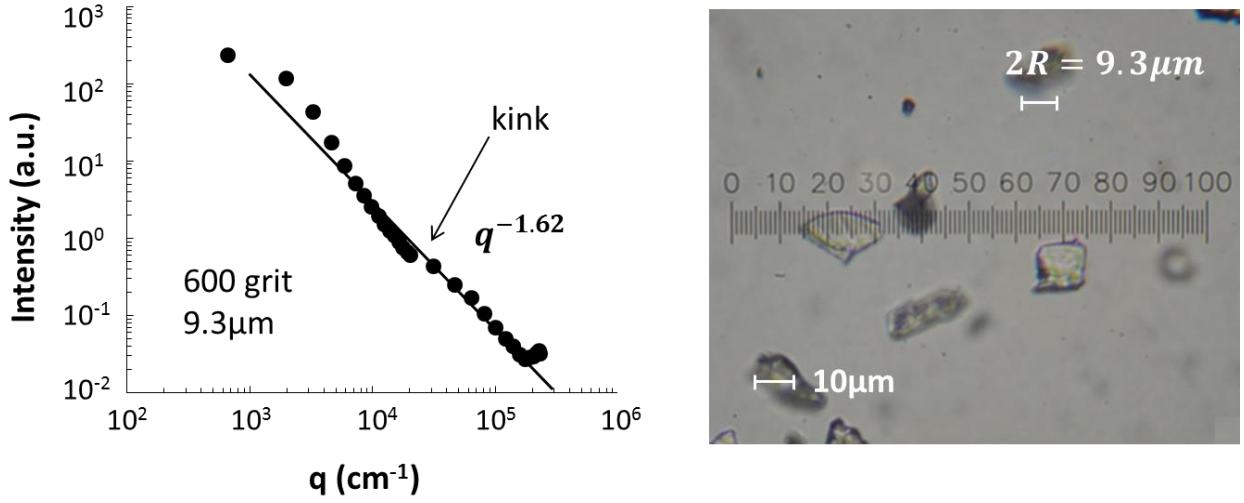

Figure 4.4 Q-space analysis of scattering by 600 grit Al_2O_3 abrasives and the corresponding image under an optical compound microscope.

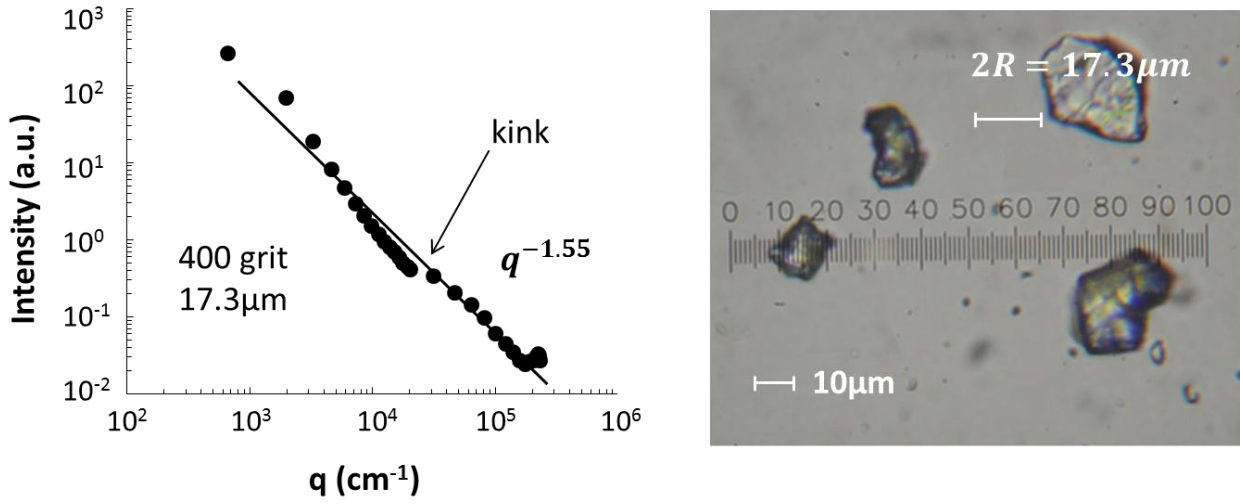

Figure 4.5 Q-space analysis of scattering by 400 grit Al_2O_3 abrasives and the corresponding image under an optical compound microscope.

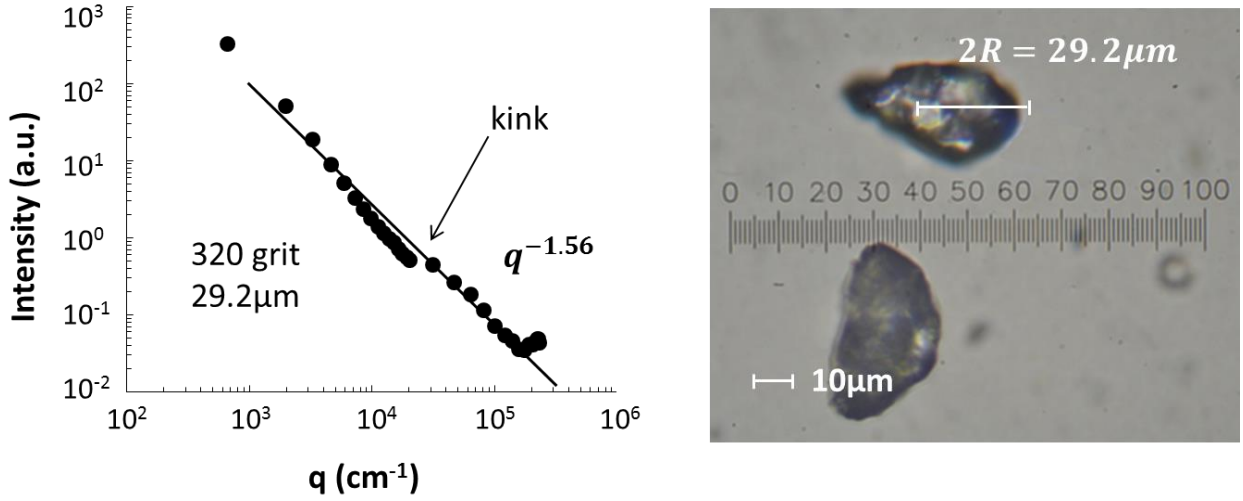

Figure 4.6 Q-space analysis of scattering by 320 grit Al_2O_3 abrasives and the corresponding image under an optical compound microscope.

We have verified that the kink was not due to the misalignment or malfunction of our setup by calibrating the forward and side detectors to each other. This was substantiated by the fact that the kink did not exist for small abrasives and developed with increasing sizes. There

were no kinks for water droplets or AZRD. Thus we are confident that the kink was an experimental fact.

4.2 Discussion

4.2.1 Sizes

As stated above, the size labeled in each figure is the average size of each abrasive sample given by the manufacturer. However, light scattering tend to see the big particles of an ensemble of particles because larger particles scatter more light. Hence, we need to determine the sizes from light scattering. Since the abrasives have irregular shapes, it was hard to define the sizes. We used Guinier analysis of light scattering to determine the radius of gyration R_g for each of grits 1200, 1000, and 800 which had strong Guinier regimes. In the limit the phase shift parameter $\rho' \to 0$ and when $qR_g < 1$, the Guinier equation [*Guinier et al.*, 1955] describes the forward scattering as Eq. (2.18). When $\rho' > 1$, the Guinier equation still holds but the radius of gyration inferred from Eq. (2.18) was not the true radius of gyration [*Sorensen and Shi*, 2000]. For spheres when $\rho' > 30$, the ratio of the true to measured radii of gyrations is about 0.85 (± 10%) as shown in Fig. 2.18. Since a study similar to [*Sorensen and Shi*, 2000] has not been performed for non-spherical particles, and since the abrasive powders had a roughly spherical shape, we applied this correction to the R_g we determine from a Guinier analysis of our abrasive light scattering.

The Guinier analysis [*Guinier et al.*, 1955] to determine the light scattering radius of gyration is shown in Fig. 4.7. Note the paucity of data in the Guinier regime would not provide great accuracy. We could only apply Guinier analysis to the 1200, 1000 and 800 grits which have

relatively small sizes to ensure $qR_g < 1$. From Guinier analysis, the measured radii of gyration of the 1200, 1000, and 800 grits were 2.4μm, 3.7μm, and 6.4μm, respectively. After the factor of 0.85 correction, the true radii of gyration were 2.0μm, 3.2μm, and 5.4μm, respectively.

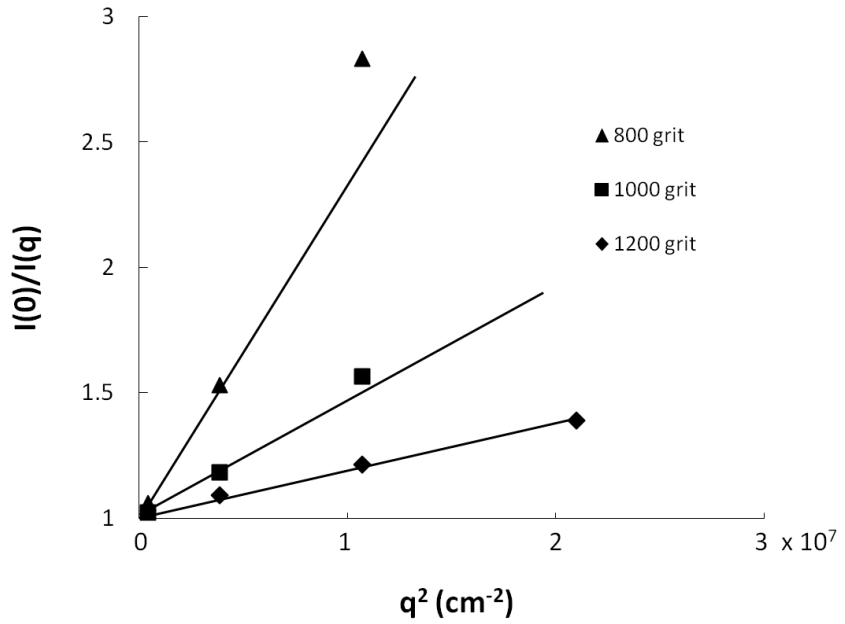

Figure 4.7 Guinier analysis on Al_2O_3 abrasives of 1200, 1000, and 800 grit. The slopes indicated the measured radii of gyration of 2.4μm, 3.7μm, and 6.4μm, respectively.

Mathematically, R_g is the root mean square radius which is smaller than the visible perimeter. The exact relation between R_g and the visible perimeter depends on the particle shape. Since we do not know the exact shape, we make an approximation based on spheres where $R_g = \sqrt{3/5}\,R$. Therefore, the optical perimeter radii of the 1200, 1000, and 800 grits were 2.6μm, 4.2μm, and 7.0μm, respectively. Hence the diameters were 5.2μm, 8.8μm, and 14μm, respectively. Compare to the diameters given by the manufacturer, 3μm, 4.5μm, and 6.5, we concluded that the light scattering measured sizes of the three grits were approximately twice as big as the sizes given by the manufacturer. We assumed that was true for all the other three

abrasive grits. Hence to calculate ρ's for the abrasives, we used the sizes twice the size given by the manufacturer.

4.2.2 Comparison between spheres and Al_2O_3 abrasives

In this section we make a comparison between the scattering from the irregularly shaped abrasives and perfect spheres with a polydisperse size distribution, using Q-space analysis. The comparison is semi-quantitative, but we believe it has value and points the way for future research. We compared grits and spheres of the same size and refractive index, hence with the same ρ'. Only the three smallest grits had well defined forward scattering and Guinier regimes to match to the same regimes for the spherical particles. To achieve the match we generated Mie solutions using Philip Laven MiePlot [*Laven*, 2004] to find a sphere radius that fit best to the abrasives Guinier regime for each grit. This was done under the condition of spherical particles with a log-normal size distribution width of 1.2, which was used to eliminate the Mie scattering ripples.

Figure 4.8 (a) – (c) show the comparisons between the spheres shown as dashed lines and the abrasives data shown as solid circles, where the scattered intensity (normalized to 1 at $qR \ll 1$) is plotted vs. qR. In Fig. 4.8 the abrasives scattering and the Mie scattering were forced to fit to each other in the Guinier regime so that we could see how they compared at large qR.

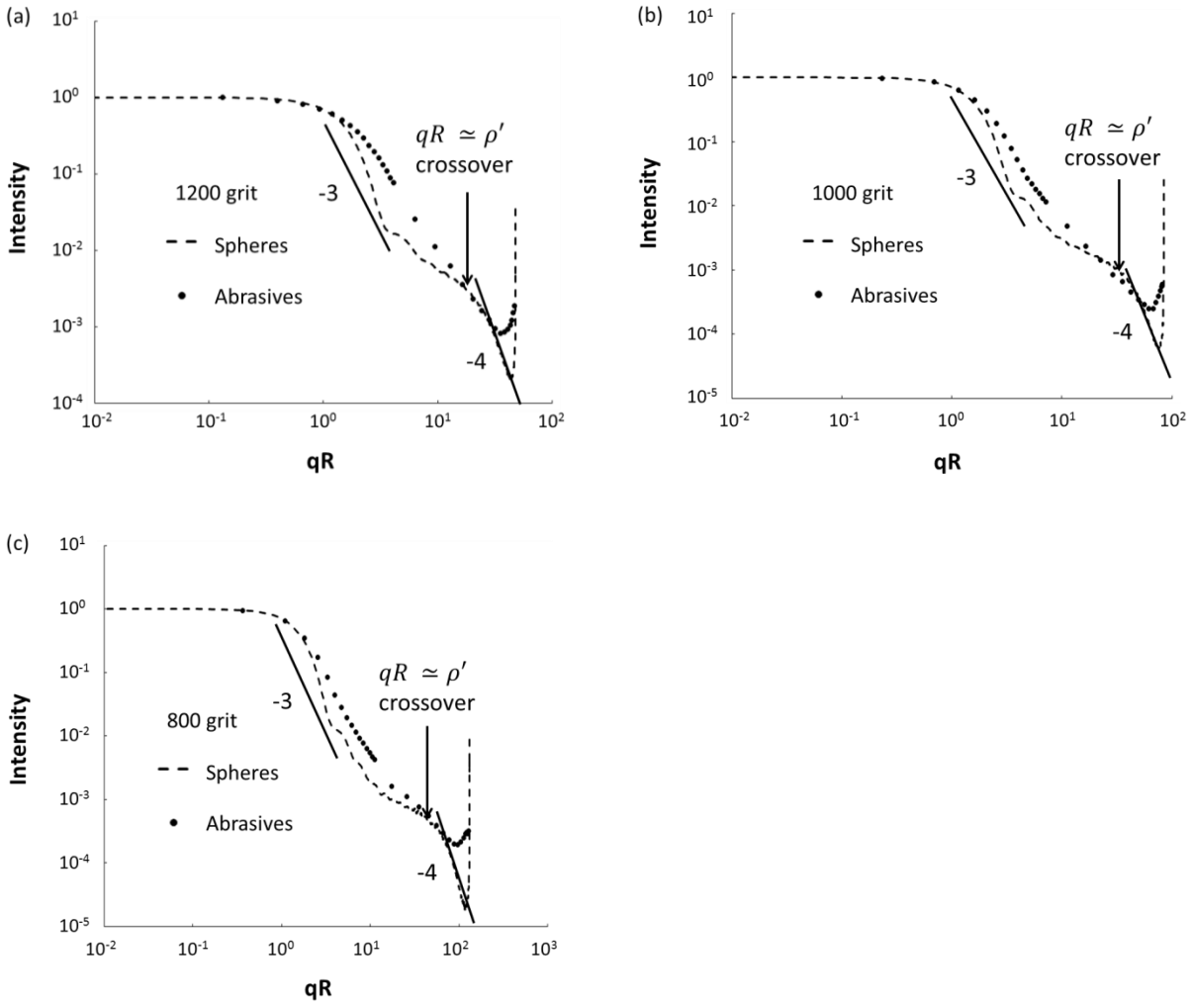

Figure 4.8 Comparisons between scattering by spheres and the 1200, 1000, and 800 grit abrasives. The scattered intensity (normalized at $qR \ll 1$) is plotted vs. qR for each grit. Spheres and abrasives were forced to fit in the Guinier, $qR \ll 1$, range. Also indicated are the $qR \simeq \rho'$ crossover points for the sphere scattering.

The Q-space functionalities for spheres is as follows [*Heinson et al.*, 2015]: when $\rho' < 1$ (the RDG limit) a $(qR)^{-4}$ functionality follows the Guinier regime. With increasing ρ', a $(qR)^{-2}$ functionality appears after Guinier regime and then this falls back to a $(qR)^{-4}$ functionality when $qR \gtrsim \rho'$. As ρ' becomes larger, the $(qR)^{-2}$ functionality breaks into a $(qR)^{-3}$ regime followed by a relatively flat regime which then crosses over to a $(qR)^{-4}$

functionality when $qR \gtrsim \rho'$. We call this the "$qR \simeq \rho'$ crossover". These functionalities are apparent in Fig. 4.8 for spheres.

The comparison of the abrasive scattering to the spherical particle scattering in Fig. 4.8 uncovers some interesting features. At the $qR \simeq \rho'$ crossover, the scattering of the abrasives roughly touches the scattering due to the spheres. The end points of the scattering, i.e. the scattering at the maximum $qR = 2kR$, by the irregularly shaped abrasives were close to the geometric centers of the glories of the spheres. Along with these features, the rough $(qR)^{-3}$ immediately after the Guinier regime and the $(qR)^{-4}$ functionality for $qR \gtrsim \rho'$ are lost. One could say that the "roughening" of the spherical shape into that of the abrasives smoothed the intensity versus qR plot to leave a Guinier hump plus a single power law that was anchored by the Guinier regime and the $qR \simeq \rho'$ crossover. The same comparison was made in [*Maughan et al.*, 2016] between Gaussian Random Spheres (GRSs) and spheres to find the same result for the ending points, especially for large ρ'. Unfortunately, we could not directly compare GRSs and our abrasives because the smallest ρ' for our Al_2O_3 abrasives was larger than any GRSs that we can currently solve for using computational techniques.

Because the Guinier regime was not in the detectable range for the other three abrasives, 600, 400, and 320 grits, we could not make direct comparisons to spheres. For spheres, the $(qR)^{-3}$ regime is a consequence of the crossover of the three dimensional spherical particle scattering to two-dimensional, Fraunhofer diffraction [*Hecht*, 2002] which must occur when the sphere becomes very large and refractive. We expect a similar 3d to 2d crossover would occur for any shape at large enough ρ'. However, the regime before the kink for the abrasives does not show a $(qR)^{-3}$ functionality. The kink that occurs in the scattering for these three grits developed with increasing size, thus increasing ρ'. Note that these three grits were in a regime of

large ρ' that has not been sufficiently explored in previous work [*Munoz et al.*, 2000, 2001, 2002, 2004, 2006, 2007; *Volten et al.*, 2001, 2006; *Curtis et al.*, 2008; *Laan et al.*, 2009; *Sorensen et al.*, 2014; *Wang et al.*, 2015; *Maughan et al.*, 2016]. Obviously this large ρ' region needs further study. If large ρ' was not the cause of the kink, we speculate that it could be due to the higher degree of symmetry for the abrasives than for all the particles studied previously.

4.3 Summary

We measured the scattered light intensity for six different sizes of Al_2O_3 grits over a wide range of scattering angles starting at 0.32°. Similar to AZRD, Q-space analysis of the Al_2O_3 abrasives revealed a forward scattering regime at small q, followed by a crossover, Guinier regime, a power law regime with quantifiable exponents, and an enhanced backscattering regime. We directly compared the scattering of 1200, 1000, and 800 grit abrasives with corresponding spheres by finding the best fit in Guinier regime. At large qR, the scattering of the abrasives approximately coincides with that of the spheres at the $qR \simeq \rho'$ crossover point of the scattering from spheres, and the abrasive scattering follows a power law after the Guinier regime whereas the spherical particle scattering is much more complex. The scattering at the maximum $qR = 2kR$ by the irregularly shaped abrasives was close to the geometric centers of the glories of the spheres. The largest three abrasives, for which $\rho' \gtrsim 100$, showed a kink in the power law, which needs further study.

Chapter 5 - The Exponent of Q-Space Analysis as a Function of ρ'

The content of this Chapter is based on [*Heinson et al.*, 2016] . In this chapter, we will apply Q-space analysis to the angular distribution of scattered light for a wide range of non-fractal irregularly shaped particles using both experimental and theoretical data produced by our group and others. The experimental data include 43 aerosol data sets from the Amsterdam-Granada group [*Munoz et al.*, 2000, 2001, 2002, 2004, 2006, 2007, 2012; *Volten et al.*, 2001, 2006; *Laan et al.*, 2009]. The Amsterdam-Granada group measured six scattering matrix elements (S_{11}, S_{12}/S_{11}, S_{22}/S_{11}, S_{33}/S_{11}, $S_{34}/S_{11,}$ S_{44}/S_{11}) as a function of angle for all the aerosols they studied. We only picked up S_{11} vs. θ, the phase function. The experimental data also include our work on Ultrafine, Fine, and Medium Arizona Road Dust (AZRD) samples [*Wang et al.*, 2015] , and the data on Ultrafine AZRD from Curtis et al. [*Curtis et al.*, 2008], and our work on six Al_2O_3 abrasives grits [*Heinson et al.*, n.d.]. The theoretical data include Gaussian Random Spheres and thickened percolation clusters from our group and irregular spheres from a collaboration between our group and Zubko [*Sorensen et al.*, 2014]. We will show an undeniable trend in the absolute value of the exponents with respect to the internal coupling parameter ρ'.

5.1 Q-Space analysis of a collection of irregularly shaped particles

5.1.1 Analysis of prior published data sets

The Amsterdam-Granada group has measured light scattering from various kinds of irregularly shaped aerosol particles such as feldspar, red clay, quartz, volcanic ash and many others at wavelengths 441.6nm and 632.8nm [*Munoz et al.*, 2000, 2001, 2002, 2004, 2006, 2007, 2012; *Volten et al.*, 2001, 2006; *Laan et al.*, 2009]. Their volcanic ash was collected from

different locations, years and time after possible eruptions. We applied Q-space analysis to all 43 aerosol data sets available on their website as shown in Fig. 5.1(a) – (i) where the scattered intensity with arbitrary units is plotted vs. q (cm^{-1}). A different, arbitrary multiplication factor is applied to the intensity for each aerosol simply for clarity in the figures. Q-space analysis with its double logarithmic axes reveals the data have a linear relationship in this space, with the fitted power law exponent values, with uncertainty of ± 0.05, labeled on the right side of each curve.

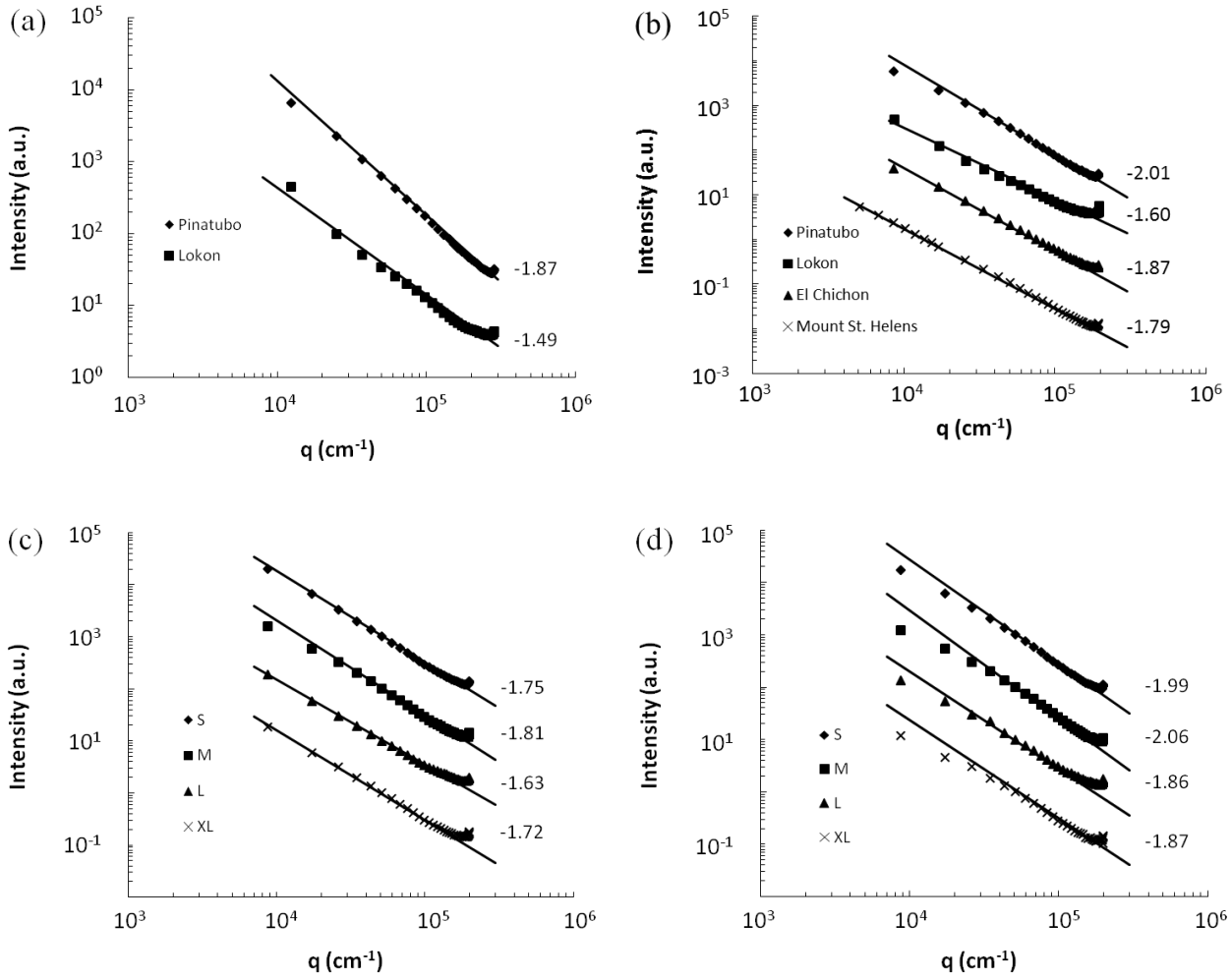

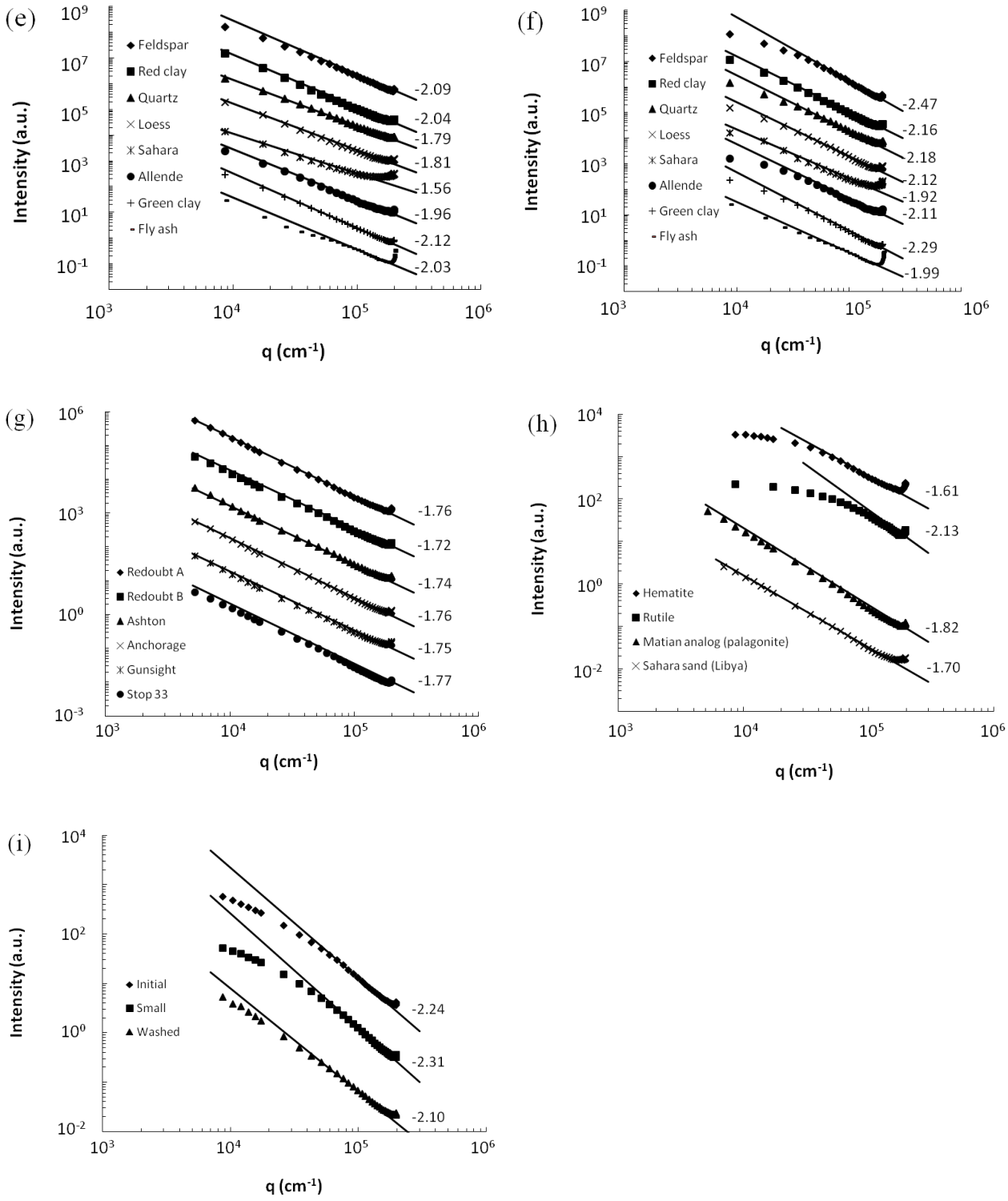

Figure 5.1 Scattered intensities (a.u.) (intensities have been scaled for clarity) expressed as functions of the parameter q (cm^{-1}), for studies of the indicated particle types, as reported by the Amsterdam-Granada group (Munoz et al. 2000; Munoz et al. 2001; Munoz et al. 2002; Munoz et al. 2004; Munoz et al. 2006; Munoz et al. 2007; Munoz et al. 2012; Volten et al. 2001; Volten et al. 2006; Laan et al. 2009). Lines are the power law fits proposed in this

work, and the numbers to the right of the plots are the exponents of the power law. (a) Volcanic ash (Pinatubo, Lokon) measured at $\lambda = 441.6nm$. (b) Volcanic ash (Pinatubo, Lokon, El Chichol, Mnt St. Helens) measured at $\lambda = 632.8nm$. (c) Olivine S, Olivine M, Olivine L, Olivine XL measured at $\lambda = 441.6nm$. (d) Olivine S, Olivine M, Olivine L, Olivine XL measured at $\lambda = 632.8nm$. (e) Feldspar, Red clay, Quartz, Loess, Sahara, Allende, Green clay, Fly ash measured at $\lambda = 441.6nm$. (f) Feldspar, Redy clay, Quartz, Loess, Sahara, Allende, Green clay, Fly ash measure at $\lambda = 632.8nm$. (g) Volcanic ash (Redoubt A, Redoubt B, Spurr Ashton, Spurr Anchorage, Spurr Gunsight, Spurr Stop 33) measured at $\lambda = 632.8nm$. (h) Hematite, Rutile, Martian analog (palagonite), Sahara sand (Libya) measured at $\lambda = 632.8nm$. (i) Forsterie initial, Forsterie small, Forsterie washed measured at $\lambda = 632.8nm$.

It is important to again stress that, in contrast to the behavior in q-space, plotting the data with a linear abscissa representing the scattering angle θ yields nondescript, indistinguishable curves. Figure 5.2 [*Sorensen*, 2013a] is an example of this comparison between conventional analysis and Q-space analysis on desert dust.

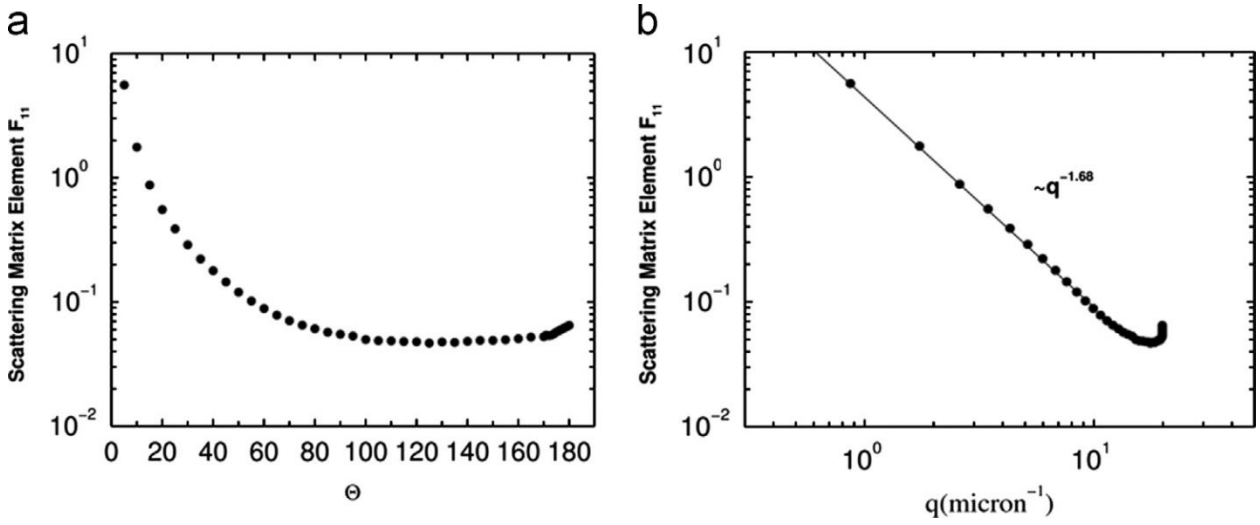

Figure 5.2 Comparison between conventional analysis and Q-space analysis on desert dust [*Sorensen*, 2013a]. The same data are plotted on each side of the figure. Plotting the data vs. linear θ (left) yields a non-descript curve; plotting vs. logarithmic q (right) yields an obvious straight line regime indicating a power law.

The data in Fig. 5.1 are limited in that they do not show a constant forward scattering lobe and only some of them show a portion of a Guinier regime. This limitation is due to minimum scattering angles larger than either 3° or 5°. Consequently, neither the true forward scattering regime nor the Guinier regime are captured in the scattering data for sizes greater than $R \approx \lambda/2\theta$ (derived from the Guinier regime $q \simeq R^{-1}$, and Fraunhofer diffraction, see e.g. Hecht, 2002) which is ca. 5 microns for 3°.

The exponents for the power law regime are obtained by fitting the data after the Guinier regime and before the Glory. For example, scattering by volcanic ash from the Pinatubo volcano measured at $\lambda = 441.6nm$ obeys the power law with the exponent of -1.87 found from a fit to the data excluding the first few points and the Glory points. The Amsterdam-Granada group provided the effective radius and the refractive index for each kind of aerosol particle, which allows us to calculate the internal coupling parameter ρ'. We noticed that the exponents evolve with increasing ρ'.

5.1.2 Arizona Road Dust (AZRD)

We discussed the measurements on three AZRD samples [*Wang et al.*, 2015] in Chapter 3. Q-space analysis on AZRD showed power laws with quantifiable exponents of -2.23, -2.17, and -2.12 for the Ultrafine, Fine and Medium dust samples, respectively; all with uncertainties of ±0.05. The sizes of the three AZRD samples determined by Guinier analysis were 2.7μm, 5.5μm, and 9.7μm for the Ultrafine, Fine, and Medium dust samples, respectively. These sizes along with the refractive index of 1.54 [*Gorner et al.*, 1995; *Wang et al.*, 2009] were used to calculate ρ'. Hence, ρ' increases from Ultrafine to Medium AZRD, which indicates the exponents

decrease with increasing ρ's. Curtis et al. (2008) conducted experiments on one AZRD sample [*Curtis et al.*, 2008]. They used an experimental method which produced much smaller Ultrafine AZRD particles with the projected surface area weighted effective radius 0.318μm. This radius implies a Guinier regime near $q \approx 3 \times 10^4 cm^{-1}$. We extrapolated their experimental data and did Q-space analysis and find a power law with the exponent of -2.60 as shown in Fig. 5.3.

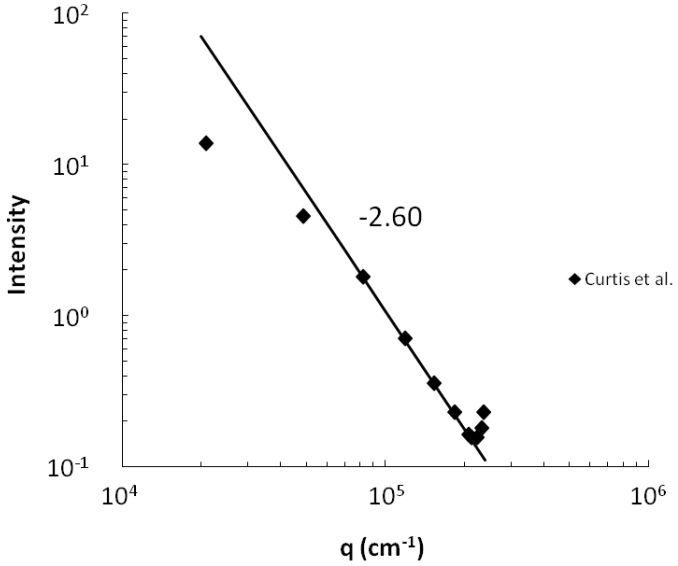

Figure 5.3 Q-space analysis on extrapolated AZRD data from Curtis et al. [*Curtis et al.*, 2008].

5.1.3 Al_2O_3 Abrasives

We discussed the measurements on six Al_2O_3 Abrasives grits in Chapter 4. Q-space analysis showed power laws with quantifiable exponents of -2.10, -1.75, -1.50, -1.62, -1.55, and -1.56 for grit 1200, 1000, 800, 600, 400, and 320 respectively. The sizes of the abrasives determined by Guinier analysis are twice as big as the ones claimed by the manufacturer and refractive index is 1.76, with which we could determine the ρ's.

5.1.4 Gaussian Random Spheres (GRSs)

The data in this section were provided by Justin Maughan who has studied Gaussian Random Spheres (GRSs) [*Maughan et al.*, 2016]. GRSs have been used to model many different objects from asteroids to dust and ice particles [*Muinonen*, 1998; *Muinonen and Lagerros*, 1998; *Munoz et al.*, 2007; *Nousiainen et al.*, 2011a, 2011b]. Figure 5.4 shows a GRS model compared to Saharan dust (Libya) particles from [*Munoz et al.*, 2007].

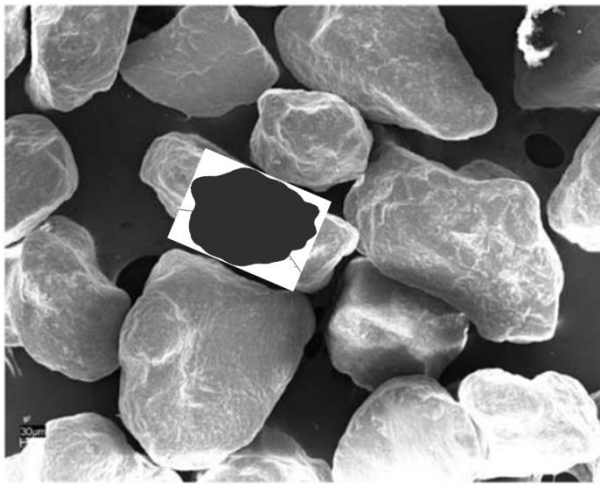

Figure 5.4 GRS model compared to Saharan dust particles from [*Munoz et al.*, 2007].

GRS, as shown in Fig. 5.5 [*Maughan et al.*, 2016], is described by three parameters: 1) a, the mean radius, which sets the overall size of the particle; 2) σ, the relative standard deviation in the radial direction which is used as a measure of the size of fluctuations in radial directions away from the mean radius a. The standard deviation would be calculated by taking the square root of the sum of the square of the difference of the actual radii from the mean radius. The relative standard deviation is the standard deviation normalized by the mean radius; and 3) ν, the power law exponent that controls the angular range of fluctuations in a tangential direction. For general descriptions of GRSs the reader is directed to [*Veihelmann et al.*, 2006; *Muinonen et al.*,

2007; *Nousiainen et al.*, 2011a], and for a more in-depth mathematical treatment [*Lamberg et al.*, 2001].

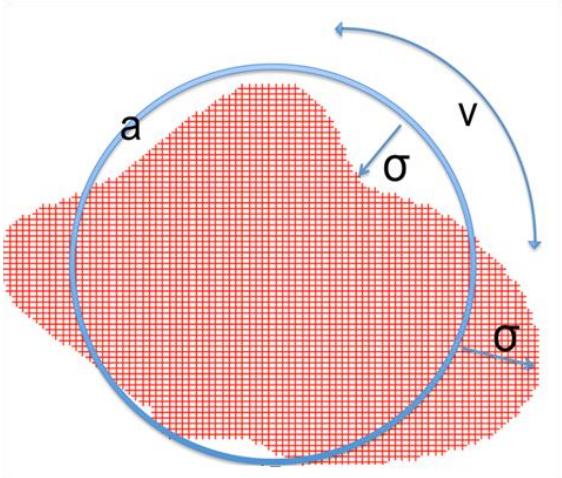

Figure 5.5 GRS described by three parameters [*Maughan et al.*, 2016]. The parameter a is the mean radius. The parameter σ is the relative standard deviation in the radial direction. The parameter ν is the power law exponent controlling the angular range of fluctuations in a tangential direction.

[*Maughan et al.*, 2016] studied GRSs with σ = 0.2 and ν =0.3 and size parameters ranging from $ka = 10$ to 30, with refractive index m ranging from 1.01 to 1.5. The scattered intensity was calculated for many different orientations and then averaged using a Discrete Dipole Approximation (DDA) [*Purcell and Pennypac.cr*, 1973; *Draine and Flatau*, 1994; *Kalashnikova et al.*, 2004]. The results show power law descriptions of the scattering in q-space. One example is shown in Fig. 5.6 where $ka = 30$. The exponent for each ρ' is labeled by each plot. We noticed that exponents evolve with increasing ρ' again.

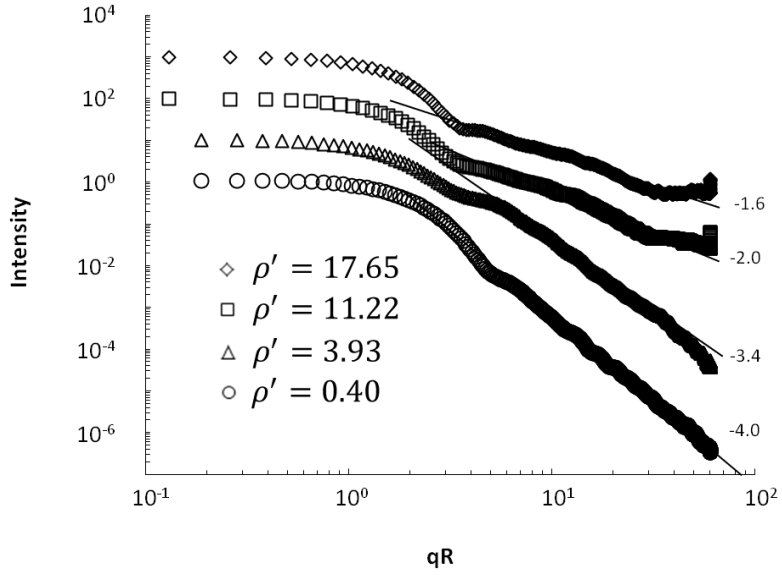

Figure 5.6 Q-space analysis on GRSs with ka=30, $\sigma = 0.2$, and $\nu = 0.3$. Lines are the power law fits and the numbers to the right of the plots are the exponents of the power law. A different multiplication factor is applied to the intensity for each plot to separate one from another.

5.1.5 Thickened Percolation Clusters

We wanted an irregularly shaped particle that was not a perturbation of a sphere to mimic certain irregular aerosol found in nature [*Popovicheva et al.*, 2012]. Our group's previous theorist Will Heinson simulated 3-dimensional dust agglomerate particles by using clusters made under the classical site percolation theory as a backbone [*Broadbent and Hammersley*, 1957; *Stauffer and Aharony*, 1994]. Percolation clusters are made on a square lattice that has sites randomly filled. When filled sites are neighbors, they are considered joined into a cluster. As more sites are filled, clusters become larger until one reaches the desired size and is set aside to be used as the backbone for the dust particle. Percolation clusters are described by their fractal dimension of $D_f \simeq 2.5$, therefore to make the fractal dimension match the spatial dimension of

three, the backbone cluster is then thickened by filling the neighboring sites. We will discuss more about fractals in Chapter 6. Figure 5.7 shows an example of a thickened percolation cluster.

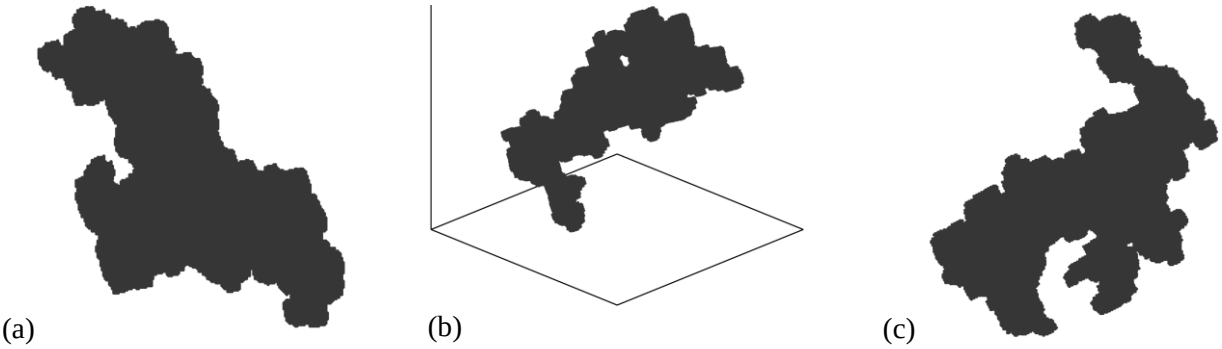

Figure 5.7 Thickened percolation cluster (a) side view, (b) three quarters view, and (c) top view.

The rotationally averaged scattered intensity was calculated using DDA [*Purcell and Pennypac.cr*, 1973; *Draine and Flatau*, 1994; *Kalashnikova and Sokolik*, 2004]. Then with the application of Q-space analysis as shown in Fig. 5.8, power law regimes after the Guinier regime become apparent. As before, the exponents evolve with increasing ρ'.

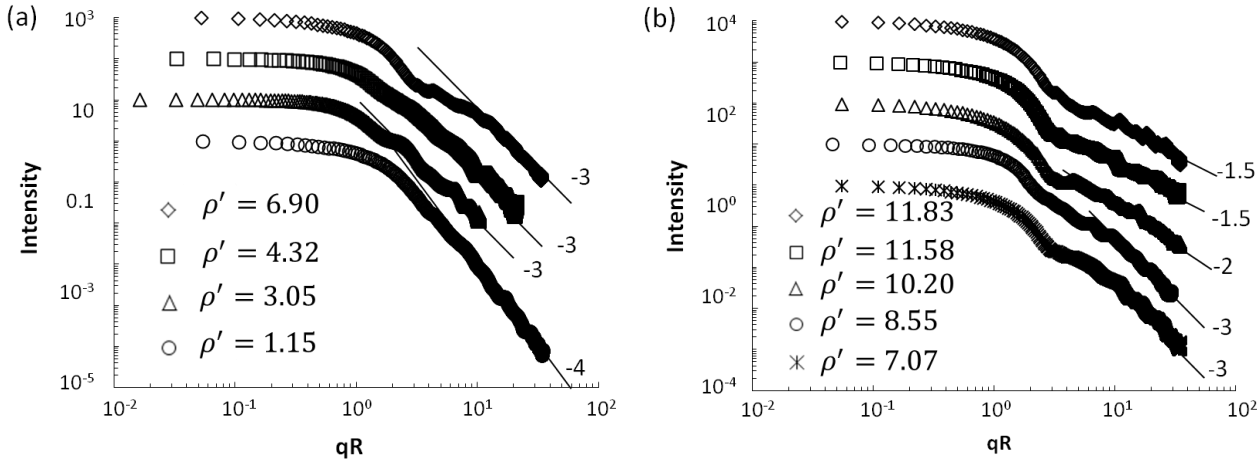

Figure 5.8 Q-space analysis on thickened percolation clusters. Lines are the power law fits and the numbers to the right of the plots are the exponents of the power law. A different multiplication factor is applied to the intensity for each plot for clarity.

5.1.6 Irregular spheres

Zubko and colleagues [*Zubko et al.*, 2006, 2008, 2009] used DDA [*Draine and Flatau*, 1994] to calculate light scattering by four different types of irregularly shaped spheres: strongly damaged spheres, e.g. see Fig. 5.9 [*Zubko et al.*, 2006], rough surface spheres, pocked spheres and agglomerated debris particles. In collaboration with Zubko our group applied Q-space analysis and reported the results including power law exponents in [*Sorensen et al.*, 2014].

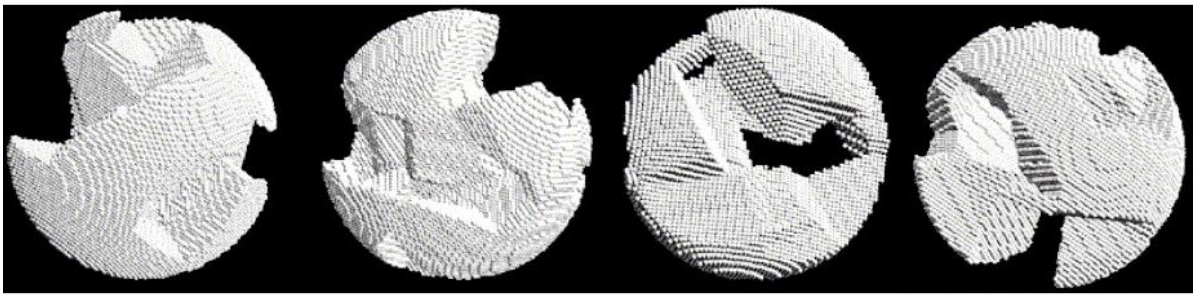

Figure 5.9 Strongly damaged spheres from [*Zubko et al.*, 2006].

5.2 The exponent of Q-space analysis as a function of ρ'

Figure 5.10 is a plot of the power law exponents uncovered by Q-space analysis versus the internal coupling parameter ρ' for all the non-fractal irregularly shaped particles studied above. Figure 5.10 clearly shows an undeniable trend that as ρ' increases, the absolute value of the exponents from the power law regimes decrease, and that all the particles fall on the same trend regardless of the detail of their structure. The absolute value of the exponents start from 4 when ρ' is small. As ρ' increases, the exponents decrease until the trend levels off at $\rho' \gtrsim 10$ where the exponents reach a constant 1.75 ± 0.25. Appendix A shows the ρ' values and the corresponding exponent absolute values for all the data presented in Fig. 5.10.

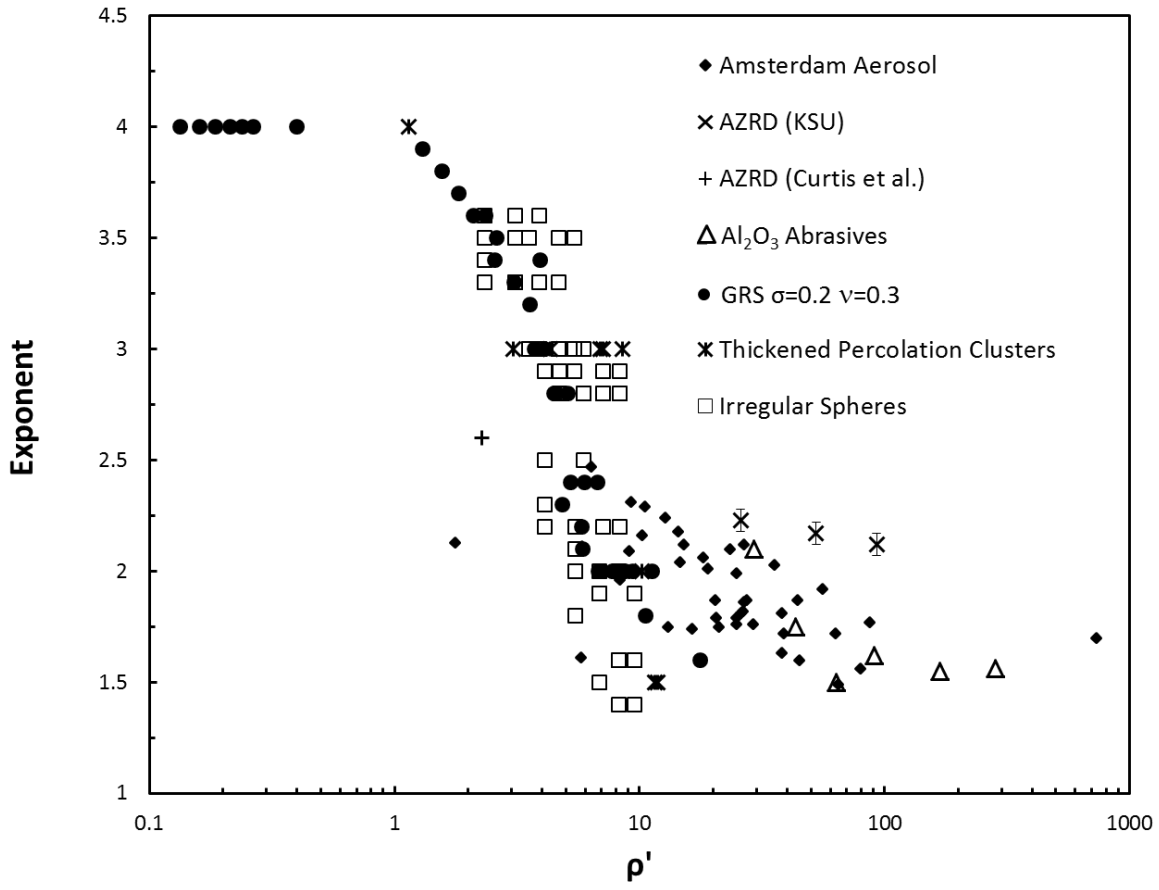

Figure 5.10 The exponents of the power laws vs. the internal coupling parameter ρ'.

In the limit of $\rho' \to 0$, which is the RDG limit, the power law regime in general obeys [*Oh and Sorensen*, 1999]

$$I(q) \sim q^{-(2D_m - D_s)}. \tag{5.1}$$

In Eq. (5.1) D_m is the particle mass scaling dimension and D_s is the particle surface scaling dimension. For example, spheres have $D_m = 3$ and $D_s = 2$ to yield via Eq. (5.1) the Porod exponent 4 [*Porod*, 1951] when $\rho' < 1$. Although we could only approach small ρ' values for theoretical calculations in Fig. 5.10, the experimental data follow the similar trend of the theoretical data at larger ρ' values. The similar trend, at large, implies that all shapes would have

a power law exponent of 4 when $\rho' < 1$. If true, then all the irregular shapes studied here and displayed in Fig. 5.10 have $D_m = 3$ and $D_s = 2$; the same as spheres, and hence do not have the fractal morphology, which is also collaborated by microscope images. A corollary to this is that "regularly shaped" spherical particles with $\rho' < 1$ fall on the trend of Fig. 5.10.

It is important to note that another type of irregularly shaped particle which we will discuss more about in Chapter 6, the fractal aggregate, does not fall on the trend in Fig. 5.10. Reference [*Sorensen*, 2001] shows that the phase shift parameter $\rho \to 0$ as the aggregate size increases when $D_m < 2$. The same argument can be applied to ρ'. Furthermore due to their fractal hence ramified nature, the internal coupling is usually weak even when D_m is larger than two. Fractal aggregates have $D_m = D_s$, to yield the well known light scattering result that $I \sim q^{-D_m}$. Thus a fractal aggregate can have $\rho' < 1$, but a power law exponent much less than 4, a result not on the trend in Fig. 5.10. We conclude that the particle types studied in this work cannot be represented by fractal morphology.

At this time, we offer a qualitative explanation for the power law exponent behavior as a function of ρ'. To explain the exponent behavior as a function of ρ', we consider the following facts: the forward scattering lobe intensity decreases relative to Rayleigh scattering; on the other hand, the Rayleigh normalized scattering at the largest value of $qR = 2kR$ remains approximately constant as ρ' increases. This implies that the intensity difference between the forward and backward scattered light is less for larger ρ'. This conclusion is consistent with an exponent decreasing with increasing ρ'. However, we cannot explain the remarkable uniformity of the power laws. In Chapter 4, we observed the kink for the three largest grits. The exponents for the grits in Fig. 5.10 are notwithstanding the kink. Note that the three largest grits, which showed the kink, are in a regime of $\rho' \gtrsim 100$ which has not been sufficiently explored in

previous work [*Munoz et al.*, 2000, 2001, 2002, 2004, 2006, 2007, 2012; *Volten et al.*, 2001, 2006; *Curtis et al.*, 2008; *Laan et al.*, 2009; *Sorensen et al.*, 2014; *Wang et al.*, 2015; *Maughan et al.*, 2016]. There is only one point at $\rho' \simeq 730$ for Sahara sand (Libya) measured by the Amsterdam-Granada group, the data for which did display a uniform power law. The $\rho' \gtrsim 100$ region needs further study. If large ρ' is not the cause of the kink, we speculate that the kink could be due to the higher degree of symmetry of the abrasives than the other dust particles.

5.3 Summary

Q-space analysis reveals power laws with quantifiable exponents for all irregularly shaped particles, both real and simulated. Furthermore, all the irregularly shaped particles studied so far display a scattering pattern as shown in Fig. 5.11. A constant forward scattering lobe at small q is followed by, at larger q, a crossover, Guinier regime near $q \simeq R^{-1}$, where R is a radial dimension; a power law regime; and finally an enhanced backscattering regime, the Glory, is sometimes observed at the largest values of q near 2k. This description applies to spheres as well, except the power law regime has more than a single power law as described above. Large abrasives have the similar behavior as spheres. These simple patterns give a unified description for all particle shapes. We suggest that Fig. 5.11 very likely represents a fundamental paradigm for scattering regimes obeyed by irregularly shaped particles. This rather surprising result means that the apparent complexity in shapes that these various samples represent has only a minor influence of the details of their angular scattering patterns.

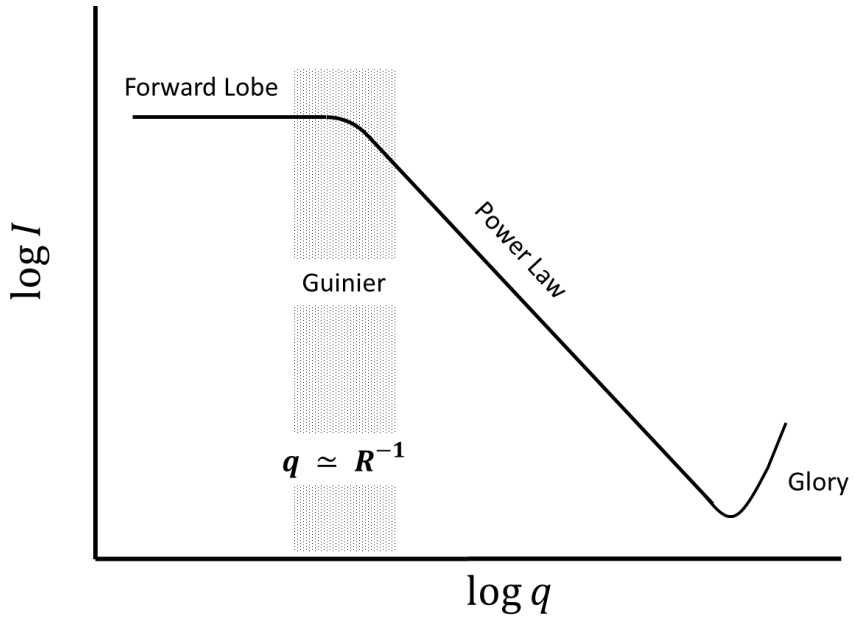

Figure 5.11 A generalized schematic of Q-space analysis for non-spherical particles. Scattered intensity I (a.u.) is plotted vs. q (cm^{-1}) on a log-log scale.

The power law exponents show a universal functionality with respect to the internal coupling parameter ρ' regardless of their specific structure. The exponents start from 4, consistent with the RDG, diffraction limit, and then beginning near $\rho' \simeq 1$, decrease with increasing ρ' until the exponents reach a constant 1.75 ± 0.25 when $\rho' \gtrsim 10$. The microscope images and the diffraction limit exponent when $\rho' < 1$ imply that despite their irregular structures, all the particles studied here have a mass scaling dimension of $D_m = 3$ and a surface scaling dimension of $D_s = 2$. This is different than fractal aggregates that have a single power law equal to the fractal dimension D_f but different scaling dimensions $D_f = D_m = D_s < 3$. Spheres (a "regular" shape), on the other hand, have $D_m = 3$ and $D_s = 2$ but do not show a single power law nor the same functionality with ρ'. Thus it appears that Q-space analysis can differentiate between spheres and these two types of irregularly shaped particles. Furthermore,

these observations suggest that the ill-defined terms “regular” and “irregular” might gain some resolution with these and future observations.

The ratio of forward to backscattered intensities is of critical importance to atmospheric radiative transfer calculations, as it changes the computed heating or cooling properties of layers of dust aerosols. Figures 5.1 – 5.3 demonstrate that lab data frequently do not measure at small enough q values (i.e., small enough scattering angles) to accurately determine the Guinier regime and the scattered intensity in the forward direction. This problem must be addressed in future measurements. However, until that time, Figure 5.11 combined with a known effective size and refractive index with which one can calculate ρ', the power law exponent determined empirically with Fig. 5.11, and finally the position of the Guinier regime from the effective size, would allow this ratio to be calculated.

Chapter 6 - Soot Fractal Aggregates

Particles emitted from high temperature combustion systems like those found in diesel engines, coal burning power plants, and biomass burning are aggregates composed of repeating black carbon spherules (monomers) [*Sorensen*, 2001]. The aggregates are typically less than 1μm. They have fractal morphology and are highly absorbing of solar radiation due to their black color.

Fractals have repeating branching structures, e.g. trees or river deltas, and from the repeating structure, a scale invariance develops. An example of scale invariance that people are familiar with is trees. Break off a branch and put it the ground and you have a great stand in for a tree in a miniature model or diorama. The part looks like the whole; thus trees are scale invariant. Another consequence of the repeating branching nature of fractals is that their mass scaling dimension is a fraction of the spatial dimension d and thus is called the fractal dimension D_f (the reason that fractals are called fractals). The volume of the material V in a soot fractal is equal to the number of monomers N multiplied by the volume of each monomer v, $V_{mat} = Nv$. Since the mass or in this case N scales as r^{D_f}, V_{mat} is related to the fractal radius r by $V_{mat} \sim r^{D_f}$ where $D_f < 3$ .Yet the volume that the fractal inhabits will go as $V_{frac} \sim r^3$ which is greater than V_{mat}. The main consequence of an objects having a $D_f < d$ is that an object can reach larger sizes without needing much material. Such objects tend to have many voids in their structure and are often described as “fluffy”.

From previous work [*US EPA*, n.d.; *Bond et al.*, 2004, 2007; *Bond and Bergstrom*, 2006], we use the term “soot” to imply high absorbance black carbonaceous aggregates of nanoparticles

with diameters of a few tens of nanometers arranged in fractal morphology, which are obtained from incomplete combustion. These aggregates are well described by Eq. (6.1).

$$N = k_0 \left(\frac{R_g}{a}\right)^{D_f}, \tag{6.1}$$

where N is the total number of monomers, k_0 is the prefactor, R_g is the radius of gyration of the fractal aggregate, and a is the radius of the monomer. It has been observed that when these aggregates form under diffusive motion, they display $D_f = 1.8$ and $k_0 = 1.35$. The fractal dimension is 1.8 for many soot aggregates and is well described by the diffusion limited cluster-cluster aggregation (DLCA) algorithms [*Sorensen*, 2001]. Figure 6.1 is a simulated soot aggregate [*Heinson*, 2015] made using a DLCA algorithm.

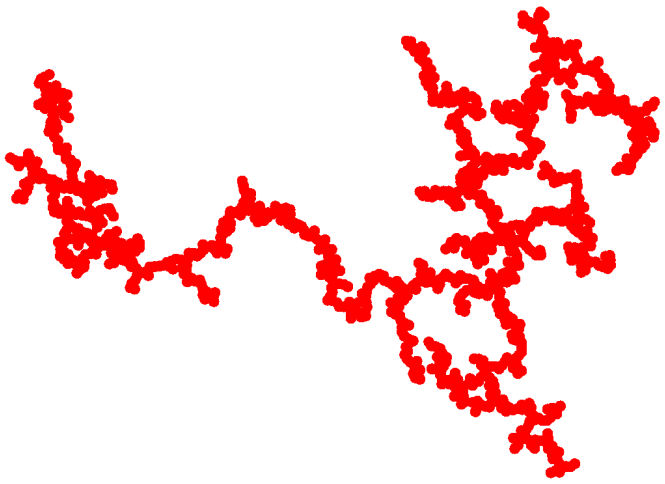

Figure 6.1 Simulated soot aggregate [*Heinson*, 2015] made using DLCA algorithm [*Sorensen*, 2001].

The soot aggregates studied in this chapter are well represented by such simulated aggregates. A great deal of work describing light scattering from soot has come from our lab over the years [*Zhang et al.*, 1988; *Gangopadhyay et al.*, 1991; *Sorensen et al.*, 1992a, 1992b,

2003; *Cai et al.*, 1993; *Lu and Sorensen*, 1994; *Oh and Sorensen*, 1997; *Sorensen*, 2001; *Kim et al.*, 2004, 2006; *Dhaubhadel et al.*, 2009; *Berg and Sorensen*, 2013; *Liu et al.*, 2015].

The Intergovernmental Panel on Climate Change (IPCC) Forth Assessment Report has shown the scientific understanding of black carbon aerosols such as the ones studied in this chapter to be lacking in regards to their effects on global radiation budget. Climate models have used the Lorenz-Mie theory to estimate the optical properties. But the Lorenz-Mie theory does a poor job estimating optical properties due to these aggregates' non-spherical fractal shape. This work was mostly limited to phase function measurements. The general conclusion [*Zhang et al.*, 1988] was that this scattering was well described by the RDG approximation where the scattering was due to diffraction. At first glance the use of this approximation seems misguided due to the strong refractive nature of the constituent monomers, but due to the fractal or fluffy nature of soot aggregates with their effective $\rho' < 1$ [*Sorensen*, 2001]. Under this approximation, the overall scattering and absorption cross sections can be determined under the assumption of the individual monomers of the soot aggregate acting as Rayleigh scatterers and absorbers. Polarization effects have been studied much less frequently [*Lu and Sorensen*, 1994].

West [*West*, 1991] performed DDA calculations on diffusion limited aggregation (DLA) aggregates (not DLCA) with a fractal dimension of 2.5 for a variety of monomer and aggregate sizes with refractive indices in the range of n = ca. 1.7 + 0.0009i to 0.21i. However, it is now well known that DLA does not describe naturally occurring aggregates such as soot. Volten et al. [*Volten et al.*, 2007] studied fluffy particles of minerals but no physical characterization was made involving fractal dimension or *in situ* aggregate size. Hamadcik and coworkers [*Hadamcik et al.*, 2006, 2007; *Francis et al.*, 2011] have studied fluffy aggregates of minerals and soot, some quite large in the 10's of microns range. However, none of their works measured scattering

function or the aggregate size explicitly while the polarization measurements were being made. Moreover, the soot they studied was from a toluene flame, and such soot has a hybrid superaggregate morphology [*Kim et al.*, 2004].

Given this background, there is both a need and an opportunity to study the complete scattering matrix from soot and other aggregates carefully and completely. We have recently begun *in situ* studies of the entire scattering matrix for soot from a C_2H_4/C_3H_8 premixed flame.

6.1 Premixed Burner

Figure 6.2(a) shows the picture of the premixed burner we designed and built with a suction nozzle, with Fig. 6.2(b) displaying the burner main body schematic drawing and Fig. 6.2(c) two disassembled burner parts. As shown in Fig. 6.2(b), the main body of the burner was made of 6mm copper tubing and two Tee fittings forming two "T" joints. C_2H_4 runs through a copper tubing joins another copper tubing which C_3H_8 runs through, by a Tee fitting forming a "T" joint. C_2H_4 and C_3H_8 were mixed coming out of the Tee fitting connecting to a copper tubing, which joins another copper tubing which O_2 runs through, by a second Tee fitting forming another "T" joint. Then C_2H_4, C_3H_8, and O_2 were mixed coming out of the second Tee fitting connecting to a copper tubing at the end of which we used a coupling to mount a frit, which was a porous stone. The use of the frit insures that the flame was one dimensional along vertical axis. Each gas passed through a flow meter (Matheson) and then a flow controller (Omega). The flow rate range of the flow controllers is from 0 to 200 ml/min. We let the gas pass through the flow meters first to make sure the flow rate stayed below the maximum scale of the flow controller.

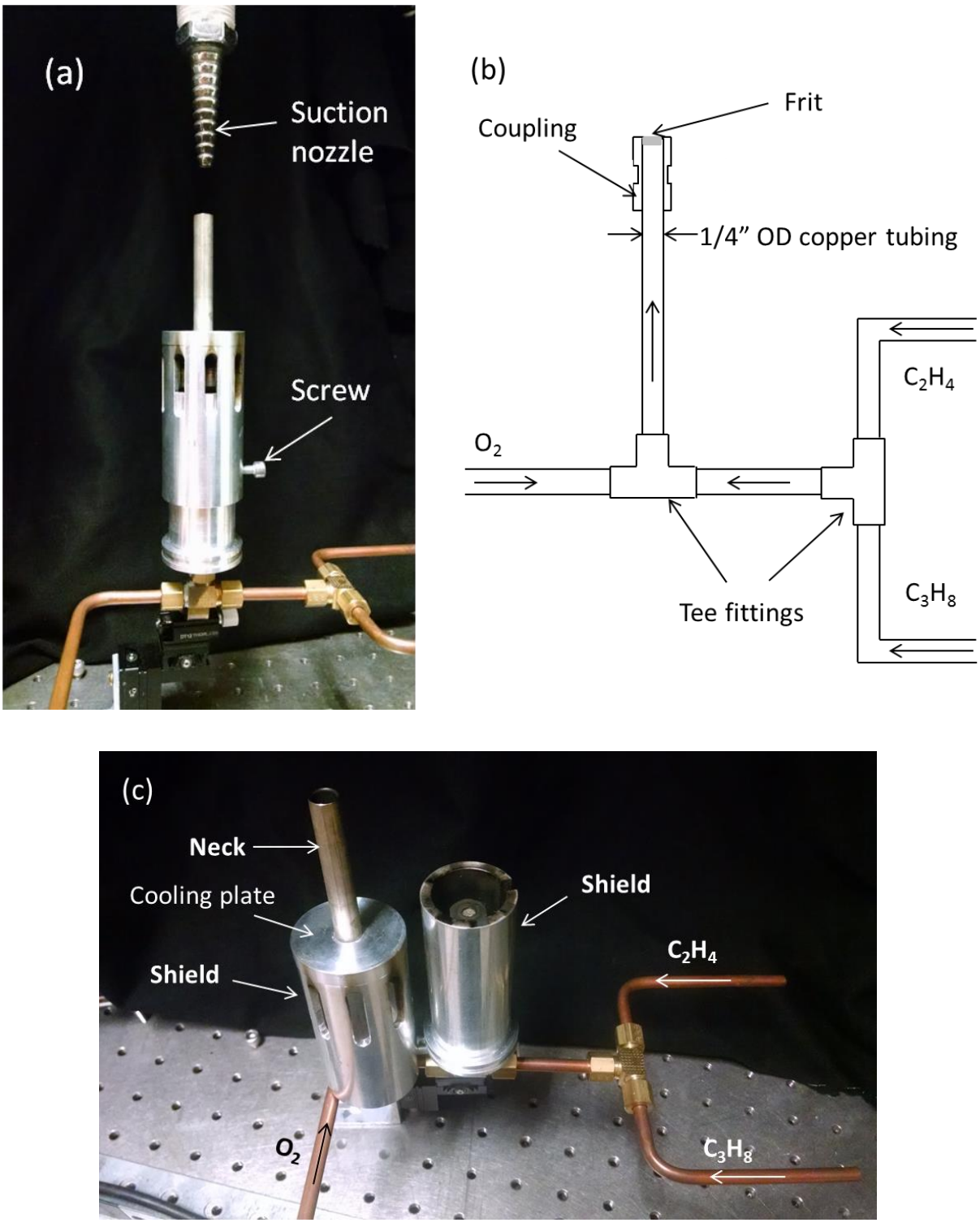

Figure 6.2 (a) A picture of the premixed burner we designed and built with a suction nozzle connected to a vacuum cleaner; (b) schematic drawing of the burner main body and (c) two disassembled burner parts with major elements labeled.

As indicated in Fig. 6.2(c), other than the main body of the burner we built a cylindrical shield surrounding the burner. The shield was a 7.5cm long, 1.8cm inner diameter and 2.5cm outer diameter cylinder with the copper tubing at the center. Additionally, we built an extra "cap" for the burner to wear. The bottom part of the "cap" was a 7.5cm long and slightly larger than 2.5cm inner diameter cylinder which can slide along the burner shield. A screw as shown in Fig. 6.2(a) was used to hold the "cap" on position. The bottom cylinder had six open slots symmetrically along the wall. Through one of the slots we can stick a match to light the burner. The two cylinders work together as a complete shield to block the outside air flow from the flame. The top of the "cap" is a 5cm long and 6mm in diameter neck where the soot comes out. Between the bottom cylinder and the neck there was a 0.6mm thick solid plate working as a cooling plate which stabilizes the soot stream in some degree. The neck stabilized the soot stream. With the help of a suction nozzle (plumbing fittings, the size of the end matched the soot stream diameter), as indicated in Fig. 6.2(a), which confined the soot stream, we were able to produce soot from a flame stable enough to measure the phase function.

6.2 Results

Note that the phase function we measured for soot was obtained by sending in vertically polarized incident light. Figure 6.3 shows preliminary data from the experiment where the flow rates of C_2H_4, C_3H_8, and O_2 were 115, 41, and 84 ml/min respectively. That was the optimized flow rate ratio to get soot out the flame, decent signal to noise ratio, and minimum anti-correlation at small q. "Anti-correlation" implies the decreasing intensity as q decreases, slightly shown in Fig. 6.3 at small q. A power law with exponent -1.85 implied the aggregates had a

fractal dimension of $D_f = 1.85$. It also showed a Guinier regime from which the radius of gyration determined as $R_g = 0.39\mu m$.

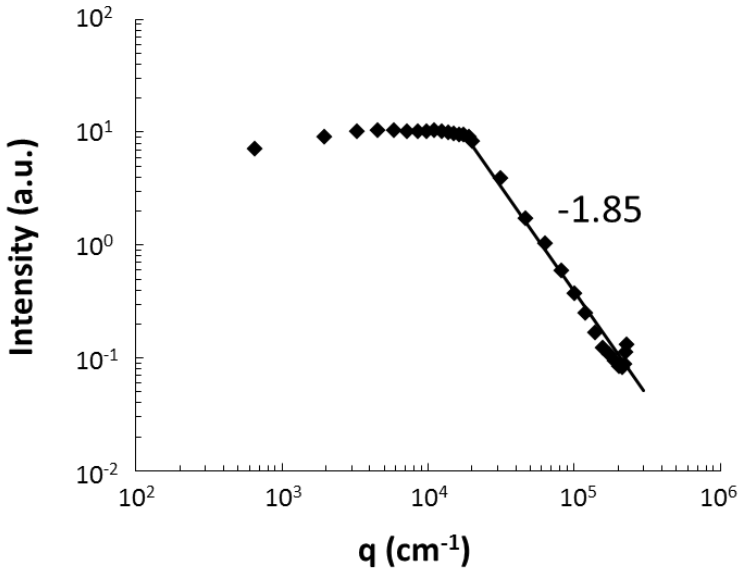

Figure 6.3 Preliminary data of soot produced from our premixed burner.

Additionally, we collected the soot freshly produced from the flame on a TEM grid and conducted TEM imaging as shown in Fig. 6.4. A scale bar of $0.699\mu m$ across one soot fractal aggregate indicates its approximate visible optical size. Considering light scattering was strongly affected by the largest particles in an ensemble. $2R_g = 0.78\mu m$ was in the reasonable range.

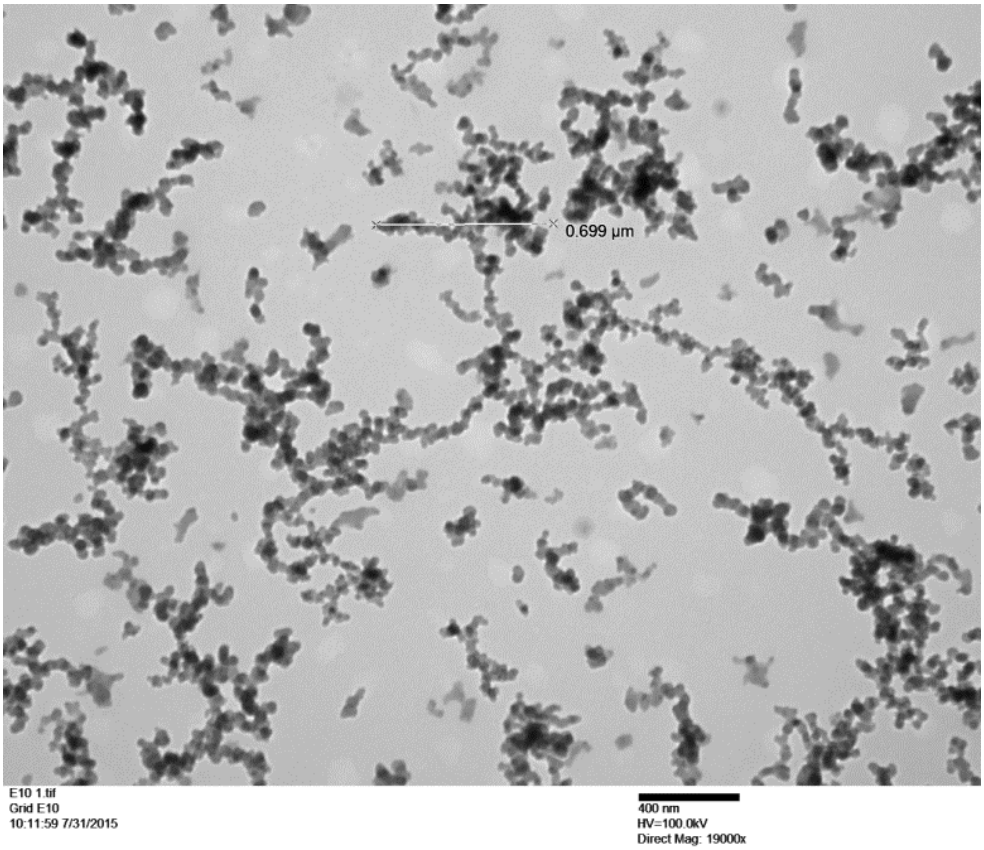

Figure 6.4 TEM image of the soot freshly produced from the premixed burner. A scale bar of $0.699\mu m$ across one soot fractal aggregate indicated its approximate visible optical size.

6.3 Discussion

In Fig. 6.3, where the preliminary data was from the measured ensemble of soot fractal aggregates, surprisingly, an enhanced backscattering was observed. Previous experimental work [*Zhang et al.*, 1988; *Gangopadhyay et al.*, 1991; *Sorensen et al.*, 1992a, 1992b, 2003; *Lu and Sorensen*, 1994] stopped at 120° or less, however the enhanced backscattering in Fig. 6.3 starts at ca. 130°. Theoretical work which considers only one aggregate at a time has never shown an enhanced backscattering along the scattering angle θ (hence q). We speculate the enhanced backscattering was due to the natural property of an ensemble of soot particles: the scattered light from one soot particle gets reflected into the backward direction by other soot particles.

[*Mishchenko and Liu*, 2007] has shown the evolution of backscattering for a 3D volume filled with densely packed randomly distributed, wavelength-sized spherical particles. Our soot system might have the same situation as [*Mishchenko and Liu*, 2007]. To diminish this possible multiple scattering effect we tried to dilute our soot system by decreasing the C_2H_4 flow rate and increasing the C_3H_8 flow rate. When the flow rates of C_2H_4, C_3H_8, and O_2 were 115, 41, and 84 ml/min, respectively, as we mentioned in section 6.2, we minimized anti-correlation at small q, however, the enhanced backscattering did not disappear. Keeping the O_2 flow rate constant, 115/41 was the lowest C_2H_4/C_3H_8 ratio at which we could still get soot out of the flame. Figure 6.5 shows the examples of anti-correlation; (a) shows strong decreasing trend as q gets smaller for small q regime when the C_2H_4/C_3H_8 ratio is high; when we lower the C_2H_4/C_3H_8 ratio, as shown in (b), the anti-correlation diminishes.

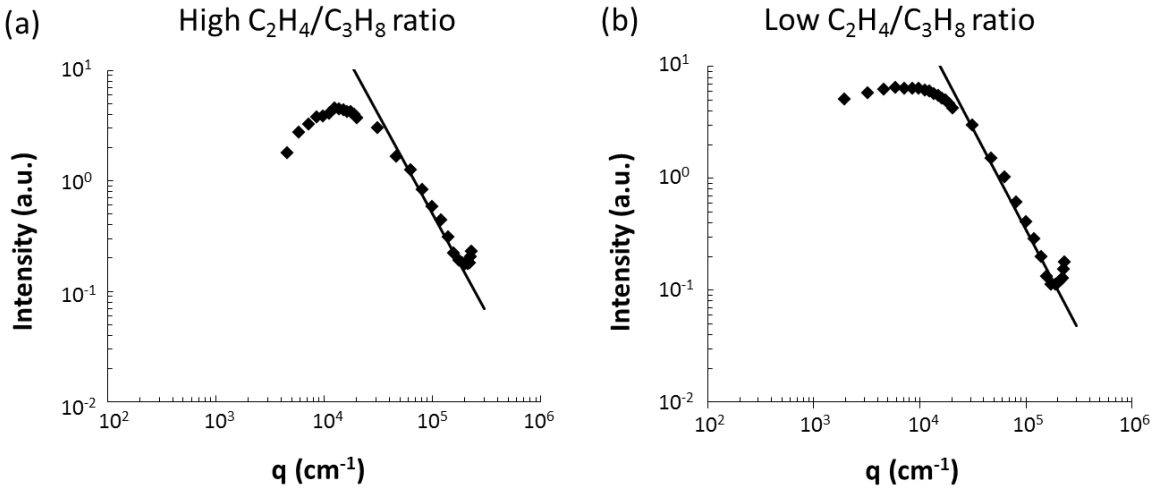

Figure 6.5 Examples of anti-correlation; (a) shows strong decreasing trend as q got smaller for small q regime; when we decreased the C_2H_4 to C_3H_8 ratio, as shown in (b), the anti-correlation was smaller.

We would like to dilute the soot system more and see if the enhanced backscattering dramatically changes or not. With the help of Colorado State University, Department of

Atmospheric Science (Sonia Kreidenweis), we are looking forward to come up a dilution system for our soot fractal aggregates.

6.4 Summary

With the premixed burner we designed, we produced soot fractal aggregates which are well described by diffusion limited cluster-cluster aggregation. We then measured the phase function using our experimental setup. From the Guinier regime of the phase function, the radius of gyration of the soot fractal aggregate is ca. $0.39\mu m$. Surprisingly, an enhanced backscattering starts at ca. 130° which was never observed before.

An important problem for atmospheric aerosols is that soot from combustion becomes humidified in the atmosphere and the effects of this on the optical properties need to be understood. We have an incipient collaboration with Colorado State University, Department of Atmospheric Science (Sonia Kreidenweis) who will help us create "wet" soot. Their experience will help us greatly. The subject has seen theoretical studies [*Kocifaj et al.*, 2008; *Yin and Liu*, 2010; *Liu et al.*, 2012] that indicate that cross sections increase with the presence of a water coating with an increase in the forward scattering but decrease in the backscattering. Theories need experimental validation. The literature indicates that soot particles can be coated using a simple flow tube with water and liquid alkanes as described by Prather and coworkers [*Noble and Prather*, 1996; *Spencer and Prather*, 2006]. Bueno et al. [*Bueno et al.*, 2011] also describe a method to do humidify soot. Another method for hydration would be to use a novel continuous flow stream-wise thermal gradient CNC device created by Roberts and Nenes [*Roberts and Nenes*, 2005].

The particles can be dried again to make "cloud processed soot" – another important particle for atmospheric and global warming problems. After scattering and direct in situ observation, these can be collected and studied via TEM.

The past ten years has seen the rise of superaggregates. Superaggregates, discovered in our laboratory [*Sorensen et al.*, 1998, 2003; *Kim et al.*, 2004, 2006], has a hybrid fractal morphology with DLCA structure with a fractal dimension of 1.8 for length scales less than about 1 micron and a percolation structure with fractal dimension of 2.6 for length scales greater than 1 micron. It is found in diffusion flames of heavily sooting fuels. Recently superaggregates have been found in turbulent pool fires [*Kearney and Pierce*, 2012] and forest fires [*Chakrabarty et al.*, 2014]. Hence superaggregates could well be relevant to the atmospheric environment. Chakrabarty et al. [*Chakrabarty et al.*, 2012, 2014] have shown that an inverted flame [*Stipe et al.*, 2005] can be used to make superaggregates. Given this rise, we will initiate experiments to study light scattering by superaggregates.

Chapter 7 - Conclusion and Future Work

We presented light scattering studies of irregularly shaped particles using the experimental apparatus we built. Our apparatus was thoroughly calibrated, and we were able to measure all six independent scattering matrix elements (S_{11}, S_{12}, S_{22}, S_{33}, S_{34}, and S_{44}). Our apparatus has some advantages over other similar instruments such that it detects light at many angles simultaneously from a small angle 0.32° to 157°. It is very important for detecting the beginning of scattering angle functionality in the small angle limit, especially for large particles, in order to determine particle sizes using Guinier analysis. We have studied all six scattering matrix elements of Arizona Road Dust. According to the measurements of six independent matrix elements, irregularly shaped particles scatter light differently than spherical particles. We strongly focused on the phase function; uniquely, we applied Q-space analysis to the phase function. Q-space analysis involves plotting the scattering intensity vs. the magnitude of the scattering wave vector $q = (4\pi/\lambda)\sin(\theta/2)$ where λ is the optical wavelength and θ is the scattering angle, on a double logarithmic plot. We have measured and studied the phase functions of Al_2O_3 abrasives; we compared the scattering from the abrasives with the scattering of spheres and found a semi-quantitative similarity between the two. Additionally, we collected a large amount of experimental and theoretical phase function data of non-fractal irregularly shaped particles produced from our group and others and applied Q-space analysis. They all displayed a common scattering pattern which includes a q-independent forward scattering regime; a crossover, Guinier regime when q is near the inverse size; a power law regime with quantifiable exponents; and an enhanced backscattering regime is sometimes observed. Power law exponents show a quasi-universal functionality with the internal coupling parameter $\rho' = 2kR\left|\frac{m^2-1}{m^2+2}\right|$. The absolute value of the exponents start from 4 when $\rho' < 1$, the diffraction

limit, and decrease as ρ' increases until a constant 1.75 ± 0.25 when $\rho' \gtrsim 10$. We have begun the *in situ* studies of the soot fractal aggregates which have different morphologies than dust particles or abrasives particles. The soot fractal aggregates were freshly produced from a C_2H_4/C_3H_8 premixed burner we built. A power law with exponent -1.85 is seen to imply the aggregates have a fractal dimension of D_f = 1.85. Surprisingly, an enhanced backscattering has been observed.

In the future, based on the work we have done on AZRD and Al_2O_3 abrasives presented in Chapter 3 and 4, respectively, we would like to replace the 16 channel photodiode array in the forward direction with a 512 channel array, which would allow us to approach much smaller angles with higher angular resolution, and then we would be able to characterize the particles sizes more precisely. Based on a design by Ferri [*Ferri,* 1997] such small angle devices has been built and used before in our lab [*Sorensen et al.*, 2003; *Kim et al.*, 2004, 2006; *Dhaubhadel et al.*, 2009]. Until we achieve better data and determine the manner in which the Guinier Analysis can be applied to large irregularly shaped particles, further analysis of that sort is not realizable. An apparatus was designed, assembled, and well calibrated in our lab to measure the scattered light in the range of $180^\circ \pm 6^\circ$ [*Heffernan et al.*, n.d.]. Based on the same idea, we will add a backscattering detection for the angular range 160° to 179° to our current setup. We will put a photomultiplier (PMT) at an angle of ca. 12° to determine the absolute scattering cross sections. The PMT will provide the ability to make absolute scattering measurements by calibration with gases of known Rayleigh ratios which was done before in our lab [*Sorensen et al.*, 1992a; *Oh and Sorensen*, 1997] following D'Alessio [*D'Alessio*, 1981]. The overall purpose will be to obtain absolute light scattering measurements over essentially the complete angular range.

We now have new insights regarding the importance of high resolution, small angle

forward scattering and Q-space analysis. Thus more in depth studies of some dust previously studied are warranted. We will redo AZRD and Al_2O_3 abrasive particles and some Amsterdam-Granada dusts with the improved scattering apparatus to obtain calibrated scattering from 0.1° to 179°. These more complete data will be used for the Guinier, forward scattering and backscattering studies. Calibration to obtain absolute scattering cross section will give an unprecedented comparison to theory. With the foundations we have built, we hope eventually we will study soot coated with liquid in collaboration with Colorado State University, Department of Atmospheric Science (Sonia Kreidenweis).

All the work presented in this dissertation showed power laws for phase functions under Q-space analysis. Q-space analysis uncovers patterns common to *all* particles. Recall Fig. 5.11, a generalized schematic of Q-space analysis for irregularly shaped particles, a q-independent forward scattering regime is followed by a Guinier regime, a power law regime, and sometimes an enhanced back scattering regime. This description applies to spheres as well, except the power law regime has more than a single power law. Large abrasives have the similar behavior as spheres. These simple patterns give a unified description for all particle shapes. Moreover, the power law exponents have a universal functionality with ρ' for non-fractal aggregates. All the particles fall on the same trend regardless of the detail of their structure. The absolute value of the exponents start from 4 when ρ' is small. As ρ' increases, the exponents decrease until the trend levels off at $\rho' \gtrsim 10$ where the exponents reach a constant 1.75 ± 0.25. The microscope images and the diffraction limit exponent when $\rho' < 1$ imply that despite their irregular structures, all the non-fractal particles presented in this dissertation have a mass scaling dimension of $D_m = 3$ and a surface scaling dimension of $D_s = 2$.

References

Berg, M. J., and C. M. Sorensen (2013), Internal fields of soot fractal aggregates, *J. Opt. Soc. Am. A*, *30*(10), 1947, doi:10.1364/JOSAA.30.001947.

Berg, M. J., C. M. Sorensen, and A. Chakrabarti (2005), Patterns in Mie scattering: evolution when normalized by the Rayleigh cross section, *Appl. Opt.*, *44*(34), 7487–7493, doi:10.1364/AO.44.007487.

Bohren, C. F., and D. R. Huffman (1998), *Absorption and Scattering of Light by Small Particles*, Wiley-VCH, Weinheim.

Bond, T. C., and R. W. Bergstrom (2006), Light absorption by carbonaceous particles: An investigative review, *Aerosol Sci. Technol.*, *40*(1), 27–67, doi:10.1080/02786820500421521.

Bond, T. C., D. G. Streets, K. R. Yarber, S. M. Nelson, J.-H. Woo, and Z. Klimont (2004), A technology-based global inventory of black and organic carbon emissions from combustion, *J. Geophys. Res.*, *109*(D14), 43 pp., doi:10.1029/2003JD003697.

Bond, T. C., E. Bhardwaj, R. Dong, R. Jogani, S. Jung, C. Roden, D. G. Streets, and N. M. Trautmann (2007), Historical emissions of black and organic carbon aerosol from energy-related combustion, 1850-2000, *Glob. Biogeochem. Cycles*, *21*(2), GB2018, doi:10.1029/2006GB002840.

Broadbent, S. R., and J. M. Hammersley (1957), Percolation processes, *Math. Proc. Camb. Philos. Soc.*, *53*(03), 629–641, doi:10.1017/S0305004100032680.

Bueno, P. A., D. K. Havey, G. W. Mulholland, J. T. Hodges, K. A. Gillis, R. R. Dickerson, and M. R. Zachariah (2011), Photoacoustic Measurements of Amplification of the Absorption Cross Section for Coated Soot Aerosols, *Aerosol Sci. Technol.*, *45*(10), 1217–1230, doi:10.1080/02786826.2011.587477.

Cai, J., N. Lu, and C. M. Sorensen (1993), Comparison of size and morphology of soot aggregates as determined by light scattering and electron microscope analysis, *Langmuir*, *9*(11), 2861–2867, doi:10.1021/la00035a023.

Chakrabarty, R. K., M. A. Garro, E. M. Wilcox, and H. Moosmueller (2012), Strong radiative heating due to wintertime black carbon aerosols in the Brahmaputra River Valley, *Geophys. Res. Lett.*, *39*, L09804, doi:10.1029/2012GL051148.

Chakrabarty, R. K., N. D. Beres, H. Moosmüller, S. China, C. Mazzoleni, M. K. Dubey, L. Liu, and M. I. Mishchenko (2014), Soot superaggregates from flaming wildfires and their direct radiative forcing, *Sci. Rep.*, *4*, 5508.

Curtis, D. B., B. Meland, M. Aycibin, N. P. Arnold, V. H. Grassian, M. A. Young, and P. D. Kleiber (2008), A laboratory investigation of light scattering from representative

components of mineral dust aerosol at a wavelength of 550 nm, *J. Geophys. Res.-Atmospheres*, *113*(D8), D08210, doi:10.1029/2007JD009387.

D'Alessio, A. (1981), Laser Light Scattering and Fluorescence Diagnostics of Rich Flames Produced by Gaseous and Liquid Fuels, in *Particulate Carbon*, edited by D. C. Siegla and G. W. Smith, pp. 207–259, Springer US.

Dhaubhadel, R., A. Chakrabarti, and C. M. Sorensen (2009), Light Scattering Study of Aggregation Kinetics in Dense, Gelling Aerosols, *Aerosol Sci. Technol.*, *43*(11), 1053–1063, doi:10.1080/02786820903136908.

Draine, B., and P. Flatau (1994), Discrete-Dipole Approximation for Scattering Calculations, *J. Opt. Soc. Am. -Opt. Image Sci. Vis.*, *11*(4), 1491–1499, doi:10.1364/JOSAA.11.001491.

Dubovik, O. et al. (2006), Application of spheroid models to account for aerosol particle nonsphericity in remote sensing of desert dust, *J. Geophys. Res.-Atmospheres*, *111*(D11), D11208, doi:10.1029/2005JD006619.

Ferri, F. (1997), Use of a charge coupled device camera for low-angle elastic light scattering, *Rev. Sci. Instrum.*, *68*(6), 2265–2274, doi:10.1063/1.1148135.

Francis, M., J.-B. Renard, E. Hadamcik, B. Couté, B. Gaubicher, and M. Jeannot (2011), New studies on scattering properties of different kinds of soot and carbon-black, *J. Quant. Spectrosc. Radiat. Transf.*, *112*(11), 1766–1775, doi:10.1016/j.jqsrt.2011.01.009.

Gangopadhyay, S., I. Elminyawi, and C. M. Sorensen (1991), Optical structure factor measurements of soot particles in a prmixed flame, *Appl. Opt.*, *30*(33), 4859, doi:10.1364/AO.30.004859.

Ghan, S. J., and S. E. Schwartz (2007), Aerosol properties and processes - A path from field and laboratory measurements to global climate models, *Bull. Am. Meteorol. Soc.*, *88*(7), 1059–+, doi:10.1175/BAMS-88-7-1059.

Glatter, O., and O. Kratky (1982), *Small Angle X-ray Scattering*, Academic Press.

Gorner, P., D. Bemer, and J. F. Fabries (1995), Photometer measurement of polydisperse aerosols, *J. Aerosol Sci.*, *26*(8), 1281–&, doi:10.1016/0021-8502(95)00049-6.

Guinier, A., G. Fournet, and K. L. Yudowitch (1955), *Small-angle scattering of X-rays*, 1st edition., Wiley.

Hadamcik, E., J. B. Renard, A. C. Levasseur-Regourd, and J. Lasue (2006), Light scattering by fluffy particles with the PROGRA^2 experiment: Mixtures of materials, *J. Quant. Spectrosc. Radiat. Transf.*, *100*, 143–156, doi:10.1016/j.jqsrt.2005.11.032.

Hadamcik, E., J.-B. Renard, J. Lasue, A. C. Levasseur-Regourd, J. Blum, and R. Schraepler (2007), Light scattering by low-density agglomerates of micron-sized grains with the

PROGRA2 experiment, *J. Quant. Spectrosc. Radiat. Transf.*, *106*(1–3), 74–89, doi:10.1016/j.jqsrt.2007.01.008.

Hecht, E. (2002), *Optics*, Addison-Wesley.

Heffernan, B. M., Y. W. Heinson, J. B. Maughan, A. Chakrabarti, and C. M. Sorensen (n.d.), Measurements of the glory of micron-sized spherical particles., *Submitt. Appl. Opt.*

Heinson, W. R. (2015), Simulation studies on shape and growth kinetics for fractal aggregates in aerosol and colloidal systems, 9 June.

Heinson, W. R., A. Chakrabarti, and C. M. Sorensen (2015), A new parameter to describe light scattering by an arbitrary sphere, *Opt. Commun.*, *356*, 612–615, doi:10.1016/j.optcom.2015.08.067.

Heinson, Y. W., J. B. Maughan, W. R. Heinson, A. Chakrabarti, and C. M. Sorensen (2016), Light scattering Q-space analysis of irregularly shaped particles, *J. Geophys. Res. Atmospheres*, *121*(2), 682–691, doi:10.1002/2015JD024171.

Heinson, Y. W., A. Chakrabarti, and C. M. Sorensen (n.d.), A Light-Scattering Study of Al2O3 Abrasives of Various Grits, *Submitt. J. Quant. Spectrosc. Radiat. Transf.*

Henyey, L. G., and J. L. Greenstein (1941), Diffuse radiation in the Galaxy, *Astrophys. J.*, *93*, 70–83, doi:10.1086/144246.

Hoff, R. M., and S. A. Christopher (2009), Remote Sensing of Particulate Pollution from Space: Have We Reached the Promised Land?, *J. Air Waste Manag. Assoc.*, *59*(6), 645–675, doi:10.3155/1047-3289.59.6.645.

Hubbard, J. A. (2006), A study of aerodynamic deaggregation mechanisms and the size control of NanoActive^{TM} aerosol particles, Thesis, Kansas State University, 5 July.

Hulst, H. C. van de (1981), *Light Scattering by Small Particles*, Reprint, edition., Dover Publications, New York.

Hunt, A. J., and D. R. Huffman (1973), A new polarization-modulated light scattering instrument, *Rev. Sci. Instrum.*, *44*(12), 1753–1762, doi:10.1063/1.1686049.

Kahn, R. A., and B. J. Gaitley (2015), An analysis of global aerosol type as retrieved by MISR, *J. Geophys. Res.-Atmospheres*, *120*(9), 4248–4281, doi:10.1002/2015JD023322.

Kalashnikova, O. V., and I. N. Sokolik (2004), Modeling the radiative properties of nonspherical soil-derived mineral aerosols, *J. Quant. Spectrosc. Radiat. Transf.*, *87*(2), 137–166, doi:10.1016/j.jqsrt.2003.12.026.

Kalashnikova, O. V., D. J. Diner, R. A. Kahn, and B. J. Gaitley (2004), Dust aerosol retrieval results from MISR, vol. 5652, pp. 309–317.

Kearney, S. P., and F. Pierce (2012), Evidence of soot superaggregates in a turbulent pool fire, *Combust. Flame*, *159*(10), 3191–3198, doi:10.1016/j.combustflame.2012.04.011.

Kerker, M. (1969), *The Scattering of Light and Other Electromagnetic Radiation*, Academic Press.

Kim, W., C. M. Sorensen, and A. Chakrabarti (2004), Universal Occurrence of Soot Superaggregates with a Fractal Dimension of 2.6 in Heavily Sooting Laminar Diffusion Flames, *Langmuir*, *20*(10), 3969–3973, doi:10.1021/la036085+.

Kim, W., C. M. Sorensen, D. Fry, and A. Chakrabarti (2006), Soot aggregates, superaggregates and gel-like networks in laminar diffusion flames, *J. Aerosol Sci.*, *37*(3), 386–401, doi:10.1016/j.jaerosci.2005.05.022.

Kocifaj, M., F. Kundracík, and G. Videen (2008), Optical properties of single mixed-phase aerosol particles, *J. Quant. Spectrosc. Radiat. Transf.*, *109*(11), 2108–2123, doi:10.1016/j.jqsrt.2008.03.006.

Kuik, F., P. Stammes, and J. W. Hovenier (1991), Experimental determination of scattering matrices of water droplets and quartz particles, *Appl. Opt.*, *30*(33), 4872, doi:10.1364/AO.30.004872.

Laan, E. C., H. Volten, D. M. Stam, O. Munoz, J. W. Hovenier, and T. L. Roush (2009), Scattering matrices and expansion coefficients of martian analogue palagonite particles, *Icarus*, *199*(1), 219–230, doi:10.1016/j.icarus.2008.08.011.

Lamberg, L., K. Muinonen, J. Ylonen, and K. Lumme (2001), Spectral estimation of Gaussian random circles and spheres, *J. Comput. Appl. Math.*, *136*(1-2), 109–121, doi:10.1016/S0377-0427(00)00578-1.

Lambert, J. H., and E. (Ernst) Anding (1892), *Lamberts Photometrie : [Photometria, sive De mensura et gradibus luminus, colorum et umbrae] (1760)*, Leipzig : W. Engelmann.

Laven, P. (2004), Simulation of rainbows, coronas and glories using Mie theory and the Debye series, *J. Quant. Spectrosc. Radiat. Transf.*, *89*(1–4), 257–269, doi:10.1016/j.jqsrt.2004.05.026.

Levy, O., and D. Stroud (1997), Maxwell Garnett theory for mixtures of anisotropic inclusions: Application to conducting polymers, *Phys. Rev. B*, *56*(13), 8035–8046, doi:10.1103/PhysRevB.56.8035.

Liu, C., R. L. Panetta, and P. Yang (2012), The Influence of Water Coating on the Optical Scattering Properties of Fractal Soot Aggregates, *Aerosol Sci. Technol.*, *46*(1), 31–43, doi:10.1080/02786826.2011.605401.

Liu, C., Y. Yin, F. Hu, H. Jin, and C. M. Sorensen (2015), The Effects of Monomer Size Distribution on the Radiative Properties of Black Carbon Aggregates, *Aerosol Sci. Technol.*, *49*(10), 928–940, doi:10.1080/02786826.2015.1085953.

Lovesey, S. W. (1986), *The Theory of Neutron Scattering from Condensed Matter: Volume I*, Oxford University Press.

Lu, N., and C. M. Sorensen (1994), Depolarized light scattering from fractal soot aggregates, *Phys. Rev. E*, *50*(4), 3109–3115, doi:10.1103/PhysRevE.50.3109.

Maughan, J. B., C. M. Sorensen, and A. Chakrabarti (2016), Q-space analysis of light scattering by Gaussian Random Spheres, *J. Quant. Spectrosc. Radiat. Transf.*, *174*, 14–21, doi:10.1016/j.jqsrt.2015.12.002.

Mie, G. (1908), Beiträge zur Optik trüber Medien, speziell kolloidaler Metallösungen, *Ann. Phys.*, *330*(3), 377–445, doi:10.1002/andp.19083300302.

Mishchenko, M. I. (2014), *Electromagnetic Scattering by Particles and Particle Groups: An Introduction*, Cambridge University Press.

Mishchenko, M. I. (n.d.), *Scattering, Absorption, and Emission of Light by Small Particles*.

Mishchenko, M. I., and L. Liu (2007), Weak localization of electromagnetic waves by densely packed many-particle groups: Exact 3D results, *J. Quant. Spectrosc. Radiat. Transf.*, *106*(1–3), 616–621, doi:10.1016/j.jqsrt.2007.01.039.

Mishchenko, M. I., J. W. Hovenier, and L. D. Travis (1999), *Light Scattering by Nonspherical Particles: Theory, Measurements, and Applications*, Academic Press.

Mokhtari, T., C. M. Sorensen, and A. Chakrabarti (2005), Multiple-scattering effects on static light-scattering optical structure factor measurements, *Appl. Opt.*, *44*(36), 7858, doi:10.1364/AO.44.007858.

Muinonen, K. (1998), Introducing the Gaussian shape hypothesis for asteroids and comets, *Astron. Astrophys.*, *332*(3), 1087–1098.

Muinonen, K., and J. S. V. Lagerros (1998), Inversion of shape statistics for small solar system bodies, *Astron. Astrophys.*, *333*(2), 753–761.

Muinonen, K., E. Zubko, J. Tyynela, Y. G. Shkuratov, and G. Videen (2007), Light scattering by Gaussian random particles with discrete-dipole approximation, *J. Quant. Spectrosc. Radiat. Transf.*, *106*(1-3), 360–377, doi:10.1016/j.jqsrt.2007.01.049.

Munoz, O., H. Volten, J. F. de Haan, W. Vassen, and J. W. Hovenier (2000), Experimental determination of scattering matrices of olivine and Allende meteorite particles, *Astron. Astrophys.*, *360*(2), 777–788.

Munoz, O., H. Volten, J. F. de Haan, W. Vassen, and J. W. Hovenier (2001), Experimental determination of scattering matrices of randomly oriented fly ash and clay particles at 442 and 633 nm, *J. Geophys. Res.-Atmospheres*, *106*(D19), 22833–22844, doi:10.1029/2000JD000164.

Munoz, O., H. Volten, J. F. de Haan, W. Vassen, and J. W. Hovenier (2002), Experimental determination of the phase function and degree of linear polarization of El Chichon and Pinatubo volcanic ashes, *J. Geophys. Res.-Atmospheres*, *107*(D13), 4174, doi:10.1029/2001JD000983.

Munoz, O., H. Volten, J. W. Hovenier, B. Veihelmann, W. J. van der Zande, L. Waters, and W. I. Rose (2004), Scattering matrices of volcanic ash particles of Mount St. Helens, Redoubt, and Mount Spurr Volcanoes, *J. Geophys. Res.-Atmospheres*, *109*(D16), D16201, doi:10.1029/2004JD004684.

Munoz, O., H. Volten, J. W. Hovenier, M. Min, Y. G. Shkuratov, J. P. Jalava, W. J. van der Zande, and L. Waters (2006), Experimental and computational study of light scattering by irregular particles with extreme refractive indices: hematite and rutile, *Astron. Astrophys.*, *446*(2), 525–535, doi:10.1051/0004-6361:20053727.

Munoz, O., H. Volten, J. W. Hovenier, T. Nousiainen, K. Muinonen, D. Guirado, F. Moreno, and L. B. F. M. Waters (2007), Scattering matrix of large Saharan dust particles: Experiments and computations, *J. Geophys. Res.-Atmospheres*, *112*(D13), D13215, doi:10.1029/2006JD008074.

Muñoz, O., F. Moreno, D. Guirado, J. L. Ramos, A. López, F. Girela, J. M. Jerónimo, L. P. Costillo, and I. Bustamante (2010), Experimental determination of scattering matrices of dust particles at visible wavelengths: The IAA light scattering apparatus, *J. Quant. Spectrosc. Radiat. Transf.*, *111*(1), 187–196, doi:10.1016/j.jqsrt.2009.06.011.

Munoz, O., F. Moreno, D. Guirado, D. D. Dabrowska, H. Volten, and J. W. Hovenier (2012), The Amsterdam-Granada Light Scattering Database, *J. Quant. Spectrosc. Radiat. Transf.*, *113*(7), 565–574, doi:10.1016/j.jqsrt.2012.01.014.

Noble, C. A., and K. A. Prather (1996), Real-Time Measurement of Correlated Size and Composition Profiles of Individual Atmospheric Aerosol Particles, *Environ. Sci. Technol.*, *30*(9), 2667–2680, doi:10.1021/es950669j.

Nousiainen, T., O. Munoz, H. Lindqvist, P. Mauno, and G. Videen (2011a), Light scattering by large Saharan dust particles: Comparison of modeling and experimental data for two samples, *J. Quant. Spectrosc. Radiat. Transf.*, *112*(3), 420–433, doi:10.1016/j.jqsrt.2010.09.003.

Nousiainen, T., H. Lindqvist, G. M. McFarquhar, and J. Um (2011b), Small Irregular Ice Crystals in Tropical Cirrus, *J. Atmospheric Sci.*, *68*(11), 2614–2627, doi:10.1175/2011JAS3733.1.

Oh, C., and C. M. Sorensen (1997), Light scattering study of fractal cluster aggregation near the free molecular regime, *J. Aerosol Sci.*, *28*(6), 937–957, doi:10.1016/S0021-8502(96)00488-0.

Oh, C., and C. M. Sorensen (1999), Scaling approach for the structure factor of a generalized system of scatterers, *J. Nanoparticle Res.*, *1*(3), 369–377, doi:10.1023/A:1010033111039.

Popovicheva, O., E. Kireeva, N. Persiantseva, M. Timofeev, H. Bladt, N. P. Ivleva, R. Niessner, and J. Moldanová (2012), Microscopic characterization of individual particles from multicomponent ship exhaust, *J. Environ. Monit.*, *14*(12), 3101–3110, doi:10.1039/C2EM30338H.

Porod, G. (1951), Die Röntgenkleinwinkelstreuung von dichtgepackten kolloiden Systemen, *Kolloid-Z.*, *124*(2), 83–114, doi:10.1007/BF01512792.

Purcell, E., and Pennypac.cr (1973), Scattering and Absorption of Light by Nonspherical Dielectric Grains, *Astrophys. J.*, *186*(2), 705–714, doi:10.1086/152538.

Roberts, G. C., and A. Nenes (2005), A Continuous-Flow Streamwise Thermal-Gradient CCN Chamber for Atmospheric Measurements, *Aerosol Sci. Technol.*, *39*(3), 206–221, doi:10.1080/027868290913988.

Sorensen, C., W. Hageman, T. Rush, H. Huang, and C. Oh (1998), Aerogelation in a Flame Soot Aerosol, *Phys. Rev. Lett.*, *80*(8), 1782–1785, doi:10.1103/PhysRevLett.80.1782.

Sorensen, C. M. (2001), Light Scattering by Fractal Aggregates: A Review, *Aerosol Sci. Technol.*, *35*(2), 648–687, doi:10.1080/02786820117868.

Sorensen, C. M. (2013a), Q-space analysis of scattering by dusts, *J. Quant. Spectrosc. Radiat. Transf.*, *115*, 93–95, doi:10.1016/j.jqsrt.2012.09.001.

Sorensen, C. M. (2013b), Q-space analysis of scattering by particles: A review, *J. Quant. Spectrosc. Radiat. Transf.*, *131*, 3–12, doi:10.1016/j.jqsrt.2012.12.029.

Sorensen, C. M., and D. J. Fischbach (2000), Patterns in Mie scattering, *Opt. Commun.*, *173*(1-6), 145–153, doi:10.1016/S0030-4018(99)00624-0.

Sorensen, C. M., and D. Shi (2000), Guinier analysis for homogeneous dielectric spheres of arbitrary size, *Opt. Commun.*, *178*(1-3), 31–36, doi:10.1016/S0030-4018(00)00601-5.

Sorensen, C. M., J. Cai, and N. Lu (1992a), Light-scattering measurements of monomer size, monomers per aggregate, and fractal dimension for soot aggregates in flames, *Appl. Opt.*, *31*(30), 6547, doi:10.1364/AO.31.006547.

Sorensen, C. M., J. Cai, and N. Lu (1992b), Test of static structure factors for describing light scattering from fractal soot aggregates, *Langmuir*, *8*(8), 2064–2069, doi:10.1021/la00044a029.

Sorensen, C. M., W. Kim, D. Fry, D. Shi, and A. Chakrabarti (2003), Observation of Soot Superaggregates with a Fractal Dimension of 2.6 in Laminar Acetylene/Air Diffusion Flames, *Langmuir*, *19*(18), 7560–7563, doi:10.1021/la034063h.

Sorensen, C. M., E. Zubko, W. R. Heinson, and A. Chakrabarti (2014), Q-space analysis of scattering by small irregular particles, *J. Quant. Spectrosc. Radiat. Transf.*, *133*, 99–105, doi:10.1016/j.jqsrt.2013.07.020.

Spencer, M. T., and K. A. Prather (2006), Using ATOFMS to Determine OC/EC Mass Fractions in Particles, *Aerosol Sci. Technol.*, *40*(8), 585–594, doi:10.1080/02786820600729138.

Stauffer, D., and A. Aharony (1994), *Introduction To Percolation Theory: Revised Second Edition*, 2 edition., Taylor & Francis, London.

Stipe, C. B., B. S. Higgins, D. Lucas, C. P. Koshland, and R. F. Sawyer (2005), Inverted co-flow diffusion flame for producing soot, *Rev. Sci. Instrum.*, *76*(2), 023908, doi:10.1063/1.1851492.

US EPA, O. of A. and R. (n.d.), Black Carbon Report to Congress, Available from: http://www3.epa.gov/blackcarbon/ (Accessed 3 November 2015)

Veihelmann, B., T. Nousiainen, M. Kahnert, and W. J. van der Zande (2006), Light scattering by small feldspar particles simulated using the Gaussian random sphere geometry, *J. Quant. Spectrosc. Radiat. Transf.*, *100*(1-3), 393–405, doi:10.1016/j.jqsrt.2005.11.053.

Volten, H., O. Munoz, E. Rol, J. F. de Haan, W. Vassen, J. W. Hovenier, K. Muinonen, and T. Nousiainen (2001), Scattering matrices of mineral aerosol particles at 441.6 nm and 632.8 nm, *J. Geophys. Res.-Atmospheres*, *106*(D15), 17375–17401, doi:10.1029/2001JD900068.

Volten, H., O. Muñoz, J. R. Brucato, J. W. Hovenier, L. Colangeli, L. B. F. M. Waters, and W. J. van der Zande (2006), Scattering matrices and reflectance spectra of forsterite particles with different size distributions, *J. Quant. Spectrosc. Radiat. Transf.*, *100*(1–3), 429–436, doi:10.1016/j.jqsrt.2005.11.074.

Volten, H., O. Muñoz, J. W. Hovenier, F. J. M. Rietmeijer, J. A. Nuth, L. B. F. M. Waters, and W. J. van der Zande (2007), Experimental light scattering by fluffy aggregates of magnesiosilica, ferrosilica, and alumina cosmic dust analogs, *Astron. Astrophys.*, *470*(1), 10, doi:10.1051/0004-6361:20066744.

Wang, X., G. Chancellor, J. Evenstad, J. E. Farnsworth, A. Hase, G. M. Olson, A. Sreenath, and J. K. Agarwal (2009), A Novel Optical Instrument for Estimating Size Segregated Aerosol Mass Concentration in Real Time, *Aerosol Sci. Technol.*, *43*(9), 939–950, doi:10.1080/02786820903045141.

Wang, Y., A. Chakrabarti, and C. M. Sorensen (2015), A light-scattering study of the scattering matrix elements of Arizona Road Dust, *J. Quant. Spectrosc. Radiat. Transf.*, *163*, 72–79, doi:10.1016/j.jqsrt.2015.05.002.

West, R. A. (1991), Optical properties of aggregate particles whose outer diameter is comparable to the wavelength, *Appl. Opt.*, *30*(36), 5316, doi:10.1364/AO.30.005316.

Yin, J. Y., and L. H. Liu (2010), Influence of complex component and particle polydispersity on radiative properties of soot aggregate in atmosphere, *J. Quant. Spectrosc. Radiat. Transf.*, *111*(14), 2115–2126, doi:10.1016/j.jqsrt.2010.05.016.

Zhang, H., C. Sorensen, E. Ramer, B. Olivier, and J. Merklin (1988), Insitu Optical Structure Factor Measurements of an Aggregating Soot Aerosol, *Langmuir*, *4*(4), 867–871, doi:10.1021/la00082a015.

Zubko, E., Y. Shkuratov, N. N. Kiselev, and G. Videen (2006), DDA simulations of light scattering by small irregular particles with various structure, *J. Quant. Spectrosc. Radiat. Transf.*, *101*(3), 416–434, doi:10.1016/j.jqsrt.2006.02.055.

Zubko, E., Y. Shkuratov, M. Mishchenko, and G. Videen (2008), Light scattering in a finite multi-particle system, *J. Quant. Spectrosc. Radiat. Transf.*, *109*(12-13), 2195–2206, doi:10.1016/j.jqsrt.2008.03.007.

Zubko, E., H. Kimura, Y. Shkuratov, K. Muinonen, T. Yamamoto, H. Okamoto, and G. Videen (2009), Effect of absorption on light scattering by agglomerated debris particles, *J. Quant. Spectrosc. Radiat. Transf.*, *110*(14-16), 1741–1749, doi:10.1016/j.jqsrt.2008.12.006.

Appendix A - Internal coupling parameter and corresponding Q-space exponent

Experiment	**ρ'**	**exp.**
Amsterdam-Granada Group's Aerosol		
Rutile (632.8)	1.76	2.13
Hematite (632.8)	5.78	1.61
Allende (632.8)	5.80	2.11
Feldspar (632.8)	6.33	2.47
Allende (441.6)	8.30	1.96
Feldspar (441.6)	9.07	2.09
Olivine S (632.8)	9.07	1.99
Forsterite small (632.8)	9.19	2.31
Red clay (632.8)	10.2	2.16
Green clay (632.8)	10.5	2.29
Forsterie initial (632.8)	12.7	2.24
Olivine S (441.6)	13.0	1.75
Quartz (632.8)	14.3	2.18
Red clay (441.6)	14.6	2.04
Green clay (441.6)	15.1	2.12
Ashton (632.8)	16.6	1.74
Olivine M (632.8)	18.1	2.06
Pinatubo (632.8)	19.0	2.01
El Chichon (632.8)	20.2	1.87
Quartz (441.6)	20.5	1.79

Gunsight (632.8)	21.1	1.75
Forsterite washed (632.8)	23.3	2.10
Mount St. Helens (632.8)	24.8	1.79
Redoubt A (632.8)	24.8	1.76
Flay ash (632.8)	24.8	1.99
Olivine M (441.6)	26.0	1.81
Martian analog(palagonite) (632.8)	26.3	1.82
Loess (632.8)	26.5	2.12
Olivine L (632.8)	26.5	1.86
Pinatubo (441.6)	27.2	1.87
Anchorage (632.8)	29.0	1.76
Flay ash (441.6)	35.5	2.03
Loess (441.6)	38.0	1.81
Olivine L (441.6)	38.0	1.63
Redoubt B (632.8)	38.6	1.72
Olivine XL (632.8)	44.0	1.87
Lokon (632.8)	44.9	1.60
Sahara (632.8)	55.7	1.92
Olivine XL (441.6)	63.0	1.72
Lokon (441.6)	64.4	1.49
Sahara (441.6)	79.8	1.56
Stop 33 (632.8)	86.9	1.77
Sahara sand (Libya) (632.8)	729	1.70
AZRD		
Ultrafine (Iowa)	4.59	2.60

Ultrafine (KSU)	25.8	2.23
Fine (KSU)	52.6	2.17
Medium (KSU)	92.8	2.12
Al_2O_3 Abrasives		
1200 grit	29.2	2.10
1000 grit	43.4	1.75
800 grit	63.2	1.50
600 grit	90.4	1.62
400 grit	168	1.55
320 grit	284	1.56
Theory	**ρ'**	**exp.**
GRS		
	0.133	4.00
	0.160	4.00
	0.186	4.00
	0.213	4.00
	0.240	4.00
	0.266	4.00
	0.399	4.00
	1.31	3.90
	1.57	3.80
	1.83	3.70
	2.09	3.60
	2.36	3.60
	2.56	3.40

	2.62	3.50
	3.07	3.30
	3.58	3.20
	3.74	3.00
	3.93	3.40
	4.09	3.00
	4.49	2.80
	4.60	2.80
	4.85	2.30
	5.12	2.80
	5.24	2.40
	5.82	2.20
	5.88	2.10
	5.98	2.40
	6.73	2.40
	6.79	2.00
	7.06	2.00
	7.76	2.00
	8.24	2.00
	8.73	2.00
	9.41	2.00
	10.6	1.80
	11.2	2.00
	17.6	1.60
Thickened Percolation Clusters		

	1.15	4.00
	3.05	3.00
	4.32	3.00
	6.91	3.00
	7.07	3.00
	8.55	3.00
	10.2	2.00
	11.6	1.50
	11.8	1.50
Irregular spheres		
	2.33	3.60
	2.33	3.30
	2.33	3.40
	2.33	3.50
	3.11	3.60
	3.11	3.30
	3.11	3.30
	3.11	3.50
	3.55	3.50
	3.55	3.00
	3.55	3.00
	3.55	3.00
	3.89	3.60
	3.89	3.30
	3.89	3.00

	3.89	3.00
	4.11	2.90
	4.11	2.50
	4.11	2.30
	4.11	2.20
	4.67	3.50
	4.67	3.30
	4.67	3.00
	4.67	3.00
	4.74	3.00
	4.74	2.80
	4.74	3.00
	4.74	2.90
	5.44	3.50
	5.44	2.90
	5.44	3.00
	5.44	3.00
	5.47	2.20
	5.47	2.10
	5.47	2.00
	5.47	1.80
	5.92	3.00
	5.92	2.80
	5.92	2.50
	5.92	2.80

	6.84	1.90
	6.84	1.90
	6.84	2.00
	6.84	1.50
	7.11	2.90
	7.11	2.80
	7.11	2.20
	7.11	2.80
	8.21	1.60
	8.21	1.60
	8.21	2.00
	8.21	1.40
	8.29	2.90
	8.29	2.80
	8.29	2.20
	8.29	2.80
	9.58	1.60
	9.58	1.60
	9.58	1.90
	9.58	1.40

Table A.1 Internal coupling parameter and corresponding Q-space exponent for each particle presented in Chapter 5.